

Washington University in St. Louis

Washington University Open Scholarship

McKelvey School of Engineering Theses & Dissertations

McKelvey School of Engineering

Summer 8-15-2013

Improving Radiotherapy Targeting for Cancer Treatment Through Space and Time

Camille Noel

Washington University in St. Louis

Follow this and additional works at: https://openscholarship.wustl.edu/eng_etds



Part of the [Engineering Commons](#)

Recommended Citation

Noel, Camille, "Improving Radiotherapy Targeting for Cancer Treatment Through Space and Time" (2013). *McKelvey School of Engineering Theses & Dissertations*. 219.
https://openscholarship.wustl.edu/eng_etds/219

This Dissertation is brought to you for free and open access by the McKelvey School of Engineering at Washington University Open Scholarship. It has been accepted for inclusion in McKelvey School of Engineering Theses & Dissertations by an authorized administrator of Washington University Open Scholarship. For more information, please contact digital@wumail.wustl.edu.

WASHINGTON UNIVERSITY IN ST. LOUIS

School of Engineering and Applied Science

Department of Biomedical Engineering

Thesis Examination Committee:

Parag Parikh (Chair)

Mark Anastasio

Shelton Caruthers

Dennis Hallahan

Sasa Mutic

Pamela Woodard

Improving Radiotherapy Targeting for Cancer Treatment Through Space and Time

by

Camille E. Noel

A dissertation presented to the Graduate School of Arts and Sciences
of Washington University in partial fulfillment of the
requirements for the degree of
Doctor of Philosophy

August 2013

Saint Louis, Missouri

© 2013, Camille E. Noel

Contents

List of Figures	iv
List of Tables	v
List of Abbreviations & Acronyms	vi
Acknowledgments	viii
Dedication	x
Abstract	xi
1 Introduction	1
1.1 Positional Uncertainties in Radiotherapy	1
1.2 Radiotherapy Treatment Evaluation using Point-based Tracking	4
1.3 MRI for Localization of Targeted Anatomy and Critical Structures	5
1.3.1 Segmentation Precision of Abdominal Anatomy for MRI-based Radiotherapy	6
1.3.2 Low-field Onboard MRI for Anatomy Visualization in Radiotherapy	7
1.4 Onboard Cine MRI for Tracking Bowel	7
1.5 Process-Based Quality Management for Clinical Implementation of Adaptive Radiotherapy	8
2 Radiotherapy Treatment Evaluation using Point-Based Tracking	10
2.1 Background and Significance	11
2.2 Materials & Methods	13
2.2.1 Real-time Tracking System	13
2.2.2 Tracking Data	14
2.2.3 Treatment Planning System Data	15
2.2.4 The SWIFTER Application	15
2.2.5 Phantom Study	21
2.2.6 Patient Case Study	23
2.3 Results	24
2.3.1 Phantom Study	24
2.3.2 Patient Case Study	25
2.4 Discussion	28
3 MRI for Localization of Targeted Anatomy and Critical Structures	31
3.1 Segmentation Precision of Abdominal Anatomy for MRI-based Radiotherapy	32
3.1.1 Background & Significance	32
3.1.2 Materials & Methods	33
3.1.3 Results	40
3.1.4 Discussion	43

3.2	Low-field MRI for Anatomy Visualization in Radiotherapy	45
3.2.1	Background & Significance	45
3.2.2	Materials & Methods	47
3.2.3	Results	49
3.2.4	Discussion	54
4	Onboard Cine MRI for Tracking Bowel	58
4.1	Background & Significance	58
4.2	Materials & Methods	62
4.2.1	Imaging Equipment	62
4.2.2	Image Acquisition & Data	62
4.2.3	Tracking Software	62
4.3	Results	73
4.4	Discussion	78
5	Process-Based Quality management for Clinical Implementation of Adaptive Radiotherapy	82
5.1	Background & Significance	82
5.2	Materials & Methods	84
5.2.1	Failure Mode & Effects Analysis (FMEA)	84
5.2.2	FMEA for Adaptive Radiotherapy	84
5.3	Results	88
5.3.1	Overall Trends	88
5.3.2	Process-specific trends	89
5.3.3	Critical Failures	90
5.3.4	Quality Control Strategies	91
5.4	Discussion	97
Appendix	Extended Definitions & Descriptions	99
A.1	Calypso Electromagnetic Tracking System	99
A.2	Gamma Dosimetric Analysis	101
A.3	ViewRay Onboard MRI	101
A.4	Active Contour Model	104
A.5	IMRT QA	107
A.6	Failure Mode & Effects Analysis	107
References	109	
Curriculum Vitae	116	

List of Figures

Figure 1.1: Resolution of localization technologies	4
Figure 2.1: Flowchart of input data, application processes, and output data for SWIFTER	16
Figure 2.2: Example of the consequences of rotational and translational target motion	17
Figure 2.3: Frequency histogram of inter- and intra-fraction prostate motion	18
Figure 2.4: Workflow for SWIFTER's retrospective dose analysis	19
Figure 2.5: Visualization tool of the SWIFTER application	21
Figure 2.6: SWIFTER phantom validation	23
Figure 2.7: Example three-dimensional dose distribution computed by SWIFTER	27
Figure 2.8: Dose statistics for a case study of a 3mm- and 5-mm margin prostate plan	27
Figure 3.1: Schematic of OAR segmentation on MR images	35
Figure 3.2: Derivation of an example baseline contour	37
Figure 3.3: Mean contouring precision metrics for abdominal organs	40
Figure 3.4: Images of BFFE and T2W MRI sequences	41
Figure 3.5: Mean ICC values for precision metrics	43
Figure 3.6: Example of OB-MRI/OB-CT image set pairs	50
Figure 3.7: Ratings of structure visualization on onboard MRI, stratified by site	51
Figure 3.8: Ratings of structure visualization on onboard MRI, stratified by structure type.....	53
Figure 4.1: Basic workflow of bowel tracking software	63
Figure 4.2: Workflow of determining the contour shift on frame n	65
Figure 4.3: Example of E_{region} in aiding contour expansion	68
Figure 4.4: Example of E_{region} in aiding contour contraction	68
Figure 4.5: Example of changing bowel contrast	69
Figure 4.6: Workflow of determining the output contour for frame $n+1$	71
Figure 4.7: Example of tracking inaccuracies	72
Figure 4.8: Example of tracked bowel abutting a tumor	73
Figure 4.9: Example of tracked bowel segments	74
Figure 4.10: Histogram of accurately tracked cine image frames	76
Figure 4.11: Example of deforming bowel	77
Figure 5.1: Flow diagram of major intensity-modulated ART processes and subprocesses	86
Figure 5.2: Change in RPN, O, S, and D values for intensity-modulated ART	89
Figure 5.3: Common & unique critical failures for intensity-modulated ART & standard IMRT.....	91
Figure 5.4: Identified points of Quality Control (QC) strategies for ART	94
Figure A.1: Calypso Electromagnetic Tracking System	99
Figure A.2: Onboard MRI Imaging System	102

List of Tables

Table 2.1:	Limitations of image-guided techniques for ART	12
Table 2.2:	Percent dose difference between SWIFTER and the TPS	25
Table 2.3:	SWIFTER processing time	26
Table 2.4:	Dose statistics for a case study of a 3mm- and 5-mm margin prostate plan	28
Table 3.1:	Subject sample characteristics for imaging on a 1.5T MRI	34
Table 3.2:	Odds ratios for contouring precision, by imaging sequence	42
Table 3.3:	List of evaluated OARS, by anatomical site	52
Table 3.4:	Ratings for targets evaluated on onboard MRI	54
Table 4.1:	Features of tracked bowel segments	74
Table 4.2:	Motion statistics for tracked bowel	75
Table 4.3:	Number of cases resulting in tracking inaccuracies	76
Table 5.1:	FMEA table of O, S, and D values	85
Table 5.2:	Overall statistics for ART FMEA values	88
Table 5.3:	Mitigation & QC strategies for ART processes with critical failures	93

List of Abbreviations & Acronyms

AAPM	–	American Association of Physicists in Medicine
A-P	–	Anterior-Posterior
ART	–	Adaptive Radiation Treatment/Radiotherapy
BFFE	–	Balanced Fast-Field Echo
CBCT	–	Conebeam Computed Tomography
CERR	–	Computational Environment for Radiotherapy Research
CMS	–	Center for Medicare & Medicaid Services
CT	–	Computed Tomography
CTV	–	Clinical Target Volume
D	–	Detectability
D_{95}	–	Percent dose covering 95% of the target volume
D_{max}	–	Maximum Dose
D_{mean}	–	Mean Dose
D_{min}	–	Minimum Dose
DC	–	Dice Coefficient
DTA	–	Distance to Agreement
EBRT	–	External Beam Radiation Treatment/Radiotherapy
FID	–	Free Induction Decay
FMEA	–	Failure Mode & Effects Analysis
HD	–	Hausdorff Distance
ICC	–	Intraclass Coefficient
IGRT	–	Image-Guided Radiation Treatment/Radiotherapy
IMRT	–	Intensity Modulated Radiation Treatment/Radiotherapy
LINAC	–	Linear Accelerator
MR	–	Magnetic Resonance
MRI	–	Magnetic Resonance Imaging
MVCT	–	Megavoltage Computed Tomography
mT	–	millitesla
NCC	–	Normalized Cross Correlation
O	–	Occurrence
OAR	–	Organ At Risk
OB-CT	–	Onboard Computed Tomography
OB-MRI	–	Onboard Magnetic Resonance Imag(ing/er)
pdf	–	probability density function
PTV	–	Planned Target Volume
QA	–	Quality Assurance
RF	–	Radio-Frequency
RPN	–	Risk Priority Number
RT	–	Radiotherapy
S	–	Severity
SNR	–	Signal-to-Noise Ratio
S-I	–	Superior-Inferior

STAPLE	–	Simultaneous Truth And Performance Level Estimation
SWIFTER	–	Semi-automatic Workflow using Intrafraction Fiducial-based Tracking for Evaluation of Radiotherapy
T	–	Tesla
T2W	–	T2-Weighted
TE	–	Echo Time
TG-100	–	Task Group 100
TPS	–	Treatment Planning System
TR	–	Repetition Time
TrueFISP	–	True Fast Imaging with Steady-State Precession
TurboFLASH	–	Turbo Fast Low Angle Shot
WNCC	–	Weighted Normalized Cross Correlation

Acknowledgments

This dissertation is a culmination of support and guidance from my mentors, colleagues, friends, and family, to which I owe my gratitude.

I would first like to acknowledge my principal investigator, Dr. Parag Parikh, for his guidance and persistent endeavor of impactful research. He is truly a leader in the field of innovative cancer technology. I have learned a tremendous amount from his tenacity and expertise, and I am fortunate to have him as a mentor. I would also like to extend my gratitude to my committee members, each of whom is a champion for excellent research. I am grateful for their invaluable support and counsel, and for their commitment to seeing this research to success. I would like to acknowledge my funding source, the Washington University Institute of Clinical and Translational Sciences (ICTS) grant UL1 TR000448, sub-award TL1 TR000449, from the National Center for Advancing Translational Sciences. I applaud the ICTS for recognizing the value of translational research, and the profound impact it has on patients and investigators alike.

My friends and colleagues in the Radiation Oncology Technology Lab at Washington University deserve a special thanks for their continual support. In particular, I would like to thank Drs. Ryan Smith, Jiajia Ge and Shyam Bharat for their contributions to this work. Likewise, I would like to thank the clinical and research groups at the Department of Radiation Oncology. To the physicians who I've had the great pleasure of working with, I thank you for your collaboration and trust. To the therapists, technicians, nurses, dosimetrists and other clinicians who have contributed to this research, I thank you for your sincere commitment to improving patient care.

The Medical Physics group, with whom I have a long-standing and fond relationship, is owed a heartfelt thanks for the invaluable support they have provided during my time with the Department. In particular, I would like to thank my dear friend and colleague, Dr. Lakshmi Santanam for her commitment to the success of this work. She has not only been my advocate, but a truly dedicated advocate for the advancement of cancer treatment. Her tireless efforts in the name of patient care have helped shape my passion for this work. For that, I cannot thank her enough.

I would like to extend my deepest gratitude to the patients who donated their valuable time and energy to participate in this research, and to those who never had the chance to. They are the heart and soul of this work. They are the heart and soul of *every* research effort made in the name of cancer. I am gratified and humbled every day to have to opportunity to pursue such a weighty endeavor.

Finally, I would like to thank my friends and family for their continual love and support. I owe them my gratitude. To my loving parents, who instilled in me a profound sense of drive, community, and world perspective — they have truly built the foundation upon which this work stands. To my grandmother and sisters, who take such great pride in my achievements; to Jayce, who centers me when I drift into quantum worlds; to all my family, who honor my work as if it were their own...

...thank you.

Without the support of all those above, this work would not have been possible.

Camille E. Noel

Washington University in St. Louis

August 2013

Dedicated to all those afflicted by cancer,
and all those in search of “the cure.”

ABSTRACT OF THE DISSERTATION

Improving Radiotherapy Targeting for Cancer Treatment Through Space and Time

by

Camille E. Noel

Doctor of Philosophy in Biomedical Engineering

Washington University in St. Louis, 2013

Research Advisor: Parag Parikh

Radiotherapy is a common medical treatment in which lethal doses of ionizing radiation are preferentially delivered to cancerous tumors. In external beam radiotherapy, radiation is delivered by a remote source which sits several feet from the patient's surface. Although great effort is taken in properly aligning the target to the path of the radiation beam, positional uncertainties and other errors can compromise targeting accuracy. Such errors can lead to a failure in treating the target, and inflict significant toxicity to healthy tissues which are inadvertently exposed high radiation doses.

Tracking the movement of targeted anatomy between and during treatment fractions provides valuable localization information that allows for the reduction of these positional uncertainties. Inter- and intra-fraction anatomical localization data not only allows for more accurate treatment setup, but also potentially allows for 1) retrospective treatment evaluation, 2) margin reduction and modification of the dose distribution to accommodate daily anatomical changes (called 'adaptive radiotherapy'), and 3) targeting interventions during treatment (for example, suspending radiation delivery while the target is outside the path of the beam).

The research presented here investigates the use of inter- and intra-fraction localization technologies to improve radiotherapy to targets through enhanced spatial and temporal accuracy. These technologies provide significant advancements in cancer treatment compared to standard clinical technologies. Furthermore, work is presented for the use of localization data acquired from these technologies in adaptive treatment planning, an investigational technique in which the distribution of planned dose is modified during the course of treatment based on biological and/or geometrical changes of the patient's anatomy. The focus of this research is directed at abdominal sites, which has historically been central to the problem of motion management in radiation therapy.

Chapter 1

Introduction

1.1 Positional Uncertainties in Radiotherapy

Radiotherapy is a common medical treatment in which lethal doses of ionizing radiation are preferentially delivered to cancerous tumors. Through the delivery of high-energy radiation to cancerous tissue, the DNA of malignant cells are damaged and the mass is shrunk or killed altogether. Radiotherapy is used in several capacities, including as a primary or adjuvant curative treatment, a means for preventing spread of local disease, and an agent of palliative treatment [1]. Approximately 65% of cancer patients are treated with some form of radiotherapy, and of those patients, the majority receive external beam radiotherapy (EBRT) [2]. In EBRT, radiation is delivered by an external radiation source which sits several feet from the patient's surface. In most EBRT schemes, the radiation dose is delivered over the course of days, weeks or months. This type of treatment scheme allows for healthy cells in the path of the delivered radiation beam to recover from radiation damage between delivered treatments (called 'fractions'), while less resilient malignant cells recover more slowly.

The fundamental sequence of steps in the radiotherapy process is as follows: 1) patient simulation, during which volumetric medical images of the targeted anatomy are obtained for the treatment planning process, 2) treatment planning, during which radiation dose to the target is virtually planned using the simulation image set(s), and 3) treatment delivery, during which the planned radiation dose is delivered using radiation-emitting equipment.

Radiotherapy is often a complex process, and errors in accurate treatment targeting can originate from any of these fundamental steps. A major challenge in the planning and delivery of EBRT is accurately positioning the target in the path of the radiation beam. Many targets change position or shape between or during treatment fractions, introducing targeting uncertainties and exposing healthy tissue to radiation. Thus, inter-/intra-fraction target motion introduces two critical hazards: shifting the target out from the path of radiation so that malignant cells do not receive the intended dose, and shifting healthy tissues into the path of radiation, increasing the risk for normal tissue toxicities and the associated adverse side effects.

Highly conformal techniques, namely intensity modulated radiotherapy (IMRT), are now commonplace in order to more accurately shape the radiation dose to the target region. However, uncertainties in localization of dynamic targets both between and during treatment fractions have historically called for an expansion of the targeted volume planned for irradiation. The inclusion of an additional volume of tissue surrounding the target (referred to as a ‘margin’) helps to ensure that the target is still irradiated, even if it is slightly misaligned during treatment delivery. Thus, the volume of tissue planned to receive the prescription dose of radiation (called the ‘planned target volume’ (PTV)) is actually larger than the target volume itself (called the ‘clinical target volume’). The inclusion of excessive spatial margins in the PTV means that the additional tissue around the target is also irradiated. While these excessive margins are designed to compensate for positional uncertainties, the associated normal tissue exposure limits dose escalation techniques, which have been shown to improve disease-free survival and local control [3].

In order to mitigate positional uncertainties, X-ray based imaging equipment attached to the treatment machine is routinely used to align the patient to the path of the radiation beam (called the treatment ‘isocenter’) immediately before dose delivery [4]. These technologies range from 2D flat-panel imagers to 3D volumetric fan-beam or cone-beam computed tomography. Both two- and three-dimensional imaging technologies have been implemented at kilo-voltage (kV) and mega-voltage (MV) energy levels. These technologies are used to track the movement of targeted anatomy between and during treatment fractions, a method known as image-guided radiotherapy (IGRT). IGRT provides valuable localization information that allows for the reduction of these positional uncertainties and more accurate patient alignment. Inter- and intra-fraction anatomical localization data not only allows for more accurate treatment setup, but also potentially allows for 1) retrospective treatment evaluation, 2) margin reduction and modification of the dose distribution to accommodate daily anatomical changes (called ‘adaptive radiotherapy’), and 3) targeting interventions during treatment (for example, suspending radiation delivery while the target is outside the path of the beam).

While onboard X-ray based imaging technology has improved patient positioning accuracy dramatically over the past several decades [5], it still suffers from many shortcomings. Dosimetric patient safety concerns limit its use for daily localization and continuous target localization during treatment [4]. It is also poorly suited for visualizing soft-tissue anatomy [6], which compromises localization accuracy of many targets and healthy tissues. New devices and techniques have been under development to improve upon the spatial and temporal accuracy provided by standard X-Ray based technologies (Figure 1.1). The research presented here investigates the use of novel inter- and intra-fraction localization technologies to improve radiotherapy to moving targets. This research is divided into four parts, each of which is briefly described herein.

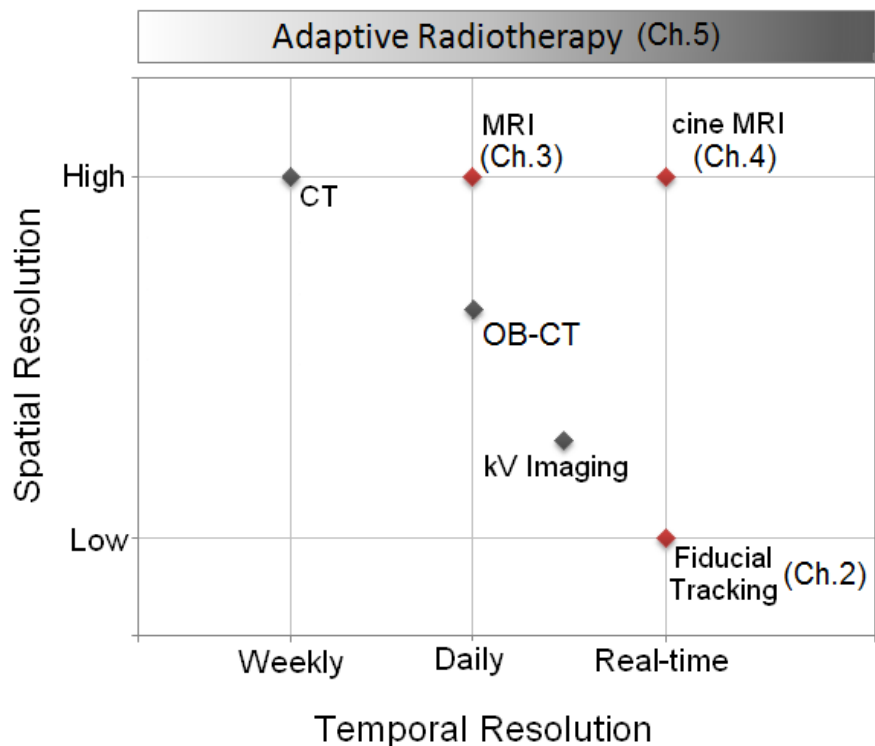


Figure 1.1 Temporal and spatial resolution of current technologies (gray) and technologies investigated in the presented research (red). Chapter 2 (Ch.2): Fiducial and point-based tracking, Chapter 3 (Ch.3): Magnetic resonance imaging (MRI), Chapter 4 (Ch.4): cine MRI, and Chapter 5 (Ch.5): Adaptive radiotherapy, which is applied in varying degrees according to the temporal resolution. OB-CT = Onboard Computed Tomography, kV = kilovoltage

1.2 Radiotherapy Treatment Evaluation using Point-based Tracking

The practice of localizing targets using implanted markers or anatomical landmarks has been available for decades. Lacking the ability to visualize soft tissue targets and structures, practitioners use the position of radiopaque markers (or dense anatomical landmarks) as visualized on onboard X-Ray imaging equipment as a surrogate for the position of the structure of interest. More recently, electromagnetic tracking technology made it possible to track wireless transponders implanted in the target, without the use of imaging equipment (see Appendix). Point-based localization and tracking is widely used today for pre-treatment, intra-treatment, and post-treatment positioning verification

of targets under treatment. However, the tracking information acquired from point-based localization technologies also offers potential value for evaluation of dosimetric coverage and adequacy of treatment for dynamic targets. Utilizing point-based tracking data, we developed a highly automated method for daily computation of cumulative dosimetric effects of inter- and/or intra-fraction target motion for cancer patients. This work describes a software application and workflow which enables (1) pre-treatment determination of appropriate rotational/translational motion limits for dynamic targets under treatment (2) post-treatment analysis of dosimetric target coverage after daily treatment, and (3) visualization of three-dimensional rotations and translations of the target with respect to the three-dimensional planned target volume and dose distribution. When used as a dose delivery evaluation tool, this application can provide increased confidence for radiation treatment. The validation and utility of this application is demonstrated with phantom testing and a prostate cancer patient case localized with continuous electromagnetic fiducial-based tracking.

There are some disadvantages of utilizing point-based data for localization and dosimetric evaluation in comparison to utilizing image data (as discussed in Chapter 2), which is the subject of the next part of this work. Emerging imaging methods may enable better targeting than current localization techniques. One such method is the use of magnetic resonance imaging (MRI) to localize mobile, deformable soft-tissue targets both before treatment and during treatment. The use of this technology is investigated in Chapter 3 of this work, and is introduced in the following section.

1.3 MRI for Localization of Targeted Anatomy and Critical Structures

Tissue targeting originates in the pre-treatment dose planning stage, in which computed tomography CT images are used to characterize the shape and location of the tumor and surrounding anatomy. Accurate treatment relies on the accurate delineation of these anatomical structures during planning, and requires that these structures are positioned in a reproducible fashion on the treatment machine every day. Since targets and organs at risk are often composed of soft-tissue, accurate pre-treatment delineation and daily alignment of these structures can be compromised using the standard X-Ray

based imaging equipment available in clinical practice [7, 8]. It is well-established that MRI provides better representation of patient anatomy for visualization and planning in many sites, including the head, central nervous system and pelvis [7, 9-11]. Supplementing computed tomography (CT) planning images with MR images for planning has been shown to result in more precise delineation in these sites, enabling better targeting and normal tissues sparing [9-12]. Such findings have motivated the development of MRI-only planning [7] and onboard MRI devices for treatment localization or adaptive treatment [13-15], rendering MRI-based radiotherapy a current focus of clinical interest.

1.3.1 Segmentation Precision of Abdominal Anatomy for MRI-based Radiotherapy

Despite large research efforts for many sites, there have been few investigations on the use of MRI for radiotherapy planning of abdominal cancer, a disease for which improved soft tissue targeting could offer considerable benefit. The respiratory motion experienced by abdominal organs during imaging has historically made abdominal MRI challenging, and the development and use of abdominal motion-compensation MRI techniques is still relatively new. Thus it is perhaps not surprising that MRI-based radiotherapy for abdominal sites has remained largely unstudied. The first part of the work presented in Chapter 3 entails an evaluation of the use of MR images for segmentation of abdominal anatomy. The inter- and intra-observer precision of normal tissue delineation is characterized on images acquired with two different sequences on a 1.5T MRI scanner. By assessing the contouring precision of abdominal anatomy offered by MRI, we aim to gain insight into its potential utility for planning and localization of abdominal cancer patients.

1.3.2 Low-field Onboard MRI for Anatomy Visualization in Radiotherapy

In the second part of Chapter 3, a new technology known as onboard MRI is investigated for its use in improving daily localization of soft-tissue structure for radiotherapy. On-board MRI is an emerging technology that is being investigated by many groups in aim of mitigating daily positioning inaccuracies and providing better anatomical information for soft-tissue localization and adaptive planning [13-15]. The anatomical information acquired by this technology could 1) allow for improved target localization 2) enable clinicians to evaluate daily dosimetric variations caused by positional differences in the anatomy and 3) improve treatment by enabling adaptation of the dose to the daily anatomy. However low-field MRI is characterized by a relatively low signal-to-noise ratio, and the implications of this technology for clinical target and normal structure visualization is unknown.

The purpose of this work is to assess the use of a novel onboard low-field MRI technology for target and tissue visualization in patients undergoing radiotherapy, in comparison to standard onboard X-Ray based imaging. The research presented here is integral to the assessment of this technology's clinical utility.

1.4 Onboard Cine MRI for Tracking Bowel

Intra-fraction tumor motion can introduce significant targeting uncertainties for radiotherapy treatment. Targets which move out of the path of the beam during dose delivery will be undertreated, while healthy tissues that move into the path of the beam are exposed to toxic levels of radiation. Furthermore, accurate treatment targeting can be particularly challenging for targets that are not only dynamic, but are also deformable. Currently, intra-fraction motion can only be accounted for by using surrogates, which may not accurately represent target motion, or X-Ray based imaging, which uses ionizing radiation and offers limited visibility of soft tissues. The promise of onboard, pre-treatment MRI for more accurate daily localization prior to treatment is an exciting

new development which is discussed in Chapter 3; however, the use of real-time onboard MRI during radiotherapy may provide even greater advantages for targeting mobile, deformable tissues.

In regard to this future application, we have presented similar work in the application of fiducial-based tracking data for dosimetric evaluation of prostate radiotherapy (as detailed in Chapter 2) [16, 17]. However, in contrast to cine MR, the nature of fiducial-based tracking data used in this previous work highlights an important limitation. This technique does not directly report on motion of critical structures, unless fiducials are implanted into the organ at risk. Fiducial-based tracking also does not offer volumetric information, and is generally not sensitive to organ deformation. In contrast, cine MRI acquired during radiotherapy does offer this information, enabling dosimetric analysis of the bowel and other organs that was previously impossible via clinically available technologies.

Abdominal tissues are more mobile than any other treatment site [18], and are highly deformable, making them difficult to target during dose delivery. In particular, bowel is one of the most critical dose-limiting structures in the abdomen due to its low radiation tolerance and poor localization during treatment [19]. A potentially significant use of intra-fraction positional information acquired from real-time onboard MR is suspending delivery of the treatment beam while the bowel is in its path, a technique known as beam ‘gating.’ To investigate the potential application of real-time MR-based ‘bowel-gated’ treatment, we have developed automated bowel-tracking software and evaluated its use on cine MR patient imagesets acquired with a hybrid MR-radiotherapy unit. Such a clinical application could enable safer dose escalation to abdominal targets and aide in clinical decisions or interventions designed to minimize or manage toxicity-induced side effects.

1.5 Process-Based Quality Management for Clinical Implementation of Adaptive Radiotherapy

As discussed in Chapters 2-4, enhanced localization techniques can improve radiotherapy treatment enabling better pre-treatment alignment, mid-treatment interventions, and post-treatment evaluation. However, an additional value of such enhanced localization technologies is their use in administering Adaptive Radian Therapy (ART). ART entails mid-treatment dose modification based

on anatomical or biological changes occurring throughout the treatment scheme. In this manner, the dose distribution can be optimized to target alignment tissues while sparing healthy tissues, based on the daily anatomy. Investigational studies demonstrating significant improvement in treatment efficacy using adaptive techniques [5, 20] have motivated clinical implementation.

Offline ART techniques involve removing the patient from the treatment couch for imaging before plan adaptation and dose delivery. Most commonly, the patient is sent home before receiving the adapted treatment plan days later. Online ART is logistically much more difficult, and involves imaging and re-planning the patient's treatment while the patient is still on the treatment couch. The adapted plan is then delivered immediately after adaptation. While ART is a popular focus of investigational study, it is rarely practiced in the clinic. Issues surrounding workflow, resource allocation, technology limitations and safety have limited the use of ART, and in particular, online ART. In light of these unique challenges, no one has described a framework for its clinical implementation. The lack of a robust quality management strategy for ART continues to deter its practice, while the lack of ART practice limits the implementation of a data-driven quality management scheme. We aimed to address this void by employing a process-based approach to identify high-priority errors and appropriate risk-mitigation strategies for ART. Chapter 5 of this work describes the application of Failure Mode and Effects Analysis (FMEA) in order to develop a quality management framework for the clinical implementation of ART.

Chapter 2

Radiotherapy Treatment Evaluation using Point-based Tracking

Point-based localization using implanted markers or anatomical landmarks is often used before, during or after radiation treatment for positioning verification of targets under treatment. However, the tracking information acquired from point-based localization technologies offers potential value for evaluation of dosimetric coverage and adequacy of treatment for dynamic targets. We developed a highly automated method for daily computation of cumulative dosimetric effects of inter- and/or intra-fraction target motion for cancer patients using point-based tracking. Software utilizing point-based tracking data was written to (1) prospectively determine appropriate rotational/translational motion limits for dynamic targets under treatment (2) retrospectively analyze dosimetric target coverage after daily treatment, and (3) visualize three-dimensional rotations and translations of the target with respect to the three-dimensional planned target volume and dose distribution. We present phantom testing and a prostate cancer patient case localized with continuous electromagnetic fiducial-based tracking to validate and demonstrate the utility of this application.

2.1 Background & Significance

Uncertainties in daily tumor localization have historically called for inclusion of excessive margins in the planning target volume (PTV). Several population-based methods have been proposed for determining treatment planning margins [21, 22]. Such methodologies incorporate common uncertainties introduced during radiation therapy, including inter- and intra-fraction organ motion, to define margins that provide acceptable coverage for 90% of patients. Still, standard use of margins determined from population-based criteria may lead to inadequate treatment for some patients and overtreatment for others.

Furthermore, the use of population-based margins prevents margin reduction, an essential component for dose escalation techniques. Prostate cancer, in particular, has been the focus of several clinical trials investigating dose escalation treatment schemes, as studies have shown improved local control [23-25]. Many studies reporting on the potential benefits gained from reduced PTV margins suggest that the degree of beneficence from margin reduction is patient-specific and may be dependent upon the shape of the target and its proximity to nearby organs at risk [26-28]. Adaptive radiation therapy using patient-specific margins and varying action levels based on inter-fraction set-up error has been published in detail [29-31]. More recently, an effort has been made to use volumetric imaging (cone-beam computed tomography (CBCT) or megavoltage computed tomography (MVCT)) for adaptive dose calculation [32-34]. While reports of potential benefits utilizing an image-guided based method are promising, clinical implementation has been limited for several reasons (Table 2.1).

Table 2.1 Limitations of image-guided techniques for ART.

Limitations	References
1) Regular QA and accuracy of HU units for dose computation	Oelfke <i>et al</i> [35], Baumann <i>et al</i> [36], Verellen [37] and McParland [6]
2) Mechanical limitations: Limited FOV, isocentric/geometric uncertainties due to gantry sag	Oelfke <i>et al</i> [35] and Verellen [37]
3) Image Quality: Increased noise and artifacts due to scatter, constraints on reconstruction algorithms, blurring from organ motion	Oelfke <i>et al</i> [35], Verellen [37], Chen <i>et al</i> [38], McParland [6] and Tran [39]
4) Only accounts for inter-fraction anatomical variability	Verellen [37], Chen <i>et al</i> [38]
5) Equipment/Technical costs	Baumann <i>et al</i> [36], McParland [6] and Tran [39]
6) Staffing and user training (acquisition, registration, target delineation)	Baumann <i>et al</i> [36], Chen <i>et al</i> [38], McParland [6] and Tran [39]
7) Accuracy/Reproducibility of automatic and manual soft-tissue delineation	Chen <i>et al</i> [38], McParland [6] and Tran [39]
8) Accuracy of image registration techniques (manual and automatic)	Verellen [37], Chen <i>et al</i> [38] and Tran [39]
9) Additional patient dose	Moseley <i>et al</i> [40], Murphy <i>et al</i> [4], Verellen [37], McParland [6] and Tran [39]
10) Data storage/transfer	Swerdloff [41], Baumann <i>et al</i> [36], Chen <i>et al</i> [38] and McParland [6]
11) Acquisition/Reconstruction/Registration time	Oelfke <i>et al</i> [35], Baumann <i>et al</i> [36], Verellen [37], Chen <i>et al</i> [38], McParland [6] and Tran [39]

Point-based tracking offers a new approach to the adaptive therapy process that bypasses many of the challenges involved in adaptive radiation therapy using volumetric imaging, including speed, data storage, additional radiation dose to the patient, and the requirement for target segmentation. Thus, our goal was to develop an infrastructure to evaluate dosimetric coverage of cancer patients utilizing point-based localization data. We developed a computer-based tool to (1) prospectively determine appropriate rotational and translational motion limits for dynamic targets, (2) retrospectively analyze dosimetric target coverage using tracked positions of individual patient data and (3) visualize both theoretical and actual three-dimensional rotations and translations of the target with respect to a stationary PTV and dose matrix. To demonstrate its utility, we utilized continuous intra-fraction

tracking data of prostate cancer patients treated with radiotherapy. This application, referred to as SWIFTER (Semi-Automatic Workflow using Intra-fraction Fiducial-based Tracking for Evaluation of Radiotherapy), enables the assessment of potentially more effective treatment techniques that simultaneously introduce more risks, such as dose escalation, sub-target boosts and reduced-margin treatment planning.

2.2 Materials & Methods

2.2.1 Real-time Tracking System

Real-time electromagnetic tracking has recently been introduced into clinics for use of target localization, both before and during treatment. This technology utilizes continuous tracking to monitor the target isocenter position, and is used clinically to enable beam-hold interventions (i.e. suspending radiation delivery while the target is outside the path of the beam). The Calypso® 4D Localization System (Varian Medical Systems, Inc., Seattle WA) uses an electromagnetic array to track passive Beacon® electromagnetic transponders (8.5x1.85-mm glass-encapsulated copper coils) implanted in the patient's tumor. The first clinical application of the Calypso System was in prostate cancer patients. The three-dimensional coordinates of each transponder, with respect to treatment isocenter, are determined from the CT scan taken during simulation. These coordinates are entered into the Calypso System to serve as the planned treatment position. During localization on the treatment machine, the electromagnetic array, a rectangular panel encasing electromagnetic coils, is positioned over the patient's target area. The coils emit a radiofrequency signal to excite the implanted transponders. The transponders then return a signal at a specific frequency, allowing for their positions to be detected at a nominal sampling rate of 10Hz. The system also monitors ambient radiation in the treatment room for synchronization with tracking data, enabling identification of target motion collected during active radiation delivery. Previous studies done by Balter *et al* [42] and Parikh *et al* [43] have documented the submillimeter accuracy of the system (see Appendix for details).

2.2.2 Tracking Data

Prospective Motion Limits. The Calypso System is designed for both set-up localization and continuous monitoring of isocenter position. At the time of initial localization, the Calypso System reports translational shifts and rotational offsets, as compared to the planned transponder positions. The user is allowed to set patient-specific rotational limits for patient set-up. If the system detects target rotation greater than this value, the user is warned during initial localization.

Additionally, the user is allowed to set patient-specific motion limits of translational isocenter movement. The system is designed to warn the user if the isocenter exceeds these limits during treatment. Limits for each axis (lateral, anterior-posterior, and superior-inferior) are set independently, allowing for asymmetrical motion boundaries. Our method is designed to determine the appropriate rotational and translational motion limits for each patient, before treatment. This is done using a computer simulation that identifies the maximum rotation and translation the target can undergo before exceeding its PTV boundaries. The target structure is virtually moved through a set of theoretical rotations/translations and excursions of the displaced volume from the stationary PTV structure are detected in search of optimal motion boundaries. Details of this method are presented in Section 2.2.4.

Retrospective dose analysis. Tracking data from each treatment fraction is stored by the Calypso System on the tracking station. The clinical system at our institution is equipped with supplementary functionality allowing for exportation of individual transponder positions to an external computer. Individual tracking files are exported into an Excel (Microsoft Corporation) spreadsheet via a non-clinical software application. Data exported for each fraction consists of individual transponder and isocenter positions as a function of time. Also included is synchronized radiation detection data. Transponder positions are sampled and recorded sequentially at a nominal sampling frequency of 10 Hz, resulting in reported isocenter positions approximately every 0.1 seconds. This data is used to create a probability density histogram of target rotations and translations for combination with the planned dose distribution.

2.2.3 Treatment Planning System Data

The patient plan is exported from the treatment planning system (TPS) into an external viewing application (Computational Environment for Radiotherapy Research (CERR), Washington University, St Louis, MO) [44]. The CERR application is designed to import contours, beams, dose and images from both RTOG and DICOM formats for conversion into a common MATLAB (Mathworks, Natick, MA) data structure. This feature enables universal compatibility with any treatment planning system with RTOG or DICOM export functionality.

The clinical target volume (CTV) contours from CT simulation are extracted and used as the mobile target structure. The PTV structure is designated as the bounding structure which is used as a constraint on the CTV to determine appropriate motion limits. Alternately, a bounding structure can be generated from an isodose line to form a dose rind in order to constrain the target structure to a dose boundary. The three-dimensional dose array is used for dose computation. Multiple treatment prescriptions are supported to accommodate treatment plans that include two treatment volumes.

2.2.4 The SWIFTER Application

A MATLAB (vR2006b) computer program was written to process and analyze treatment plan and point-based tracking data. This application automatically extracts information from the plan to register the structures, dose, and absolute transponder data to the treatment room reference frame. The data flow and functionalities are summarized in Figure 2.1.

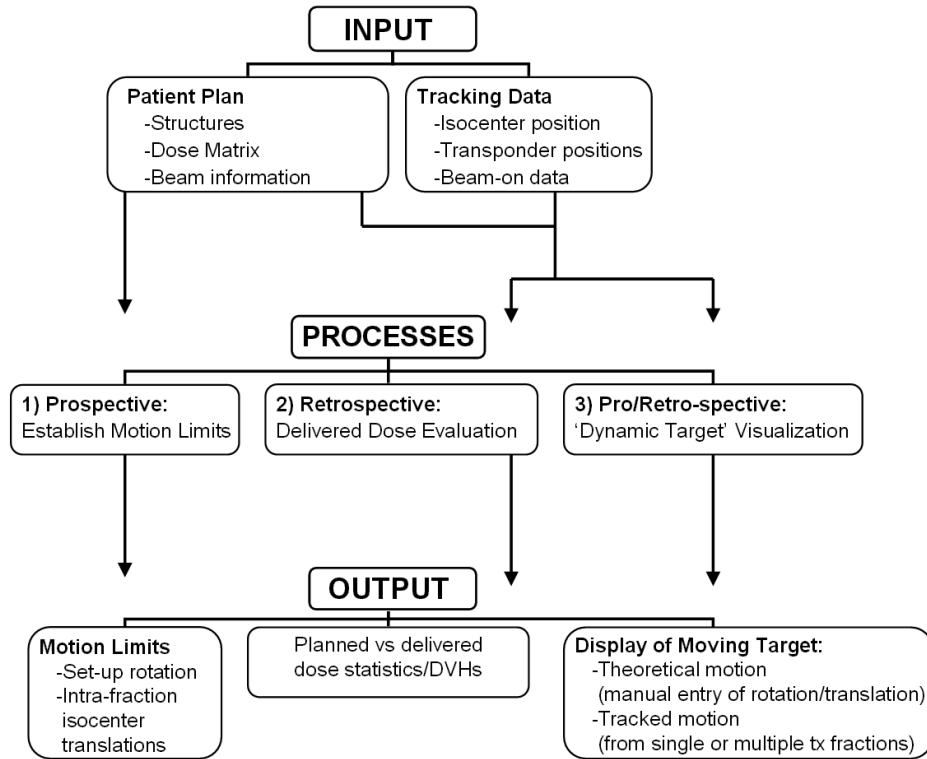


Figure 2.1 Flowchart of input data, application processes, and output data for SWIFTER.

Prospectively determining patient-specific motion tolerances. First, prospective motion limits can be established. Rotational set up tolerances are assessed by virtually moving the structure through a series of theoretical rotations and translations. A binary approach is used to judge appropriateness of rotational limits. When the target structure is detected as exceeding the bounding structure’s volume, the motion condition is flagged. Because real-time target rotations are not reported during treatment and therefore are not used as criteria by which intra-fraction radiation delivery is held, the SWIFTER application is programmed to assume set-up rotation as a systematic offset when testing translational motion limits. By testing translational and rotational limits concurrently, SWIFTER is able to detect conditions where an intra-fraction translation or rotation might push the prostate out of the PTV. An example of such a condition is shown in Figure 2.2. Patient-specific translational tolerances that compensate for geometric misalignments caused by target rotations during treatment are established by SWIFTER.

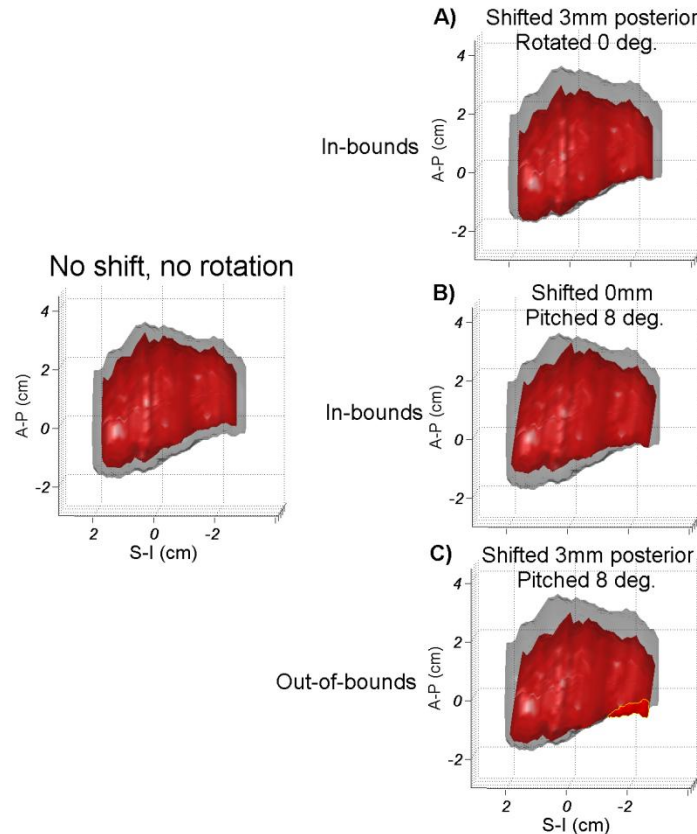


Figure 2.2 Example of a condition where a combination of rotational and translational motion would push the prostate (red structure) out of a 3 mm PTV margin (gray structure): (A) prostate is within the PTV for a 3 mm shift (no rotation); (B) prostate is within the PTV for 8° rotation (no shift); (C) prostate falls out of the PTV when rotated 8° and shifted 3 mm. SWIFTER tests all three cases to detect such conditions.

These translational motion limits are also assessed by binary pass/fail criteria. SWIFTER identifies conditions when the target structure exceeds PTV boundaries. Since there is no way of directly controlling intra-fraction rotation during treatment, the application attempts to reduce translational motion limits before reducing rotational limits in efforts to minimize the volume of the target outside the bounding structure. Several PTV margins can be tested (e.g. 3 mm, 5 mm, 8 mm) to decide on the most appropriate one to encompass theoretical rotations. A set of theoretical rotations encompassing a range of common rotations observed during patient treatment was established from a dataset of inter- and intra-fraction prostate rotations.

Approximately 30 h of tracking data collected from a group of ten prostate cancer patients was analyzed. A range limited within two standard deviations of the mean of rotations about each axis (lateral, superior–inferior (S–I) and anterior–posterior (A–P)) was established. Figure 2.3 displays a frequency histogram of this dataset. An upper translational motion tolerance of 3 mm (coinciding with tolerances used for a multi-institutional clinical Calypso study [45]) and a lower tolerance of 2 mm (the minimal allowed setting by the Calypso System) was used for translational motion limit testing. SWIFTER is designed to test combinations in a hierarchical fashion for optimum speed. Large rotations, which are more likely to fail than smaller rotations, are tested first. If the rotation fails, the program ceases testing further translational combinations and continues with the next smallest rotational value.

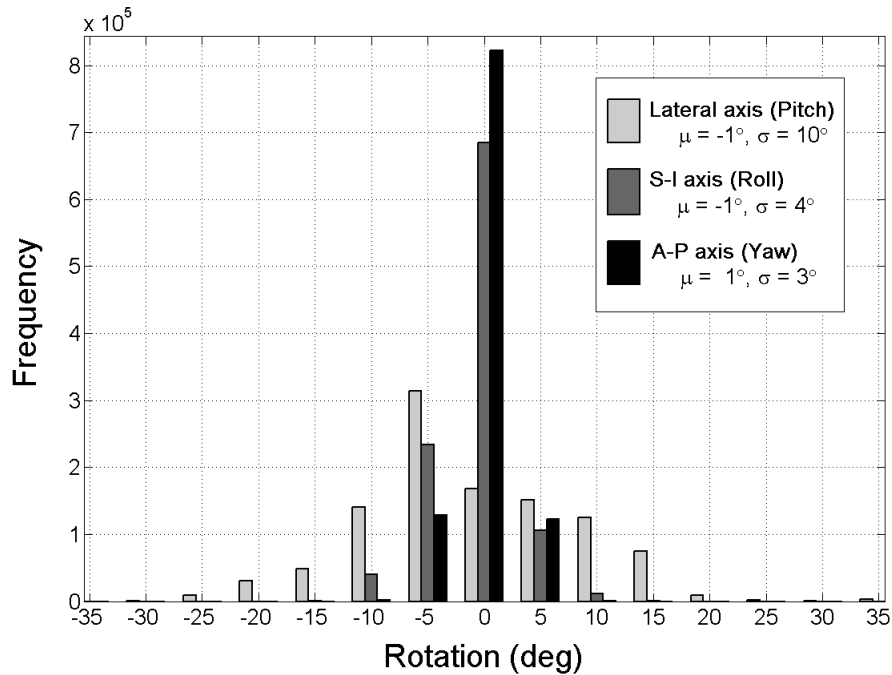


Figure 2.3 Frequency histogram of inter- and intra-fraction prostate rotations (difference from planned position) about the lateral, S–I and A–P axes.

Retrospectively estimating delivered dose. Next, SWIFTER is designed to perform dose computation using patient tracking data to estimate dose delivered to the target during treatment. Dose computation could potentially be performed after each treatment fraction. SWIFTER is designed to allow for combination of previous analysis with the ‘dose of the day’ to provide accumulated dosimetric effects. Consequently, the delivered dose distribution can be monitored throughout treatment to detect poor plan efficacy before a large dosimetric impact is incurred (Figure 2.4).

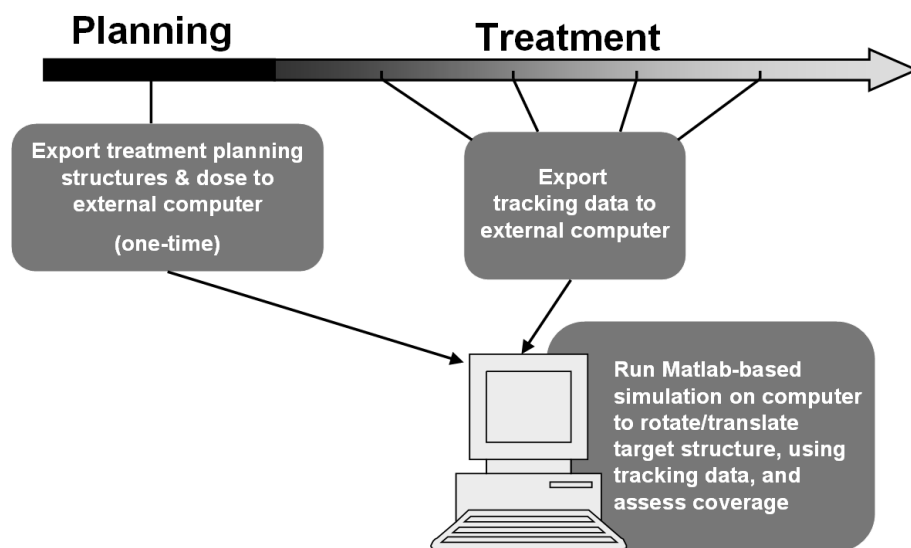


Figure 2.4 Workflow for SWIFTER's retrospective dose analysis.

Tracking data exported from the system is applied to the target structure. Translational motion of the isocenter is reported by the Calypso System, however explicit rotation data is not. Rigid rotations are calculated by SWIFTER by minimizing the fiducial registration error using a least-squares method. Three-dimensional rotations and translations with resolutions of 1 degree and 0.05cm, respectively, are binned into a six-dimensional frequency histogram.

The three-dimensional target volume is then virtually rotated and translated within the static dose cloud to each position differentiated by the frequency bins. Thus, for each distinct rotation/translation, every voxel comprising the target structure is displaced to a new location inside the three-dimensional dose array. At each position (bin), the dose to every voxel is recorded and mathematically weighted by the frequency of that positional occurrence. The end product is a matrix of indexed voxels and their accumulated doses, as determined by the amount of time spent at different locations within the dose array. The target structure alone is treated as a dynamic volume, while the rigid body (skin) and surrounding structures are assumed to be static structures.

As tracking data is added daily to SWIFTER for each individual patient, previous results are combined with new analysis in order to calculate cumulative dose to each voxel. Statistics and dose volume histograms (DVHs) are computed on the planned and delivered dose distributions to evaluate the adequacy of the plan under real target motion.

Visualizing target motion. Finally, SWIFTER allows for visualization of the target structure with respect to the stationary PTV and three-dimensional dose array (Figure 2.5). The visualization tool allows the user to manually enter rotations and translations to display the displaced target relative to the treatment room reference frame. Additionally, processed tracking data can be input for visualization of target motion collected during treatment. Sequential positions from tracked data can be read in as a function of time to simulate actual movement of the target under radiation delivery. Processed tracking data can also be read as a frequency table of each target position and the amount of target volume exceeding the PTV. In this manner, the user can visualize the actual target positions as a function of occurrence frequency or percentage of volume excursion. This visualization tool can be used to ensure that the rotations and translations measured by the point-based tracking system are physiologic and do not represent corrupted or flawed data.

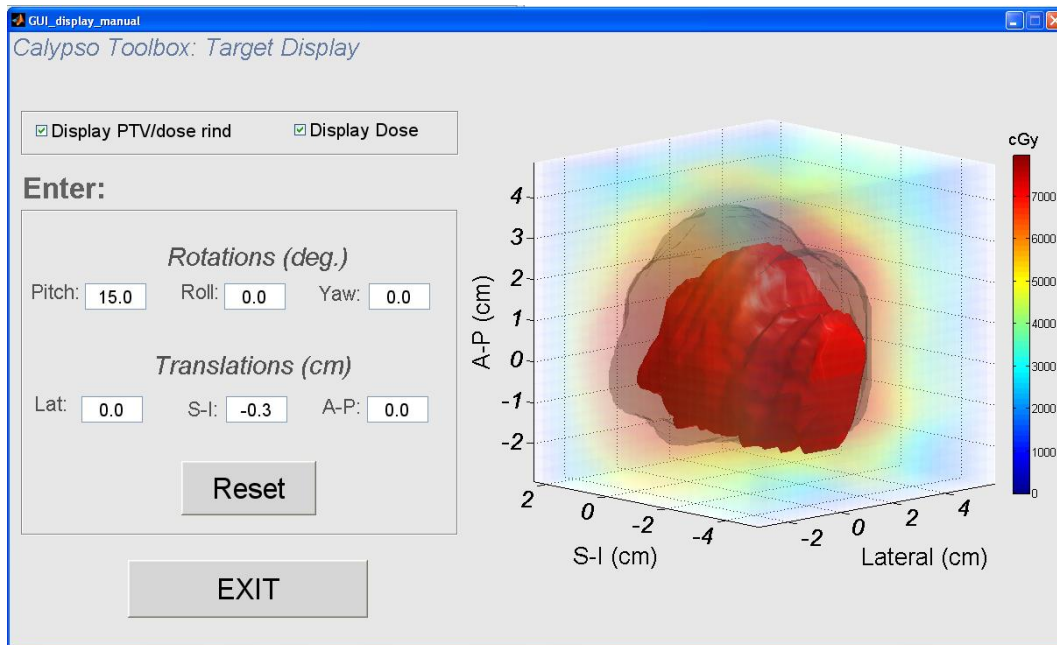


Figure 2.5 Visualization tool of the SWIFTER application for a prostate cancer patient displaying the prostate (red) relative to the PTV structure (gray) and planned dose with a 15° rotation and 0.3cm shift.

2.2.5 Phantom Study

A phantom study was conducted to validate the process in its entirety (including data transfer, coordinate transformation, calculation of rotations, dose analysis, etc). The accuracy of dose computation for a structure under the influence of rotational and translational offsets was tested using controlled phantom tracking data and a patient treatment plan.

The data (structure set, plan information and dose matrix) from a seven-field intensity modulated radiation therapy (IMRT) prostate treatment plan was exported from the Pinnacle treatment planning system (TPS) (v8.0 m, Philips Medical Systems, Madison, WI) into the SWIFTER application. To ensure the accuracy of SWIFTER's dose computation in both high and low-dose areas and over high gradient regions of the dose distribution, we performed testing with a structure encompassing a larger area of the treatment volume (as opposed to simply the high-dose target area surrounding the prostate). For this reason, the skin contour was designated as the dynamic target structure for dose computation.

Tracking data was obtained using a $10 \times 10 \times 13$ cm³ cubic phantom (QA Fixture—Varian Medical Systems, Inc., Seattle, WA) embedded with three Calypso transponders. The phantom was imaged on the Philips Brilliance 64-slice CT scanner (Philips Medical Systems, Cleveland OH) with 1.5 mm slice thickness, and the image set was transferred to the Pinnacle TPS. The isocenter position (identified from external marks on the phantom surface) and transponder locations obtained from CT images were entered into the Calypso System and the phantom was localized and tracked on the treatment machine. The phantom was translated ± 1 cm from the isocenter to offsets in the S–I, lateral and A–P directions and each position was separately tracked (six tracking sessions in total). The phantom was then re-aligned to the isocenter and tracking was repeated while the phantom was rotated $\pm 20^\circ$ (verified with a digital level) about each axis using a Styrofoam wedge. In total, tracking sessions were collected for 13 different positions: 0 cm/ 0° (no shift), ± 1 cm/ 0° along each axis (six total) and 0 cm/ $\pm 20^\circ$ about each axis (six total). Transponder data was exported from the Calypso System for input into the SWIFTER application, and the resulting dose theoretically delivered to the skin contour was computed for each tracking session.

For three-dimensional evaluation of the accuracy of the SWIFTER application, axial, sagittal and coronal isocentric dose planes (1 mm dose grid spacing) were exported from the TPS and SWIFTER to a commercial quality assurance analysis software (OmniPro-*P*mRT v1.6, IBA Dosimetry, Germany). Each translated or rotated dose plane exported from our application was compared to the static dose plane (from the TPS), which was virtually translated/rotated by ± 1 cm/ $\pm 20^\circ$ using the OmniPro-*P*mRT software application (Figure 2.6). Planes were analyzed using the Gamma method (tolerance of 1 mm/1%, see Appendix) and computation of percent dose difference inside a region of interest defined by the skin contour.

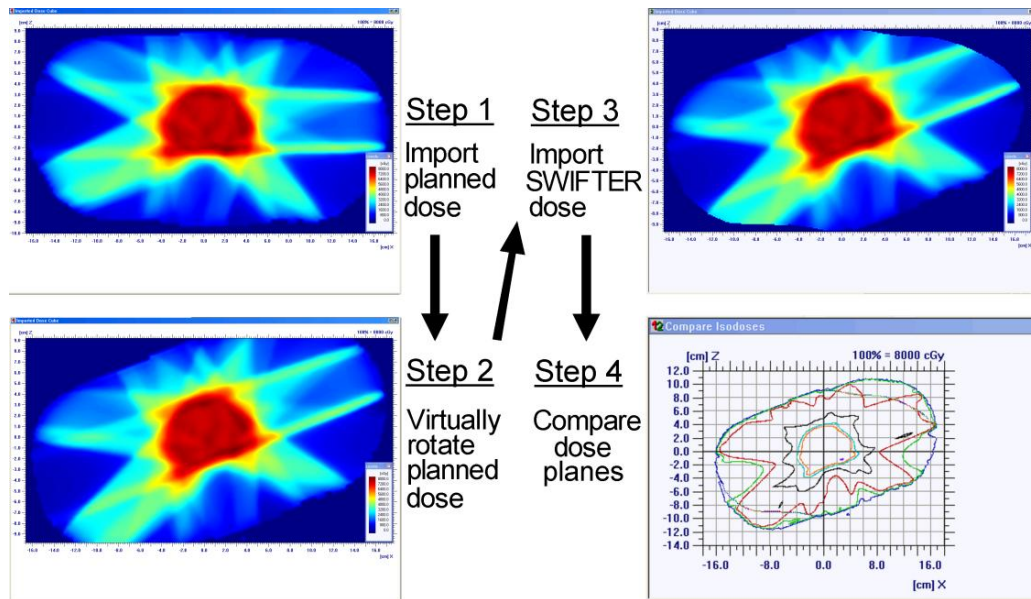


Figure 2.6 SWIFTER phantom validation. Screenshots from the commercial QA software showing the validation process by isodose comparison of axial dose planes (20° rotation) between the TPS and SWIFTER. Step 1: import the dose plane from the TPS into the commercial QA software; step 2: virtually rotate the planned dose plane 20° using the commercial QA software; step 3: import the dose plane analyzed by SWIFTER into the commercial QA software; step 4: compare dose planes between SWIFTER and the TPS (rotated). An overlay of isodose lines is shown.

2.2.6 Patient Case Study

The data from a prostate cancer patient treated with a standard seven-field IMRT plan using a 5mm margin PTV was acquired for analysis. A total dose of 75.6 Gy at an energy of 18 MV was planned for delivery over 42 fractions. Contouring and planning was done on a CT data set with 1.5mm slice thickness using the Pinnacle TPS. A magnetic resonance image (MRI) acquired before transponder implantation was used to supplement prostate delineation.

Real-time tracking data using a 3mm action limit for beam-hold (in any individual direction) was acquired from the patient's treatment to assess actual dose delivery. Since the tracking data used for this case study includes intra-fraction beam-hold interventions, it is likely that the dosimetric impact of prostate motion is less severe than for a case including no intervention. Tracking data was unavailable for two treatment sessions, so analysis was completed using the remaining 40 fractions. Inter-fractional and cumulative dose computation was performed (using only 'beam-on' motion

data) and planned and delivered dose distributions were compared. Maximum dose (D_{\max}), minimum dose (D_{\min}), mean dose (D_{mean}), and percent of prescription dose covering 95% of the prostate volume (D_{95}) were calculated and used as a metric to assess the coverage and homogeneity of the delivered dose distribution. A plan using a reduced PTV margin of 3mm was generated for additional comparison and dose computation was repeated using patient tracking data. Planned D_{\max} , D_{\min} , D_{mean} , and D_{95} for each plan were comparable at 108.7, 99.6, 102.7, and 100.8 for the 5mm-margin treatment plan and 109.9, 99.8, 102.5, and 100.9 for the 3mm-margin treatment plan. The time required for each step in the dose evaluation process was recorded to assess the time efficiency of our technique.

2.3 Results

2.3.1 Phantom Study

Gamma analysis revealed over 99% of dose points in each plane processed by SWIFTER agreed to within 1mm/1% of dose planes exported from the TPS. The average point-by-point percent difference for all planes was <1%, with a maximum standard deviation of 2%. The mean percentage difference and standard deviation for each analyzed plane are reported in Table 2.2.

Table 2.2 Percent dose difference between dose planes exported from the SWIFTER application ($Dose_{SWIFTER}$) and the TPS ($Dose_{TPS}$). Viewing convention for orientation of rotation (clockwise (cw) or counterclockwise (ccw)) in the axial, sagittal, and coronal planes is defined as: view from feet, view from left, and view from above (respectively).

Analyzed Dose Plane	Shift	Percent Dose Difference ($Dose_{SWIFTER} - Dose_{TPS}$)/ $Dose_{TPS}$	
		Mean (%)	Std Dev (%)
Axial	<i>None</i>	0.2	1.0
	+1cm (left)	0.2	0.9
	-1cm (right)	0.2	0.9
	+20° (cw)	0.4	1.9
	-20° (ccw)	0.4	1.7
Sagittal	<i>None</i>	0.8	1.7
	+1cm (ant.)	0.8	1.7
	-1cm (post.)	0.8	1.7
	+20° (ccw)	0.8	2.0
	-20° (cw)	0.8	2.0
Coronal	<i>None</i>	0.3	1.7
	+1cm (sup.)	0.3	1.7
	-1cm (inf.)	0.3	1.7
	+20° (ccw)	0.9	2.0
	-20° (cw)	0.9	2.0

2.3.2 Patient Case Study

The transfer of patient plan data (dose, plan, structures) from the TPS to an external computer in MATLAB-based format required approximately 10 ½ minutes. The determination of appropriate rotational and translational motion limits was reported within seconds. Processing point-based tracking data for a single fraction (including exportation of tracking data, importation into a MATLAB-based format, data sampling, calculation of rotations, and distribution of positions into frequency bins) required approximately 5 minutes. On average, an additional 2 to 5 minutes was required to complete dose computation for each individual fraction. This value varied depending on the number of positional bins. Table 2.3 displays each process and its associated time requirement for dose evaluation of a treatment single fraction. Cumulative dose computation for 40 fractions was completed in 80 minutes.

Table 2.3 Approximate time requirement for each process in the SWIFTER application (on a per-fraction basis). The shaded process indicates a task performed only once. Approximate total time for cumulative dose computation of 40 fractions is 80 minutes.

Frequency	Process	Sub-processes	Time	
Per patient (one-time)	Transfer of Patient Plan Data	Export Patient RTOG plan, dose, & structures	½ min	10 ½ min
		Import plan data into CERR/MATLAB	10 min	
Per tx fraction	Transfer & Processing of Patient Tracking Data	Export tracking data	(seconds)	7 – 10 min
		Import into Excel	1 min	
		Read Excel	¼ min	
		Process Bin Positions	3 ½ min	
	Dose Computation & Analysis	Dose computation Generation of dose statistics	2 – 5 min (seconds)	

The average translational position of the isocenter during radiation delivery (while the treatment beam was on) was 0.0 cm in the lateral, S-I, and A-P directions. The range of motion for each axis was -0.6 to 0.2 cm, -0.8 to 0.5 cm, and -0.4 to 0.7 cm, respectively. Rotational motion during radiation delivery was largest around the lateral axis (pitch), with a mean of 8° and a range of -7° to 27°. The average rotations around the S-I and A-P axes (roll and yaw, respectively) were within 2°.

The delivered D_{max} , D_{min} , D_{mean} , and D_{95} to the prostate expressed as percentages of the prescription dose were 106.5%, 98.7%, 102.7%, and 101.3% (respectively) for the 5mm-PTV plan. These values agreed to within 2.2% of the planned dose statistics. The delivered D_{max} , D_{min} , D_{mean} , and D_{95} values for the 3mm-PTV plan were generally similar at 106.9%, 91.5%, 102.5%, and 101.0%, respectively. All values for the 3mm-PTV plan, with the exception of D_{min} , were within 2.1% of the planned dose statistics. The delivered D_{min} was 8.3% lower than the planned D_{min} . Figure 2.7 displays a three-dimensional representation of the prostate volume and the planned and delivered dose to the target. A concentration of low-dose voxels is found at the posterior portion of the prostate apex for the delivered dose distribution, indicating that part of the volume was not adequately covered.

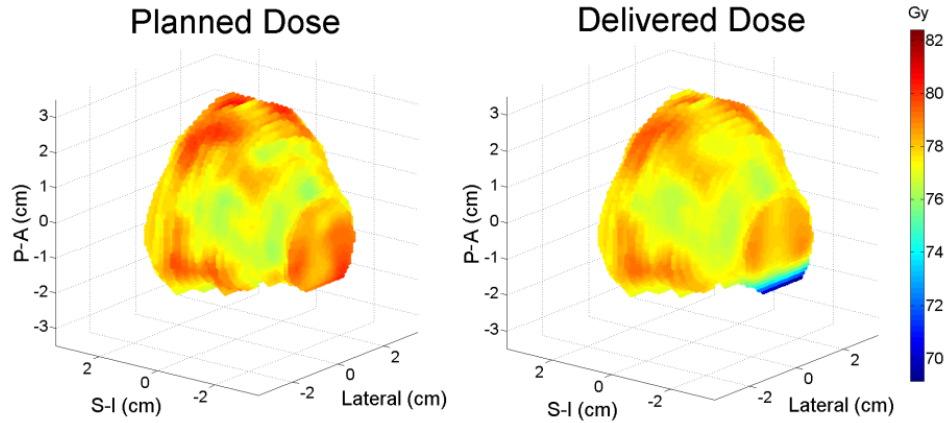


Figure 2.7 Three-dimensional representation of the prostate structure surface and planned (left) and delivered (right) dose distribution for 3mm-margin plan.

Computation of dose statistics for individual treatment fraction revealed increased inter-fraction instability of D_{\max} and D_{\min} as compared to D_{95} (Figure 2.8), particularly for the 3mm-PTV plan. D_{\min} experienced the greatest instability across all treatment fractions with a standard deviation of 8.0% for the 5mm-PTV plan and 12.2% for the 3mm-PTV plan (Table 2.4).

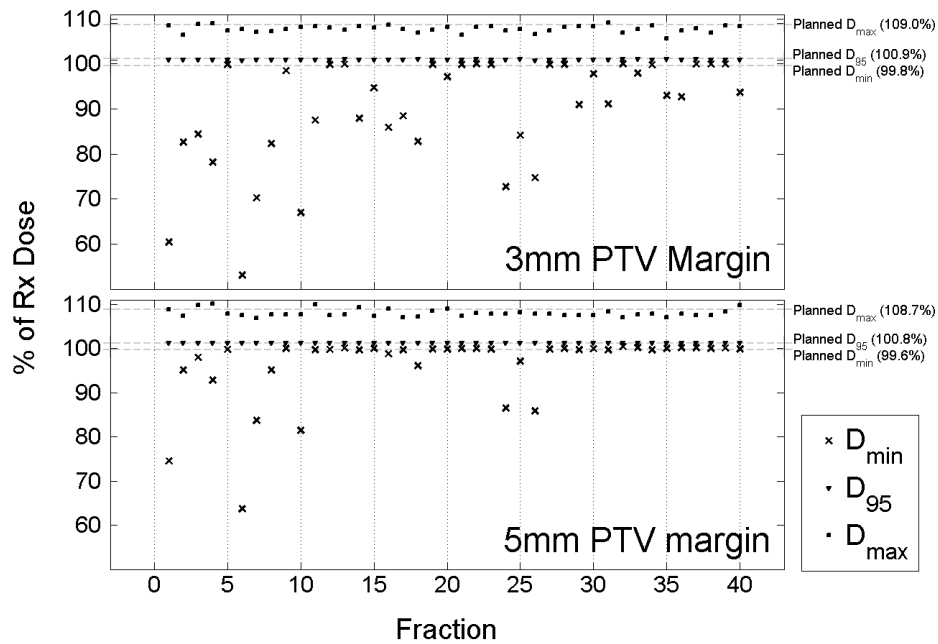


Figure 2.8 D_{\min} , D_{\max} , and D_{95} of the prostate for each individual treatment for the 3mm-margin and 5mm-margin plan. Dose values are expressed as a percentage of the prescription dose.

Table 2.4 Mean and standard deviation of dose statistics over 40 fractions (planned and delivered) for the prostate for both 5mm-PTV and 3mm-PTV IMRT treatment plans.

Metric	5mm PTV margin		3mm PTV margin	
	Mean (%)	Std Dev (%)	Mean (%)	Std Dev (%)
D_{\max}	108.0	0.8	107.8	0.8
D_{\min}	96.2	8.0	89.7	12.2
D_{mean}	102.7	<0.0	102.5	0.1
D_{95}	101.2	<0.0	100.9	0.1

2.4 Discussion

The development of methods to mitigate uncertainties presented by daily target localization is ongoing. Evaluation of target coverage from daily dose delivery can provide increased certainty in treatment efficacy and help enable adaptive planning decisions. This is demonstrated by the patient case study presented here. Computation of cumulative dose delivery indicated a considerable drop in the minimum dose to the prostate from a 5 mm to 3 mm PTV margin treatment plan. While potentially adequate coverage might be offered by the 5 mm PTV margin treatment plan over a 40-fraction treatment course, it is important to consider the effect of a hypo-fractionated treatment scheme for such a patient. For example, the variability observed in the D_{\min} over the first ten fractions indicates a possible under-dosing to the prostate during the beginning of treatment. This would cause an exaggerated effect of a hypo-fractionated treatment scheme. It should be taken under consideration that the dosimetric effects presented in this patient case include intra-fraction beam-hold intervention. Dose computation of an intervention-free treatment might have revealed a larger dosimetric miss. Incorporation of daily target coverage review would help enable an inter-fraction intervention before a large dosimetric impact is incurred.

For clinical use as a dose delivery evaluation tool, this application can provide increased confidence for radiation treatment [16, 17]. It can be used for point-based dose evaluation for any anatomical targets impacted by intra-fraction motion, such as lung and abdominal tumors. However, it is a notable limitation that point-based localization may not be sensitive to volumetric deformation of the target and nearby tissues, which may be more or less concerning depending on the target site.

Evidence suggests that the prostate, for example, can be adequately represented by point-based information. A study done by van der Wielen *et al* found that deformation of the prostate with respect to intraprostatic fiducials was small [46]. Additionally, Deurloo *et al* reported that the magnitude of prostate deformation is secondary compared with organ motion and intra-observer variability in target delineation [47]. However, the magnitude of motion and degree of deformation of thoracic and abdominal targets elevates the complexity of estimating dose delivery. Thus, the application of the method described here for thoracic and abdominal targets may call for the development of specialized anatomic models.

There are some clear advantages of using point-based localization data rather than volumetric localization data. While fiducial-based methods provide limited knowledge of the daily dosimetric impact on normal tissues, analytical efforts are focused on target anatomy in the high-dose region. The large amount of data provided by volumetric imaging entail that additional efforts are not required for a point-based technique. However, there is no doubt that as compared with point-based techniques, image-guided techniques can provide a substantial amount of information about the position and geometry of the target and nearby tissues.

One of the most significant advantages of utilizing point-based tracking data for dose delivery evaluation is the incorporation of intra-fraction motion. Adaptive radiation therapy techniques using volumetric imaging alone have historically been limited to pre- and post-treatment sampling, relying on the condition that the internal anatomy remains stationary between the time of image acquisition and the end of treatment. It is well documented that the mobile targets can experience intra-fraction movement ranging from several millimeters to a few centimeters [18]. Without the use of intra-fraction tracking, the magnitude and impact of this motion is unknown.

The SWIFTER application has proven clinically valuable for reduced-margin prostate radiotherapy. Our group published work on its use for a clinical patient cohort and found that SWIFTER was able to diagnose undertreatment for 3/15 patients planned with reduced PTV margins [17]. Through an industrial collaboration with Philips Medical Systems, the SWIFTER application has been converted to a commercial platform for integration into a clinical environment. This application has been

patented and is available for use [48]. It has since been used in our clinical as a dose monitoring tool for hypo-fractionated prostate treatments. Future work is planned for its use for assessing dose to lung cancer patients tracked with point-based localization.

Work to develop real-time volumetric imaging is also underway, and may provide significantly more anatomical information for dynamic targets and the surrounding anatomy. Onboard MRI is a new technology that may offer enhanced spatial resolution while maintaining acceptable temporal resolution for real-time tracking. It may also provide better anatomical visualization for improving pretreatment targeting accuracy. To date, onboard MRI has yet to be used in a clinical setting during radiotherapy, and its value for treatment improvement still remains to be seen. This exciting new technology is the focus of the next chapters of this work.

Chapter 3

MRI for Localization of Targeted Anatomy and Critical Structures

The effective administration of radiotherapy treatment relies on accurate identification and localization of the target and surrounding healthy tissues both during treatment planning and during daily treatment delivery. The limited soft tissue visualization provided by computed tomography (CT), the standard imaging modality for treatment planning and daily localization, has motivated studies on the use of MRI for better characterization of soft tissue targets [7]. Supplementing radiation treatment planning with MR images can offer better anatomical information and greatly improve the identification of tissue borders, thus improving targeting [9-12]. Furthermore, if acquired just before treatment, such information can be used to modify the planned treatment dose to compensate for daily positional variations - a technique known as Adaptive Radiation Therapy (ART). Emerging technologies may enable MRI-based planning, dosimetry, daily localization and ART in the near future, however it remains to be seen if MRI-based radiotherapy offers significant treatment improvement. Here, work is presented investigating the use of MRI for target positioning using novel onboard MRI technology, with specialized focus on the application of MRI for localization of abdominal tissues. This work is comprised of two parts. The first is a study on the use of MRI for localization of healthy tissues for treatment planning of abdominal sites. The second is a study of low-field onboard MRI for visualization of targeted anatomy and critical structures.

3.1 Segmentation Precision of Abdominal Anatomy for MRI-based Radiotherapy

3.1.1 Background & Significance

It is well-known that X-ray based imaging, the standard imaging modality for radiotherapy planning and pre-treatment setup, offers limited visualization of soft-tissue boundaries [7]. The application of magnetic resonance imaging (MRI) to aid in tissue visualization during planning and pre-treatment localization carries significant implications for many treatment sites. The benefits of utilizing MRI for treatment planning of targets in the head, central nervous system, and pelvis have been well-established [7, 9-12]. Supplementing computed tomography (CT) planning images with MR images for planning has been shown to result in more precise delineation in these sites, enabling better targeting and normal tissue sparing [9-12]. Such findings have motivated the development of MRI-only planning [7] and onboard MRI devices for treatment localization or adaptive treatment [13-15], rendering MRI-based radiotherapy a current focus of clinical interest.

Despite large research efforts for many sites, there have been few investigations on the use of MRI for radiotherapy planning of abdominal cancer, a disease for which improved soft tissue targeting could offer considerable benefit. Cancer of the pancreas, liver, and other abdominal sites have historically demonstrated poor treatment prognosis and high mortality rates. Surgical resection is widely regarded as the only curative technique available, however many patients are diagnosed at advanced stages of disease making them poor surgical candidates [49-51]. Studies have indicated that dose escalation strategies offer more effective treatment of abdominal tumors compared to conventional radiotherapy, especially if normal tissue toxicity is minimized using accurate targeting [49, 51]. However, accurate targeting during CT-based planning and pre-treatment localization is particularly challenging for abdominal sites, which are mostly comprised of soft tissue.

There has been recent interest in the use of MRI for improved delineation of abdominal targets, and evidence from several studies supports this proposition [52-54]. A study of 23 patients with liver tumors performed by Voroney *et al* found significant differences in target size when tumors were imaged with CT as compared to MRI [54]. Another study of 21 liver cancer patients (Dawson *et al*) concluded that tumor volumes defined on MRI were larger than those defined on CT, suggesting that some disease may be missed when using only CT images for target delineation. Authors concluded that MRI can detect tumor extension that CT cannot [52]. Romero *et al* compared pathologic tumor size to that defined on MRI for 13 patients with colorectal cancer and found that MRI provided good agreement with actual tumor size [53].

These investigations highlight the potential advantage of using MRI for target delineation in abdominal cancer patients, which may provide more accurate representation of the tumor without the use of ionizing radiation. This advantage also makes MRI a particularly attractive option for daily radiotherapy localization. However, despite these promising findings, MRI-based radiotherapy for abdominal sites has remained largely unstudied. Currently, there is no evidence that MRI-based segmentation of abdominal anatomy achieves adequate delineation precision for planning and localization. In fact, there is no evidence at all of the utility of MRI for abdominal tissue segmentation for radiotherapy. In this study, we evaluate the use of abdominal MR images for segmentation by characterizing the inter- and intra-observer precision of normal tissue delineation on MR images. Two MRI sequences are evaluated: the first is a commercial scan sequence specifically designed for motion compensation, and the second is a sequence optimized for acquisition using a breath-hold method. By assessing the segmentation precision of abdominal anatomy offered by MRI, we aim to gain insight into its potential utility for planning and localization of abdominal cancer patients.

3.1.2 Materials & Methods

Subjects and Imaging. Fourteen healthy subjects enrolled on an IRB-approved protocol were imaged on a 1.5T Philips Intera MR scanner (Philips Healthcare, The Netherlands). The subject sample was 57% male, with a mean age of 30 years ($\sigma=9$ years) (Table 3.1). For imaging, each subject laid flat on the MR table head-first supine with arms above their head, and a MRI coil was

secured to their abdominal surface. The built-in body RF coil was used for RF transmission, and a four-channel pelvic phased-array coil was used for signal receiving. A pneumatic belt was used to monitor patient respiratory motion, for synchronization with MR imaging. During each subject's one-hour imaging session, two different volumetric MR sequences were obtained. The first was a commercial T2-weighted (T2W) sequence specifically designed for motion compensation (triggered at exhalation, 2377.9 ms repetition time, 70.0 ms echo time, 90° flip angle, 2.5mm slice thickness, 1.4mm in-plane resolution). T2W sequences are often used for imaging of liver lesions since they are particularly well-suited for evaluating tumor margins and internal structures [55]. The second was a balanced fast field echo (BFFE) sequence acquired with a breath-hold technique (4.3 ms repetition time, 2.1 ms echo time, 60° flip angle, 2.5mm slice thickness, 1.4mm in-plane resolution). MRI sequences that enhance the visualization of fluids, like the BFFE sequence, are extremely useful for visualization of the pancreatic and bile ducts [55]. The BFFE sequence is also very fast, making it well-suited for breath-hold acquisition. In total, 28 imagesets of abdominal anatomy were obtained from the group of subjects.

Table 3.1 Subject sample characteristics.

Characteristic	Percentage (Frequency), unless otherwise noted
Gender	
Male	57.1 (8/14)
Female	42.9 (6/14)
Ethnicity	
Caucasian	57.1 (8/14)
East Asian	28.6 (4/14)
Indian	14.3 (2/14)
Mean Age, Range	30 years, 20-54 years

Segmentation. After acquisition, the two abdominal MR imagesets acquired from each subject were loaded into a clinical treatment planning system (Pinnacle v9.0, Philips Healthcare, Madison WI) for segmentation of normal tissues. Three independent observers performed manual segmentation of eight normal structures generally accepted as standard abdominal organs at risk (OARs): liver, stomach, duodenum, pancreas, spleen, bowel, kidneys, and spinal cord (Figure 3.1). The spleen of one subject was not contoured due to a previous splenectomy. Observers were blinded details of the MR imagesets and subjects, other than the MR sequence used to obtain the imageset (T2W or BFFE).

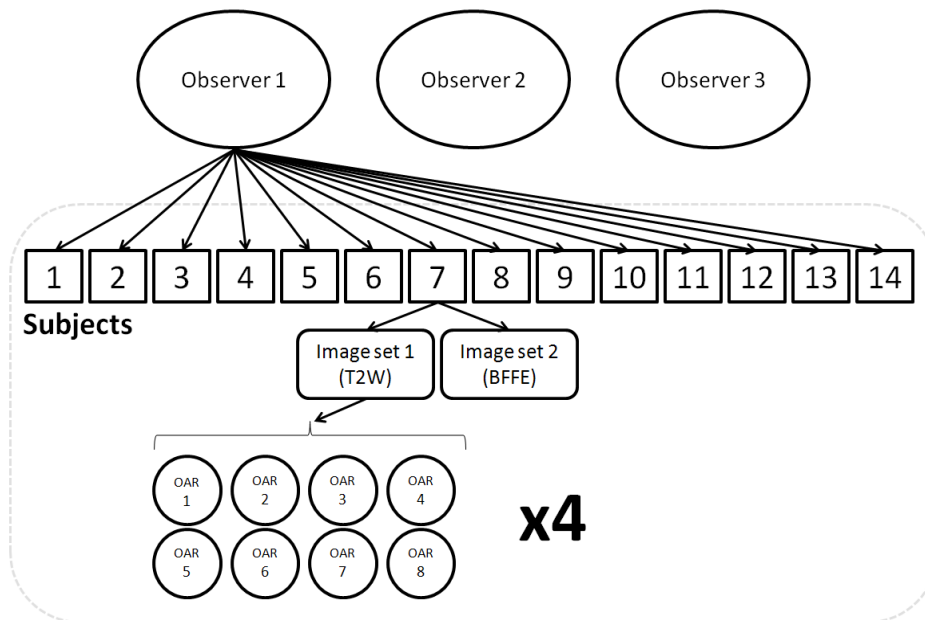


Figure 3.1 Schematic of OAR segmentation for a single observer. Each trial is performed four times.

To ensure a standardized approach was used across observers, each was provided with standard instructions for organ delineation (for example, to contour ‘bowel-in-a-bag’, as opposed to contouring individual bowel loops). Observers were permitted to use any basic contouring tools used in clinical practice, including ‘sparse contouring’ (interpolation between manually contoured slices), automatic intensity thresholds, and copying contours onto adjacent slices. All observers performed manual editing following the use of any of the aforementioned automated planning tools. In this manner, observers were required to ensure that any automatically generated contour points agreed with their interpretation

of the appearance of the anatomy. Furthermore, all contours were reviewed by a single observer independently to detect any gross contouring errors (eg. missing slices). Any gross errors detected during the review process were corrected by the respective observer.

To investigate intra-observer precision, observers were asked to contour each of the 28 imagesets four separate times (Figure 3.1). Each contouring session (herein referred to as ‘trial’) occurred at least one week apart. The assigned order in which the 28 imagesets were contoured by each observer was randomized. Additionally, standard imageset window/level values were set and remained fixed for all contouring trials over all imagesets (T2W: window/level = 300/-20, BFFE: window/level = 190/-20). In total, 2664 structures were contoured by the three observers. The contoured three-dimensional (3D) structures for each imageset were then exported to MATLAB (Mathworks Inc., Natick MA) and analyzed to assess contour precision between contouring trials and between observers.

Precision Measurements. Segmentation precision between contouring trials of the same imageset and organ were assessed by computing three-dimensional (3D) overlap of each of the contoured structures from each trial compared to a baseline. Since there was no ground truth available, a baseline structure was created for each imageset and organ. A baseline volumetric structure of each of the eight OARs was generated with the four trial contour sets using the “Simultaneous Truth and Performance Level Estimation” (STAPLE) algorithm (Figure 3.2) [56]. This algorithm computes a probabilistic estimate of the true segmentation of a structure from a set of contours using an expectation-maximization algorithm. This is a widely accepted methodology often used in similar studies in which no ground truth structure is available [57-59].

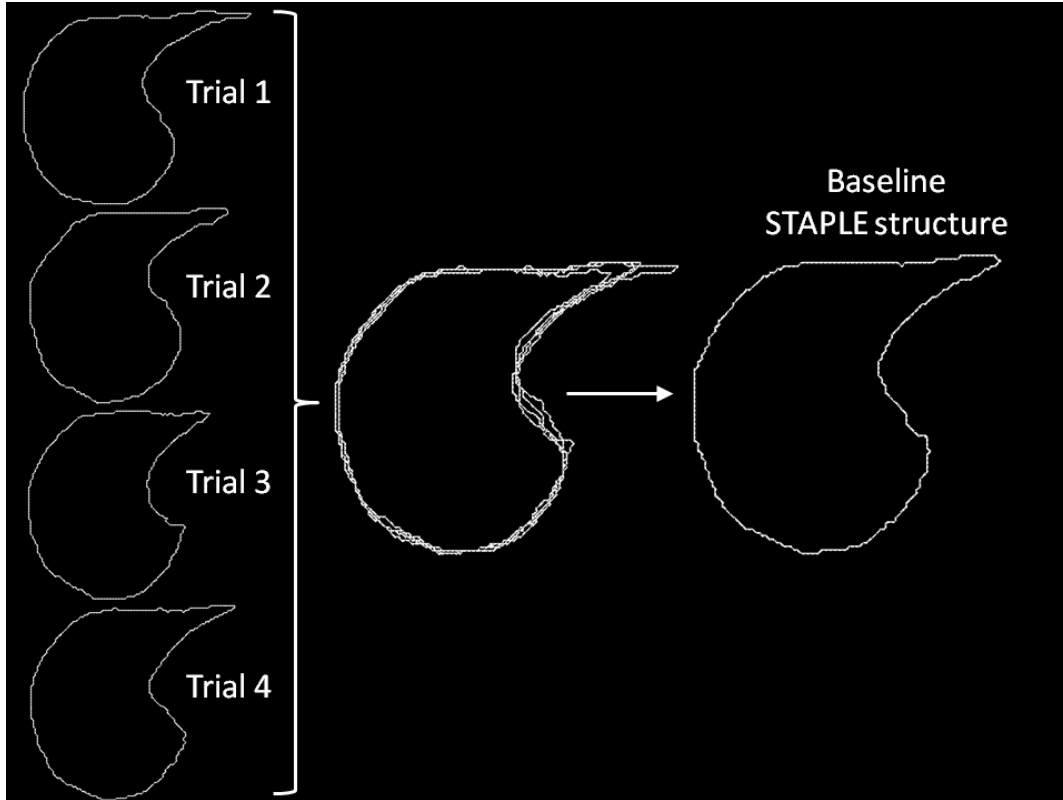


Figure 3.2 Derivation of a baseline liver structure for intra-observer precision analysis using liver structures from four contouring trials from a single observer.

The agreement of each trial structure with the baseline structure was then measured using two metrics: the Dice coefficient and the median two-dimensional (2D) slice-wise Hausdorff distance, which are both common metrics of contour agreement used in segmentation studies [60, 61]. The Dice coefficient provides a measure of volumetric overlap between two 3D structures and is computed as follows (Equation 3.1):

$$Dice\ Coefficient = \frac{2|X \cap Y|}{|X| + |Y|} \quad (3.1)$$

Here, X and Y represent two 3D contour structures. The Dice coefficient ranges from 0 to 1, with a value of 0 indicating no overlap, and a value of 1 indicating perfect overlap. Dice coefficients for each contour structure were compared to a standard literature-based value of 0.7, above which generally indicates a good level of agreement [62].

The Hausdorff distance is used as a metric of surface agreement by providing a measure of the maximum value in the set of nearest distances between two sets of contour points, and is computed as follows (Equation 3.2):

$$\textit{Hausdorff Distance} = \max \left\{ \max_{x \in X} \min_{y \in Y} d(x, y), \max_{y \in Y} \min_{x \in X} d(x, y) \right\} \quad (3.2)$$

Here, X and Y represent two 2D contours on the same axial image slice and x and y represent the finite points contained on contours X and Y . The maximum Euclidean distance between these two sets of points is computed as the Hausdorff distance. Sets containing a contour on only one of the two slices were omitted. As described by similar studies, the median of all Hausdorff distances over all slices was computed [60]. The median is used because it provides a better measure of central tendency for the distribution of Hausdorff distances, which was skewed towards high values (positively skewed) for most structures. Low values indicate a high level of contouring precision, while high values indicate poor precision.

To assess inter-observer contouring precision, the STAPLE structures derived for the four contouring trials were used to represent individual observer structures. For each imageset and structure, an additional baseline structure was derived using a second iteration of the STAPLE algorithm from these three observer structures. In the same manner as above, the Dice coefficient and Hausdorff distance were computed for each observer structure using the new STAPLE structure as a baseline.

Statistical Analysis. Due to the non-normal distribution of precision metrics, non-parametric significance testing was used to identify significant factors affecting contouring precision (indicated by Dice coefficients and Hausdorff distances) over all trials (n=2664). Potential factors included organ, MRI sequence, subject gender, subject age, and subject ethnicity. It was hypothesized that organ and MRI sequence would be significant predictors, while the others would not. Once significant predictors were identified, Dice coefficients and Hausdorff distances were grouped into clinically relevant categories and entered into a multinomial logistic regression model. Odds ratios were computed for each predictor variable and tested for significance. Due to the large variation in size, shape, and tissue contrast of the organ set, odds ratios were specifically computed for each organ.

The Dice coefficient (DC) was categorized as indicating “good agreement” ($0.7 < DC \leq 0.9$), or “great agreement” ($0.9 < DC$). A Dice coefficient of greater than 0.7 is commonly referenced by segmentation studies as indicating a good level of agreement [60-62]. Similarly, the Hausdorff distance (HD) was categorized as indicating “poor agreement” ($5\text{mm} < HD$), “good agreement” ($3\text{mm} < HD \leq 5\text{mm}$), or “great agreement” ($HD \leq 3\text{mm}$). These distance values are complementary to common values often used for treatment planning or setup margins, which helps to define clinically meaningful precision categories.

To assess the reproducibility of segmentation within and between observers, the magnitude of intra- and inter-observer contouring variability was computed. Intra-class correlation coefficients (ICC) [63] were computed for repeated contouring trials (to establish intra-observer variability) and repeated contouring by observers (to establish inter-observer variability) using organ as the grouping class. ICC values range from 0 to 1, and provide an indicator of the level of variability between trials (or observers) when contouring is repeated on a single subject for several different organs. A high value indicates low variability between trials or observers. The intra-observer and inter-observer ICC values were computed for each subject and imageset. Non-parametric statistical testing was used to assess if intra-observer ICC values were significantly different from inter-observer ICC values.

3.1.3 Results

The mean and standard deviation of intra-observer Dice coefficient and Hausdorff distance values were 0.89 ± 0.12 and $3.6\text{mm} \pm 1.5$, respectively. The mean and standard deviation of inter-observer Dice coefficient and Hausdorff distance values were 0.89 ± 0.15 and $3.2\text{mm} \pm 1.4$, respectively. As displayed in Figure 3.3, the mean Dice coefficient for all OARs over all trials was greater than 0.7, while the mean Hausdorff distance was less than 6mm. When organs were ranked according to their mean precision metrics from least to most precise, the duodenum, pancreas, and bowel ranked among the least precise for both metrics (mean Dice coefficient and mean Hausdorff distance), suggesting that they were contoured with the poorest precision. The spinal cord yielded a relatively low mean Dice coefficient, but yielded the best (lowest) mean Hausdorff distance. In contrast, the liver yielded a high mean Dice coefficient, but a relatively poor (low) mean Hausdorff distance.

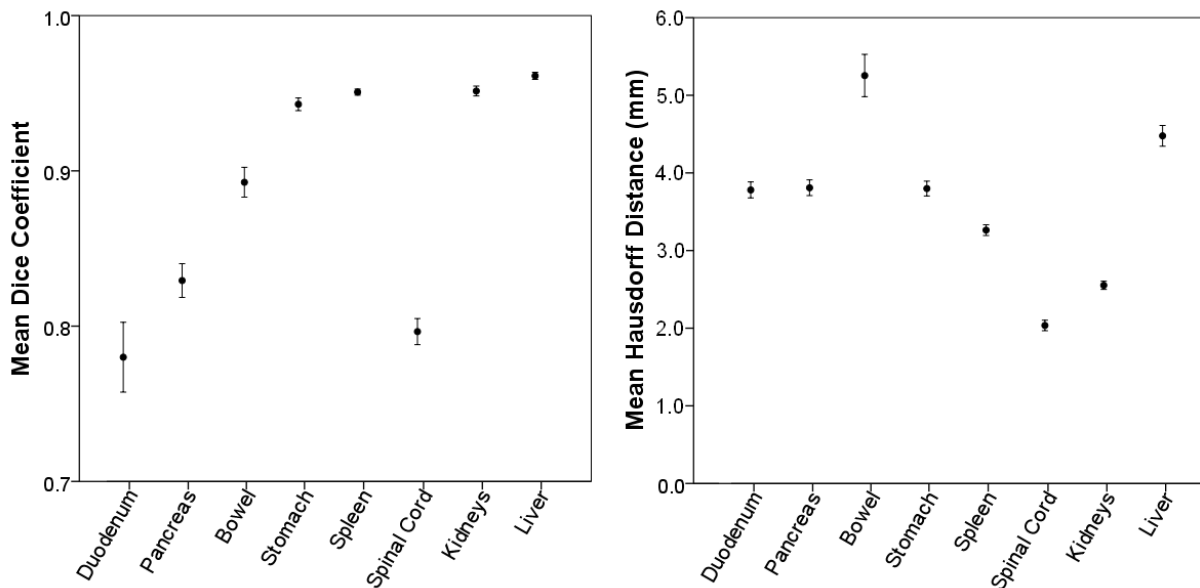


Figure 3.3 Mean Dice coefficients and Hausdorff distances for each organ over all trials with 95% confidence intervals. The Dice coefficient graphical scale is shown here from 0.7 to 1.0, as all mean dice coefficients were > 0.7.

Nonparametric significance testing revealed that organ (Kruskal-Wallis test) and MRI sequence (Wilcoxon Signed-Ranks test) were significant predictors of the intra-observer Dice coefficient and/or Hausdorff distance values (α -level = 0.05). Sample images of T2W and BFFE sequences

with overlaid contours are shown in Figure 3.4. Only organ was a significant predictor of inter-observer precision metrics. Subject gender, age, and ethnicity were not significant predictors (α -level = 0.05) for intra- or inter-observer agreement, and were not included in further logistic regression modeling.

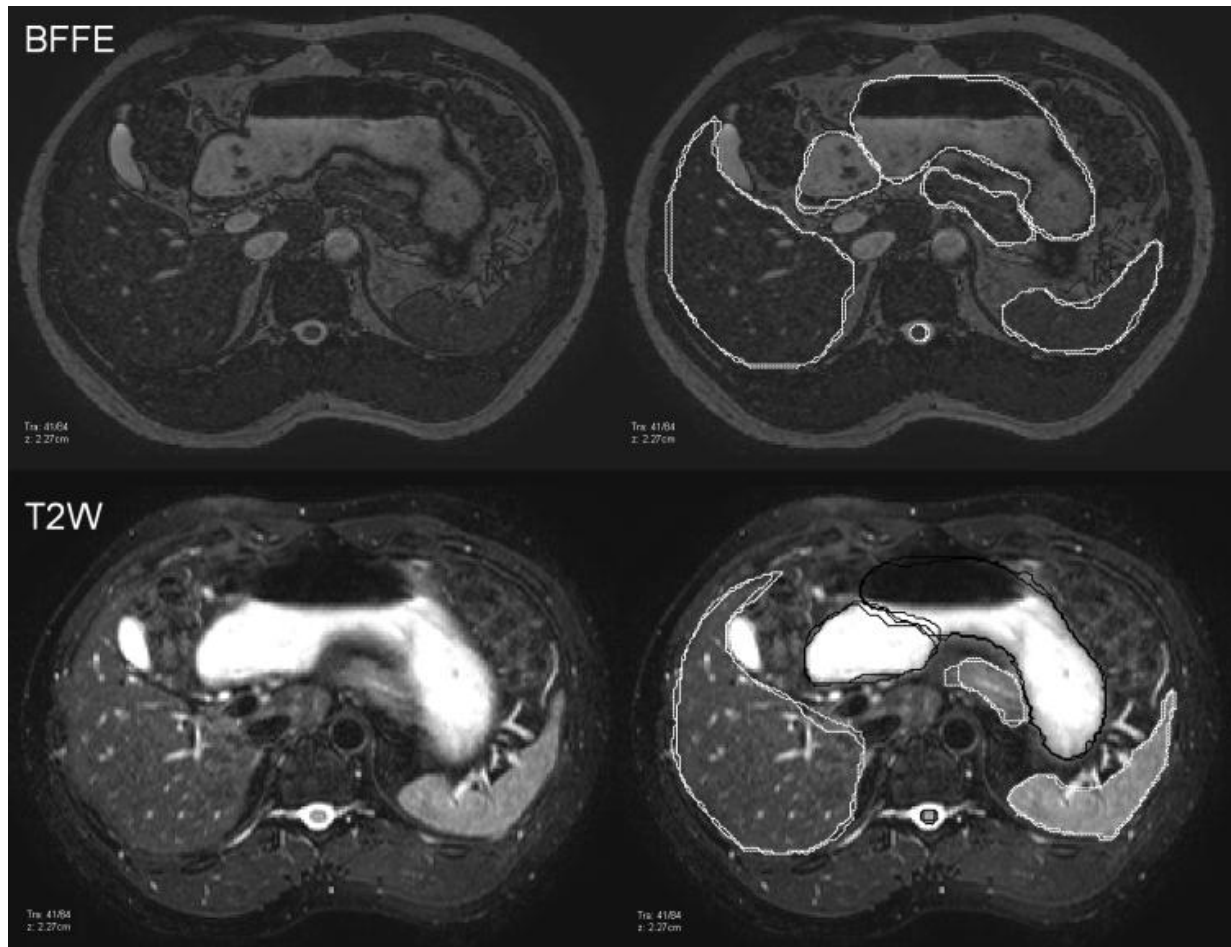


Figure 3.4 Images of a BFFE and T2W sequence for a single subject. Contours for two trials produced from a single observer are overlaid on the right-hand panel. Contours for the stomach, duodenum, and spinal cord produced from a single observer are displayed in black for the T2W sequence to enhance visualization.

Logistic regression modeling revealed that MRI sequence was a significant predictor of poor, good, or great intra-observer agreement in all OARs except for the spleen and kidneys (Table 3.2). In all OARs where MRI sequence was considered a significant predictor of either the Dice coefficient or Hausdorff distance, the BFFE sequence produced higher odds of better precision than the T2W sequence. For example, the BFFE sequence was 2.1 and 3.4 times more likely than the T2W

sequence to produce a “good” and “great” Hausdorff distance (respectively) for segmentation of the stomach (Table 3.2). Differences in intra-observer contour agreement can be easily noticed for the pancreas. Full results with associated odds ratios are displayed in Table 3.2.

Table 3.2 Odds ratios for categorized intra-observer precision metrics, according to MRI sequence.

Organ	Odds Ratio for MRI Sequence (BFFE/T2W)			
	DC		HD	
	Good	Great	Good	Great
Liver	NS	NS	NS	NS
Stomach	NS	NS	2.1	3.4
Duodenum	NS	NS	NS	2.6
Pancreas	2.0	NS	NS	2.7
Spleen	NS	NS	NS	NS
Bowel	6.8	5.3	NS	NS
Spinal Cord	3.2	9.2	NS	NS
Kidneys	NS	NS	NS	NS

DC = Dice coefficient, HD = Hausdorff distance, NS = not significant. The “poor agreement” level is used as the reference category for odds ratio values.

The mean and standard deviation of intra- and inter-observer ICC values for the Dice were $ICC_{DC, intra-} = 0.84 \pm 0.12$ and $ICC_{DC, inter-} = 0.48 \pm 0.18$; the mean and standard deviation of the intra- and inter-observer ICC values for the Hausdorff distance were $ICC_{HD, intra-} = 0.93 \pm 0.07$ and $ICC_{HD, inter-} = 0.86 \pm 0.08$ (Figure 3.5). The intra- and inter-observer ICC values were found to be significantly different using the Mann-Whitney U test (α -level = 0.05), indicating that inter-observer variability is higher than intra-observer variability.

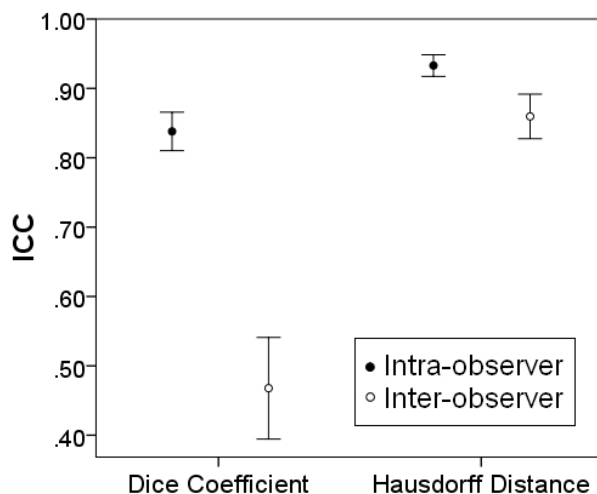


Figure 3.5 Mean intra- and inter-observer ICC values for precision metrics. ICC values for Dice coefficients and Hausdorff distances are significantly different between groups.

3.1.4 Discussion

In the interest of assessing its utility for MRI-based radiotherapy planning and localization, we present the first study evaluating the segmentation precision of abdominal anatomy on MRI. Overall, results indicate that MRI can be used for abdominal organ delineation with a good level of precision (mean DC > 0.7, mean HD < 4mm). The number of subjects ($n = 14$), observers ($n = 3$), contouring trials ($n = 4$), and organs ($n = 8$) investigated in this study amounted to a substantially large amount of data, compared to similar studies for other anatomical sites. While labor-intensive, this study offers an exploratory investigation into the potential use of MRI in abdominal radiotherapy as emerging MRI-based technologies and onboard imaging devices start to become available for clinical use [13-15]. Results of this study support the use of MRI for abdominal radiotherapy planning and localization, as contouring precision was found to be adequate by our metrics.

The use of both the Dice coefficient and the Hausdorff distance as indicators of contouring precision was motivated by the fact that each metric is sensitive to a different geometric property of the segmented structures, collectively providing a good representation of contour agreement. The Dice coefficient, a volume-based metric, is a good indicator of structure overlap. However, it has

been shown to be sensitive to structure size, and is not necessarily a singular robust metric for assessment of a set of structures of various sizes. A brain tumor segmentation study performed by Zou *et al* demonstrates this very issue, and authors suggest that distance based metrics may be a good alternative to the Dice coefficient when spatial information is of interest [61]. We hypothesize that this may be why the spinal cord yielded a relatively poor (low) Dice coefficient, but a very good (low) Hausdorff distance. The Hausdorff distance is an indicator of spatial distance between two structures, and provides a measure that is clinically meaningful in the context of contouring error and setup margins. However, it is sensitive to any discrepancies in trial- or observer-specific delineation preferences of structure boundaries. For example, there were some variations between observers and trials in the extension of the liver contour around the vena cava to include the caudate lobe of the liver. This may explain the relatively large Hausdorff distance reported for the liver (Figure 3.3). It is important to note that the Hausdorff distance takes into account the maximum slice-wise distance between two structures, and therefore is an indication of the largest slice-wise contouring errors per structure, and not three-dimensional contouring errors.

The duodenum and pancreas yielded the lowest precision overall. The duodenum extends from the stomach to the main section of the bowel, and it can be difficult to reproducibly define where this structure connects to these adjacent organs. This may be why the duodenum yielded relatively low and variable precision metric values, as indicated by mean precision metric values and corresponding confidence intervals (Figure 3.3). The pancreas is highly deformable, and perhaps the most inconsistent in shape from person to person of all evaluated OARs [64]. It is likely that the ambiguous and variable nature of the geometry of the pancreas is why resulting precision metrics were relatively poor. Comparatively, the spleen and kidneys, both relatively consistent in boundary and shape, yielded high precision overall. Furthermore, contouring precision was not significantly impacted by any MRI sequence for either the spleen or the kidneys, suggesting that they are generally well-visualized on MRI.

It is not surprising that MRI sequence was a significant predictor of contouring precision, as variations in sequence can dramatically impact the visualization of anatomy. The BFFE breath-hold sequence outperformed the T2W sequence for all OARs which MRI sequence was found to be a

significant predictor. It is not clear whether this is due to the breath-hold nature of MRI acquisition (versus the exhalation-triggered nature of the T2W acquisition) or due to the visualization offered by the sequence itself, but this finding underscores the need for site-specific sequence optimization. Future studies comparing different types of motion-compensation methods for abdominal imaging would be very useful to this end.

Abdominal sites are of great interest for these types of MRI-based radiotherapy, as they could experience substantial benefit from better soft tissue targeting [49, 51]. The work presented here demonstrates that segmentation of abdominal tissues on MRI can be performed with good precision for radiotherapy. The results of this study offer important insight into the potential use of MRI for abdominal planning and localization, as emerging MRI technologies, techniques, and onboard imaging devices are beginning to enable MRI-based radiotherapy [13-15]. In fact, MRI-only planning is currently the subject of much investigation [7], and may be implemented into clinical practice in the near future. Pretreatment MRI-based positioning verification will soon be a reality, with the first clinical installations of onboard MRI imaging devices (Section 3.2). Understanding how precisely anatomical borders can be localized is of great importance here, as uncertainties will have an impact on the inclusion of setup margins around the target and critical structures. Some of these devices are also designed to enable adaptive planning, during which anatomy will be segmented solely on an MRI imageset. The utility of daily onboard MRI for enhanced location and adaptive techniques is an exciting new prospect, and is the focus of the next section of this chapter.

3.2 Low-field MRI for Anatomy Visualization in Radiotherapy

3.2.1 Background & Significance

As previously discussed, MRI-based radiotherapy (RT) has recently become a prominent interest in radiation oncology due to its superior soft-tissue visualization [7, 65]. The additional benefit of image acquisition without the use of ionizing radiation makes MRI a particularly attractive modality for weekly or daily imaging throughout treatment. However, the use of standalone, offline MRI devices for routine imaging of the anatomical changes occurring over the course of treatment is not

optimal. First, many practices do not have convenient access to an MRI scanner directly in the clinic. The coordination of MRI scheduling, patient transfer and set-up, image acquisition, data transfer, and re-planning requires substantial time and resources, making it impractical to do on a daily (or even weekly) basis. In addition to cumbersome workflow issues, offline MRI cannot account for daily anatomical shifts and deformations due to daily patient positioning. These obstacles have motivated the development of onboard MRI for daily patient setup, anatomical localization and adaptive treatment.

Several groups have made substantial progress in the development of onboard MRI technology. Currently, several variants of onboard MRI-RT devices exist in various stages of development. Research teams in the Netherlands [66] and Canada [14] are each developing systems integrating linear accelerators with onboard MRI. Groups from Melbourne [67] and Cleveland [13] have proposed an alternative design, using a ^{60}Co treatment approach to simplify the technical considerations. A less integrated solution, where the MRI is de-coupled from the treatment system, has also been developed [5]. Many of these MRI-RT devices are designed to utilize low-field MRI (0.2-0.35T) to reduce perturbations of the dose distribution, machine interference, and distortion caused by the magnetic field.

The clinical advantage of onboard low-field MRI for daily anatomical position verification, however, has not been established. Although there are dosimetric benefits for MRI over X-Ray based imaging, no clinical studies have compared visualization of radiotherapy targets and critical structures between low-field MRI and standard onboard CT (OB-CT) imaging modalities commonly used in clinical practice. There are many studies comparing MRI simulation images to CT simulation images which have shown that MRI can more accurately represent soft tissue anatomy [7, 65], however this is not necessarily translatable to on-board imaging technology. Low-field MRI is characterized by a relatively low signal-to-noise ratio, and the implications of this technology for clinical target and normal structure visualization is unknown. A comparison of low-field on-board MRI to the clinical CT-based standard for image-guided RT is warranted to justify the clinical use of this technology.

We conducted a physician-based comparison for visualization of patient anatomy between onboard MR images acquired with a hybrid low-field MRI-RT system (see Appendix) and OB-CT images acquired as standard of care. We sought to evaluate the utility of onboard MRI for anatomic visualization of target and critical structures in the context of current clinical practice.

3.2.2 Materials & Methods

Low-field MRI. Imaging was performed on the ViewRay System (ViewRay Inc., Cleveland OH). The hybrid MRI-treatment unit is comprised of an open, split-solenoid low-field MRI co-registered to a three-head ^{60}Co gamma-ray radiation delivery device. The MRI has a nominal field strength of 0.35T and is a variant of the Siemens MAGNETOM product used for intraoperative imaging. The imaging and treatment isocenter are co-registered, allowing for simultaneous target treatment and localization (see Appendix). The low-field design of the MRI scanner allows for imaging with preservation of spatial integrity by limiting magnetic susceptibility artifacts. This design also prevents significant perturbations of the dose distribution. For this investigation, only the MRI component of the machine was used.

Patients. Fourteen patients undergoing fractionated radiotherapy for cancer in the thorax ($n = 2$), pelvis ($n = 6$), abdomen ($n = 3$) and head and neck ($n = 3$) were enrolled onto an IRB-approved protocol for MRI imaging with the ViewRay device (ViewRay Inc., Cleveland OH). The onboard MRI system was used to image each patient for one or two sessions prior to installation of source heads on the machine. All patients received additional standard of care image-guided treatment with routine daily/weekly onboard CT imaging on the TrilogyTM (Varian Medical Systems, Palo Alto, CA) or the Tomotherapy[®] (Accuray Inc., Sunnyvale, CA) treatment systems.

MR Imaging and Data. During each imaging session, patients were laid flat on the MRI table and fitted with a 12-channel torso or 11-channel head and neck receiver coil. Patients were positioned on the center of the table and their treatment position was reproduced as closely as possible, with feet secured together and arms placed on their chest or above their head. Patient-specific immobilization devices were not used due to size constraints and/or MRI-compatibility issues. Patients were

positioned with their treatment site longitudinally aligned with the imaging/treatment isocenter. Volumetric axial-plane MR images were acquired for each patient using a fast gradient echo sequence (TrueFISP or turbo FLASH) with parallel imaging techniques. Each imageset was acquired with an in-plane resolution of 1.5x1.5mm, slice thickness of 1.5mm (n = 10) or 3.0mm (n = 4), and field of view of 400-540mm x 228-449mm x 264-432mm in the lateral, anterior-posterior, and superior-inferior directions, respectively. Each volumetric scan lasted 1-3 minutes.

OB-CT data. Conebeam CT (CBCT) and mega-voltage (MVCT) image sets used for routine treatment localization were acquired on the Trilogy or Tomotherapy treatment systems within two weeks of MRI imaging for each patient. CBCT imagesets (n = 13) were acquired with an in-plane resolution of 0.7-1.2mm, slice thickness of 2-2.5mm, and a radial field of view of 250mm (n = 2), 450mm (n=9), or 465mm (n = 2). One patient was imaged with MVCT, acquired with an in-plane resolution of 1.5mm, slice thickness of 4mm, and radial field of view of 400mm.

Evaluation. For each of the 14 patients, the volumetric onboard MRI and OB-CT image sets were displayed side-by-side on clinical image viewing software and independently reviewed by three experienced radiation oncologists. Each physician was given a survey and instructed to indicate which image set (if either) offered better visualization of the target and individual organs at risks (OARs), as derived from a standardized list of site-specific critical structures [68]. For each image set pair, physicians recorded one of four responses for each structure: “Better visualized on MRI”, “Better visualized on OB-CT”, “Equivalent”, “Unable to see on either image set”. Physicians were permitted to freely scroll through axial images and adjust the zoom and window/level settings for optimal visualization. Fifteen to 24 OARs per patient were planned for evaluation, depending on the anatomical site (n = 24 for the thorax and head and neck, n = 15 for the abdomen, n = 20 for the pelvis (female), n = 21 for the pelvis [69]). Ten of 14 target structures were evaluable (i.e. intact tumors) and included in the evaluation.

Analysis. To assess the overall level of agreement among physician ratings, the proportion of structures resulting in majority (2/3 physicians) and unanimous consensus (3/3 physicians) agreement was computed. Additionally, agreement was measured by computing Fleiss' kappa, a

commonly used statistical metric of inter-rater reliability (9). The proportion of structures rated as better visualized on MRI or OB-CT was computed overall, and by anatomical site. To investigate if visualization was dependent on the type of structure, ratings were also analyzed after stratifying structures into five categories: soft tissue, central nervous system (CNS), vasculature, bone, pulmonary/airways, and target structure. One-way chi-square statistical testing ($\alpha=0.05$) was performed to test for significant differences between the proportion of structures better visualized on MRI and the proportion better visualized on OB-CT (overall, stratified by anatomical site, and stratified by structure type).

3.2.3 Results

Overall, 296 structure pairs were planned for evaluation on 14 MRI/OB-CT images set pairs. Seven of these structures were not evaluable due to previous surgical removal. Fifty-eight of the remaining 289 structures were not within the field of view of the OB-CT image sets ($n = 49$, 17%), MRI image sets ($n = 1$, <1%), or both image sets ($n=8$, 3%), and were omitted from the evaluation. Thus, 231 structure pairs were evaluated in total ($n_{\text{thorax}} = 46$, $n_{\text{pelvis}} = 70$, $n_{\text{abdomen}} = 48$, $n_{\text{head and neck}} = 67$) by each of the three physicians. Sample imageset pairs are shown in Figure 3.6.

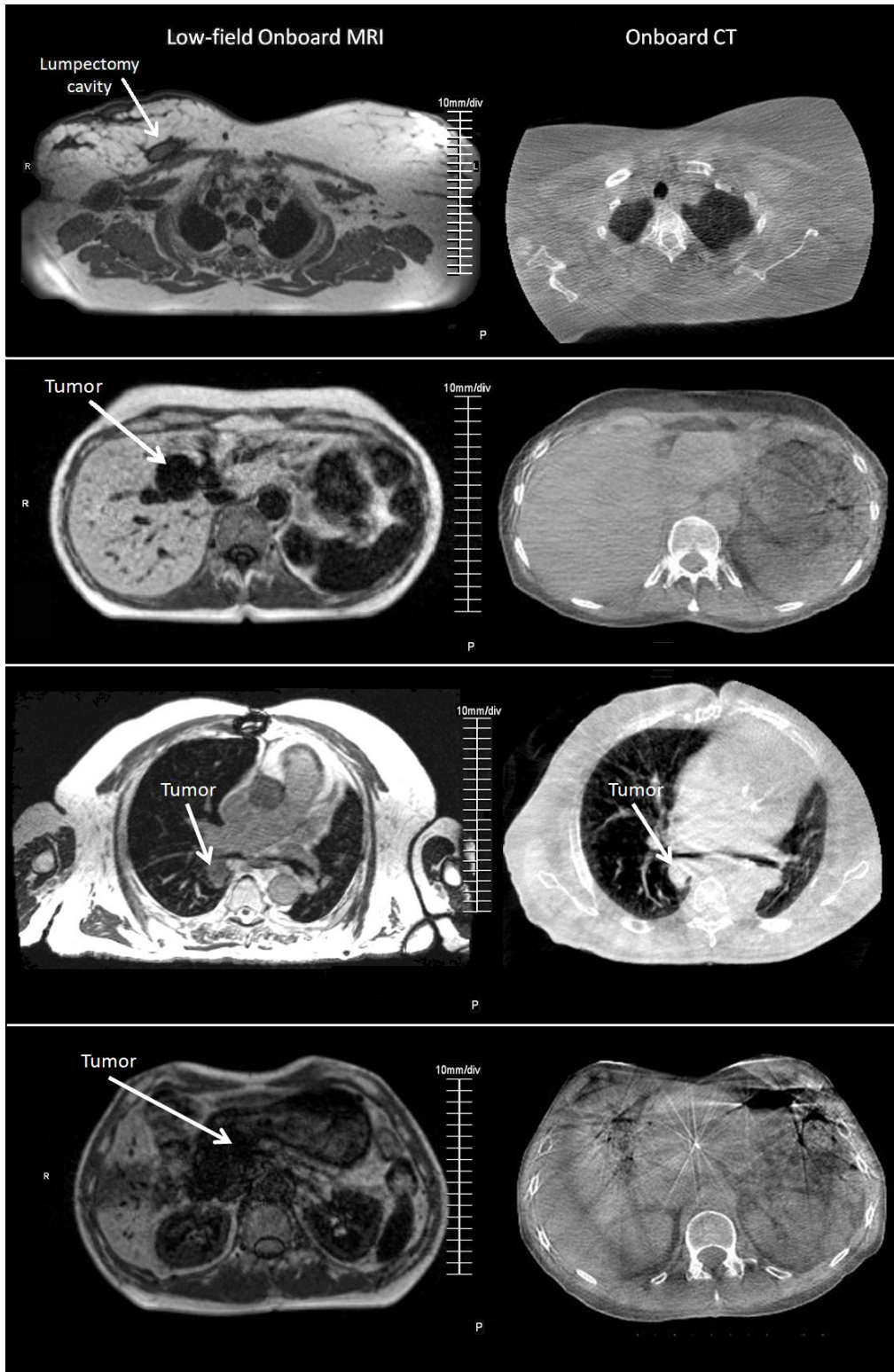


Figure 3.6. Examples of OB-MRI/OB-CT image set pairs for four targets: lumpectomy cavity, liver tumor, lung tumor, pancreas tumor (from top to bottom).

Agreement between the independent evaluations by physicians was high, indicating a high degree of inter-rater reliability. Physicians agreed in majority and in unanimous consensus for >99% and 74% of cases, respectively. In a single case, the three physician ratings were split between three categories, yielding no majority result. Fleiss' kappa was calculated as 0.63, indicating “substantial” agreement between physicians [70]. The following results are represented by majority agreement, unless otherwise stated.

Twenty-two (10%) structures were better visualized on OB-CT and 163 (71%) structures were better visualized on MRI, which was found to be a significant difference ($p < .001$). For thorax, pelvis, abdomen, and head and neck sites, the proportion of structures better visualized on MRI were 63, 63, 77, and 79%, respectively (Figure 3.7), and significantly greater than the proportion of structures better visualized on OB-CT by both majority and unanimous agreement ($p < .001$). Consensus was not reached for one thorax structure (the trachea), as reflected in Figure 3.7. Structures that were consistently better visualized on MRI 100% of the time are displayed in Table 3.3.

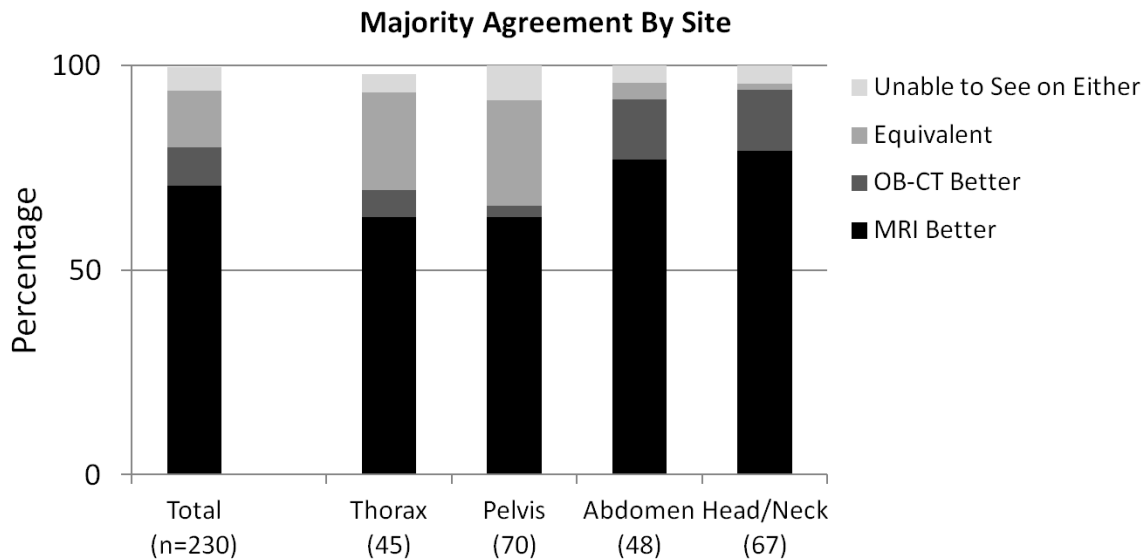


Figure 3.7 Ratings (majority agreement) stratified by anatomical site.

Table 3.3 List of evaluated OARs, by site. OARs which were better visualized on MRI or OB-CT for 100% of cases are indicated. OARs visualized equivalently on MRI and OB-CT (or better in some cases but not in others) are listed at the bottom of the table.

Site	Thorax	Pelvis	Abdomen	Head and Neck
Better visualized on MRI (majority)	A_Brachialceph	AnalCanal	Aorta	A_Carotid
	A_Pulmonary	Bladder	Colon	Cerebellum
	A_Subclavicular	Cervix	Duodenum	Chiasm
	Atrium	Colon	Kidney	CN_VII
	BrachialPlexus	PenileBulb	Liver	CN_VIII
	Carina	Penis	SmallBowel	Hippocampus
	Pericardium	Prostate	SpinalCord	OccipitalLobe
	SpinalCord	Rectum	Spleen	OpticNerve
	V_CavalInferior	SeminalVesicle	Stomach	ParietalLobe
	V_CavaSuperior	SmallBowel	Vessels	Parotid
	V_Pulmonary	Uterus		Pituitary
	V_SubClav	Vagina		SpinalCord
	Ventricle	Vessels		Submandibular
Better visualized on MRI (consensus)	Aorta	AnalSphincter	Esophagus	BaseOfTongue
	Esophagus	CaudaEquina	Pancreas	BrainStem
	V_Azygos			Retina
				Tongue
Better visualized on OB-CT (majority)	Rib		Rib	
Better visualized on OB-CT (consensus)				Ear_Middle
				VB_Cervical
Equivalent or Varied Ratings	A_Coronary	FemoralJoint	VB_Lumbar	Cochlea
	BronchialTree	Femur	VB_Thoracic	Glottis
	Lung	Ovary		LacrimalGland
	MainBronchus	PelvicBones		Larynx
	Trachea	Sacrum		Thyroid
	VB_Thoracic	Testis		
		Urethra		
		VB_Lumbar		
	AnalCanal			

Stratification of ratings based on structure-type categories revealed stronger trends (Figure 3.8). MRI provided better visualization for a vast majority of soft tissue (92%), vasculature (94%), and CNS structures (100%). OB-CT provided better visualization for two of 98 soft tissue structures (the larynx and the glottis, on one image set pair). The remaining 6% of structures in each of the soft tissue and vasculature categories were evaluated as “unable to see on either image set”.

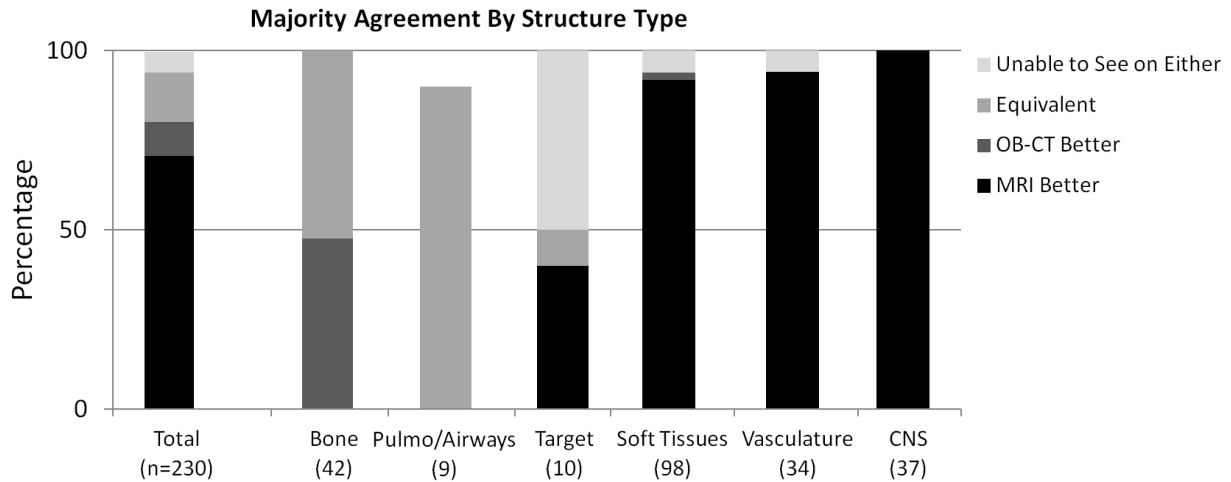


Figure 3.8 Ratings (majority agreement) stratified by structure type.

Bony anatomy was better visualized on OB-CT for 48% of structures, and equivalently visualized on both MRI and OB-CT for 52% of structures. All pulmonary structures were visualized equivalently on MRI and OB-CT datasets, although majority agreement was not reached for one pulmonary structure (the trachea), as reflected in Figure 3.8.

Target structures varied in location and size, and included three thoracic tumors, three pelvic tumors, two abdominal tumors, and two head and neck tumors. Four of ten target structures were better visualized on MRI, one was visualized equivalently on MRI and OB-CT, and five were not visualized on either. Targets were never better visualized on OB-CT, as compared to MRI. Physicians were in unanimous agreement for five of ten target evaluations (Table 3.4). Examples of MRI and OB-CT image sets are displayed for four targets in Figure 3.6.

Table 3.4 Majority and physician-specific ratings for the ten evaluated targets.

Target Evaluated	Physician 1	Physician 2	Physician 3	Majority Rating
Lumpectomy Cavity	MRI	MRI	MRI	MRI
Liver Tumor	MRI	MRI	MRI	MRI
Neck Tumor	MRI	MRI	MRI	MRI
Nasopharynx Tumor	MRI	MRI	MRI	MRI
Lung Tumor	MRI	Equivalent	Equivalent	Equivalent
Esophagus Tumor	Not Seen	Not Seen	MRI	Not Seen
Pancreas Tumor	Not Seen	Not Seen	MRI	Not Seen
Cervix Tumor	Not Seen	MRI	Not Seen	Not Seen
Anal Tumor	Not Seen	Not Seen	MRI	Not Seen
Anal Tumor	Not Seen	Not Seen	Not Seen	Not Seen

3.2.4 Discussion

The results of this study provide evidence that onboard low-field MRI offers better visualization for selected radiotherapy targets and most critical structures compared to OB-CT. Soft tissue, vasculature, and CNS structures were consistently better visualized on MRI, although high density bony anatomy was better visualized on OB-CT. Pulmonary structures such as the lungs and airways were comparably visualized for MRI and OB-CT. OB-CT never outperformed MRI for visualization of pulmonary structures, which is an interesting finding since CT is generally well-suited for imaging high-contrast interfaces. OB-CT also never outperformed MRI for visualization of target structures, which in this study were of soft tissue and pulmonary origin.

The degree of radiotherapy target visualization on MRI did vary. This is not surprising given the array of target sizes and locations included in the study. MRI proved particularly advantageous for visualizing solid tumors in the head and neck, liver, and lumpectomy cavity in the breast. There was some discordance among physicians on the usefulness of MR images for providing visualization of targets in the anus, cervix, esophagus, and pancreas. The anal and esophageal targets were smaller and less discreet compared to the other targets evaluated, possibly causing them to be less easily visualized by physicians. The pancreatic tumor (Figure 3.6) was not seen by 2/3 physicians, possibly due to a metal clip implanted at the target site which created an image artifact.

OB-CT may offer benefit when imaging high-density structures. While MRI provided equivalent visualization for a majority of bony anatomy, OB-CT was evaluated as superior for a considerable number of bony structures; specifically the ribs and some vertebral bodies. In one comparison case, OB-CT provided better visualization for two soft tissue structures – the larynx and the glottis – which are partially composed of cartilage. However, in the remaining two cases, the larynx and glottis were reported as better visualized on MRI.

Overall, onboard MRI enhanced anatomical visualization in comparison to onboard CT for most anatomy, including radiotherapy targets. Use of this technology could have significant implications for patient treatment. Better visualization can lead to better targeting, as demonstrated by the emergence of the first image-guided radiotherapy (IGRT) techniques years ago. The use of onboard X-Ray imaging to visualize internal anatomy has enabled more accurate patient setup, more conformal treatment techniques and smaller treatment margins [71, 72]. It has also been conducive to the use of dose escalation techniques, which has been shown to be beneficial for multiple disease sites [71-73]. Still, CT-based image guidance suffers from considerable geometric uncertainties and the need for additional post-processing for automated soft-tissue registration [73]. Manual registration is still necessary for soft-tissue sites due to suboptimal soft-tissue contrast, which can reduce the efficiency of patient setup. Enhanced visualization offered by MRI may lead to faster setup, and the possibility of automated registration based on soft tissue rather than bony anatomy.

MRI may be better suited than OB-CT for adaptive radiotherapy as well. MRI is known to improve the delineation of targets in the head and neck, central nervous system, and pelvis for radiotherapy treatment planning [7, 65], and may potentially replace CT in the future as the primary planning image set for some treatment sites. Efforts are currently underway to demonstrate the feasibility of MRI-only treatment planning. Jonsson *et al* performed a planning study for 40 patients with targets in the prostate, lung, head and neck and brain, and found that MRI-only treatment planning could be performed with a maximum dosimetric error of 1.6% [74]. Similar results have been reported by other studies investigating prostate radiotherapy planning [75-77], which has been the most frequently studied site for MRI-based planning and a likely target for its early clinical use. A publication by Kapanen *et al* describes the commissioning of a radiotherapy process for prostate treatment using MRI-only planning, which authors conclude is sufficiently accurate to replace CT-based planning and slated for use in their clinic [78].

While our findings support the use of MRI-guided radiotherapy, there are a few limitations of our study. First, study data is based on qualitative physician-based evaluations that are subjective in nature. However, we aimed to minimize any potential observer-specific bias by including three different radiation oncologists to perform independent reviews. Furthermore, results of Cohen's kappa indicate a substantial level of agreement between the three physicians, suggesting that results are generalizable across multiple observers. Results may not necessarily be generalizable across the general patient population, however, given our small patient sample of 14 patients. Our data may not adequately capture the full variation of anatomy and targets observed in other clinics. In particular, our ability to assess visualization of all types of tumors was limited since only ten patients had evaluable target structures. Still, the sample comprised a good variety of targets, varied in size, shape, location and composition. We were also able to evaluate a large variation of critical structures by selecting patients with different treatment sites. Utilizing a published structure taxonomy ensures that this evaluation can be widely interpreted in standard clinical context [68]. This study, however, did not quantify the impact of using onboard MRI for clinical tasks such as patient positioning or mid-treatment intervention. Future studies investigating the clinical impact of enhanced onboard MRI-based anatomical visualization will be necessary to fully demonstrate the value of onboard MRI for clinical practice.

Our results suggest that low-field MR provides better anatomic visualization of many radiotherapy targets and many organs at risk as compared to CBCT/MVCT, which is currently the clinical standard for volumetric localization. This finding was consistent across all major anatomical sites (thorax, pelvis, abdomen, and head and neck), and supports implementation of this technology for visualization of radiotherapy targets and critical structures in the clinic.

Chapter 4

Onboard Cine MRI for Tracking Bowel

Intra-fraction tissue motion is a crucial problem for many treatment sites. However it is most problematic for abdominal sites, which can experience motion on the order of several centimeters during treatment [18]. Intra-fraction motion introduces substantial challenges in delivering the dose to the target as intended. In particular, bowel is one of the most critical dose-limiting structures in the abdomen due to its low radiation tolerance and poor localization during treatment [19]. Newly emerging technologies incorporating real-time MRI during radiotherapy may enable visualization and dosimetric avoidance of the bowel during treatment. A potentially significant advancement is the use of intra-fraction positional information to suspend delivery of the treatment beam while the bowel is in its path, a technique known as beam ‘gating’. However, gating treatment based on the bowel position has never been investigated. Tracking bowel is exceptionally challenging due to unpredictable shape changes, non-systematic peristaltic motion, and random fluctuations in bowel contrast. Here, we have developed automated deformable bowel-tracking software using a combination of normalized cross-correlation tracking and an active contour method in order to investigate the potential application of real-time MR-based bowel tracking and ‘bowel-gated’ treatment.

4.1 Background & Significance

The use of radiotherapy is a common treatment alternative for unresectable abdominal cancers, and is also often used in conjunction with surgical resection [49, 51]. Moreover, emerging magnetic resonance image (MRI) guided interventions, such as MR-guided focused ultrasound, are also being investigated for treatment of abdominal cancers [79]. Radiotherapy studies have shown promising results in local control of abdominal cancers when treated with high radiation doses [80, 81], however potential complications arising from normal tissue toxicity limits dose escalation techniques [19].

Bowel is regarded as one of the most critical dose-limiting structures in the abdomen due to its low radiation tolerance and poor localization during treatment [19]. The bowel experiences drastic deformations between daily treatment sessions and large-scale respiratory motion during radiation delivery. When this motion is not controlled for, bowel segments in close proximity to the target area may enter regions of high dose during treatment. Repeated exposure of high doses to the bowel can cause ulcerations, bleeding, frequency, fistula formation, and obstruction [82]. While onboard X-Ray imaging systems are commonly used for many anatomical sites to localize the target and critical structures for treatment, the soft tissue of the abdomen is poorly visualized using these techniques. Currently, there is no way to directly monitor or intervene on motion of the bowel during delivery.

Our group has performed the first clinical imaging trial with the hybrid MRI-radiotherapy device, ViewRay (Cleveland OH). This new technology incorporates real-time MRI during radiotherapy, enabling bowel visualization during treatment. This could potentially aide in a delivery intervention scheme where the radiation beam is temporarily and automatically disabled when the bowel enters high dose regions. This type of ‘gating’ scheme typically utilizes an external surrogate for target localization. Until now, the feasibility of real-time tracking of the bowel for gated radiotherapy has never been explored, nor even presented as a possibility in clinical practice. The development of real-time MRI has made this application a real possibility.

However, tracking the bowel during radiotherapy presents considerable challenges. Unlike tracking targets in the thorax, which is a popular topic of research in the literature [4, 83], bowel tracking must accommodate random motion patterns, unpredictable shape changes, and large fluctuations in contrast. Research has been done on the study of peristaltic bowel motion on cine-MRI for diagnosis and assessment of gastro-intestinal diseases [84, 85]. These studies attest to the challenges of tracking the shape and borders of imaged bowel. The bowel's flaccidity gives rise to continuous deformations, causing both in-plane and out-of-plane geometric changes. Whole segments of bowel may disappear and reappear in 2D cine images. Furthermore, peristaltic motion of the bowel is usually not systematic or predictable. Therefore predictive modeling, which has been used extensively for targets in the thorax [86, 87], is not as easily applied for bowel-tracking. Changes in position and shape are often coupled to fluctuations in bowel contrast, since both physiologic changes are driven by bowel filling and emptying. Because bowel contents vary from air, to liquids, to solids, these contrast changes are often extreme. This can cause complications for tracking techniques that rely upon image intensities and gradients to define regions and borders of interest [85].

To date, algorithms investigated for bowel tracking have been designed for retrospective post-processing in order to assess bowel motility. Wu *et al* reported on the use of a fast-marching method to retrospectively track bowel borders undergoing peristaltic motion [85]. In their publication, authors describe the implementation of an anisotropic Gaussian filter and a boundary penalty to improve tracking of low-contrast regions, as the traditional fast-marching method is reliant on image gradients. Authors gauged the success of this algorithm by comparing diameter measurements of the tracked bowel to manual measurements of the bowel. While they reported approximately 94% accuracy, only 240 cine image frames were tested, and details of the MRI image sets and evaluation were limited in their published report [85]. Yigitsoy *et al* demonstrate the use of their manifold learning algorithm for tracking out-of-plane bowel motion on approximately 2,700 image frames; however authors describe a multi-planar method for tracking respiratory-induced motion only, and do not explicitly report any tracking accuracy results [88].

We aimed to develop tracking software for real-time tracking of deforming bowel on low-field cine imagesets, and demonstrate its utility on a dataset of more than 11,000 image frames. To our knowledge, no such applications have been developed or tested on such an extensive data set. The tracking algorithm described herein combines a template matching approach with an active contour method. A template matching approach was selected due to its demonstrated robustness in tracking moving anatomy on 2D cine MRI [89]. The selection of an active contour method to track bowel deformations was made for several reasons. First, due to its intrinsic connectivity, the information of an active contour is integrated along the length of the contour, which is particularly advantageous for analyzing noisy images or natural scenes [90]. Thus, this method can be expected to be well-suited for images demonstrating a lower signal-to-noise ratio, as is seen in low-field MRI. The active contour method is also robust to tracing boundaries of objects with edge gaps (caused by low contrast, image artifacts, or noise corruption), while other edge detection algorithms generally fail in this scenario. This makes it advantageous for detecting subjective contours which may not have fully explicit edges [91]. The active contour model offers the ability to tune parameters to control inherent properties of the contour (such as contour flex and elasticity) and to weight internal and external forces acting on the contour. These forces act to complement each other in order to optimize the position of the contour. This behavior is extremely useful for tracking continuous deformations and motion of non-rigid, natural shapes [90]. Due to its versatility, the active contour model has been used for contour tracking, stereo matching, shape skeletonization, scale-space tracking, and automated path planning. This method has also been used extensively for segmentation of static medical images, such as auto-segmentation of brain tumors [92].

Software was developed and evaluated on 70 cine MR patient imagesets acquired with the ViewRay hybrid MR-radiotherapy unit. 11,556 cine image frames acquired at a frame rate of 2 or 4 Hz were analyzed. We demonstrate its use for tracking bowel segments with varied shapes, sizes, contrast levels, motion patterns, and image intensities. The demonstrated application of this software offers promising implications for the treatment of pelvic and abdominal targets where bowel toxicity is a concern, and could be extended to other MRI-guided interventions.

4.2 Materials & Methods

4.2.1 Imaging Equipment

All imaging was performed on the ViewRay hybrid MR-radiotherapy unit, which is detailed in section 3.2.2 and the Appendix.

4.2.2 Image Acquisition & Data

Two-dimensional cine MR imagesets were collected from seven patients enrolled on an IRB-approved protocol. All patients were diagnosed with cancer in the abdominal or pelvic region, and scheduled to receive radiotherapy. Cine imagesets were acquired over a duration of 0.5 to 2.5 minutes at a frame rate of 2 or 4 Hz. In total, 11,556 image frames of patient bowel were analyzed. All imagesets were acquired in the coronal or sagittal plane in order to capture a maximum degree of motion. Images were acquired at slice thicknesses of 3.5, 5, and 7mm, and an in-plane resolution of 3.5x3.5mm. Images were interpolated to an in-plane resolution of 1.75x1.75mm for image analysis and tracking. All cine image sets were acquired with a TrueFISP sequence (see Appendix) and a flip angle of 60°. Repetition and echo times for imaging sequences ranged from 2.4 – 3.6ms and 1.0 – 1.6ms, respectively.

4.2.3 Tracking Software

Tracking software was developed to track motion of targeted bowel segments throughout the duration of the cine sets. The software implements a combination of a weight-normalized cross-correlation technique to track gross displacement, and an active contouring method to track deformation. The software was preliminarily developed to work offline, in order to test its accuracy. The software workflow is first described before detailing of the components of the tracking algorithm itself.

Workflow. Cine MR imagesets are imported into MATLAB (v2011b) as generic DICOM files, and the first frame is displayed for the user. The user manually segments the targeted region of the bowel

on the first frame of the 2D cine imageset. The tracking algorithm is then applied to identify the position of the bowel on subsequent images. The basic tracking workflow is depicted in Figure 4.1, and is as follows. 1) The image frame I_n is loaded and 2) a template matching algorithm is used to identify the gross shift of the contoured bowel from the origin. 3) The algorithm employs an active contour method to deform the contour to the borders of the bowel. The process is then repeated for the next tracking iteration.

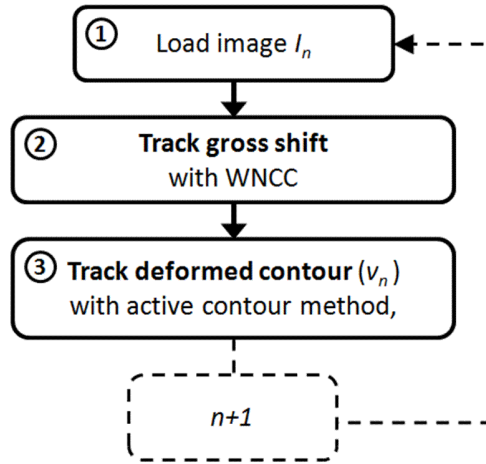


Figure 4.1 Workflow of bowel tracking software.

Tracking gross motion. The gross motion tracking component of the software is based on a variant of the classical normalized cross-correlation (NCC) algorithm to measure similarity between a matching template and the image of interest. The image region encompassed by the previously tracked contour (V_{new}) from image frame I_{n-1} provides a template region for matching the segmented bowel on the subsequent image I_n . The classical NCC technique may compromise tracking accuracy since the template matching region is rectangular, and includes non-significant features that move in discordance with the bowel. By applying a weight to each pixel element in the template indicating value of matching priority, a weighted normalized cross-correlation (WNCC) can be achieved. At point (p,q) within an image or image sub-region (I) , the WNCC coefficient (γ) between the image I and template T is computed using the weighting matrix W according to equation 4.1. Here, μ_I and μ_T are defined as the average image intensities (over the area of the template) of the image I and the template T , respectively.

$$\gamma(I, T, W) = \frac{\sum_{x,y \in T} (I_{(p+x,q+y)} - \mu_I)(W_{(x,y)})(T_{(x,y)} - \mu_T)}{\sqrt{\sum_{x,y \in T} (I_{(p+x,q+y)} - \mu_I)^2 (W_{(x,y)})^2 (T_{(x,y)} - \mu_T)^2}} \quad (4.1)$$

The weighting matrix W is established using information from the image frame I . The values in the weighting matrix are determined for points all points (x,y) on template T :

1. spatially, by defining positive values for points (x,y) on within the bowel contour region (R) , and
2. statistically, by computing the discrete probability density function (*pdf*) of image intensities on R , and weighting corresponding points (x,y) by their probabilities.

Pixels located within the contour region R are considered high priority, and thus are positively weighted. Those values outside the contour are assigned a value of zero (Equation 4.2).

$$W_{(x,y)} = \begin{cases} pdf(x,y), & \text{for } (x,y) \in R \\ 0, & \text{otherwise} \end{cases} \quad (4.2)$$

During the tracking process, the location of maximum correlation between the template and image is used to compute the gross translational bowel displacement for the n^{th} frame (*shift_n(x,y)*). This position is indicated by the location of γ_{max} , the maximum WNCC coefficient. A search window constraint limiting the distance of γ_{max} from the previous location (on frame $n-1$) is applied to improve speed and accuracy. Thus, γ_{max} for the n^{th} frame is identified within a window of size of $s_w \times s_l$ on γ , centered at $(x_{\gamma_{max}}, y_{\gamma_{max}})_{n-1}$. The window size $s_w \times s_l$ is user-defined, and was defined in our process as 15x15mm for a sampling rate of 4Hz and 30x30mm for a sampling rate of 2Hz. This value was determined by calculating the maximum motion the bowel was likely to move at an average breathing rate of 15 breaths per minute. In clinical practice, this constraint could be defined by monitoring the patient's breathing frequency and amplitude immediately before initiation of daily treatment.

The coefficient γ_{max} ranges between 0 and 1, with 1 indicating perfect correlation between I_n and template T . During initial software testing, low values of γ_{max} often corresponded with a state in which the tracking failed and the resultant contour had deviated away from an accurate location. To

control for this situation, a subroutine within the tracking code was designed to flag instances in which γ_{max} fell below a threshold of 0.7, a value which indicates “good” agreement [93]. Under this condition, the gross shift was defined as an average of $shift_n$ and $shift_{n-1}$. (Figure 4.2) The implementation of this condition greatly improved the recovery rate of failed tracking instances.

After determining the bowel displacement, the contour output from the previously tracked image frame (v_{new}) is shifted in x and y directions by the determined gross shift (Figure 4.2). This new shifted contour is defined as v_0 , and is passed to the deformable tracking component of the software as an initial guess of the location of the bowel borders.

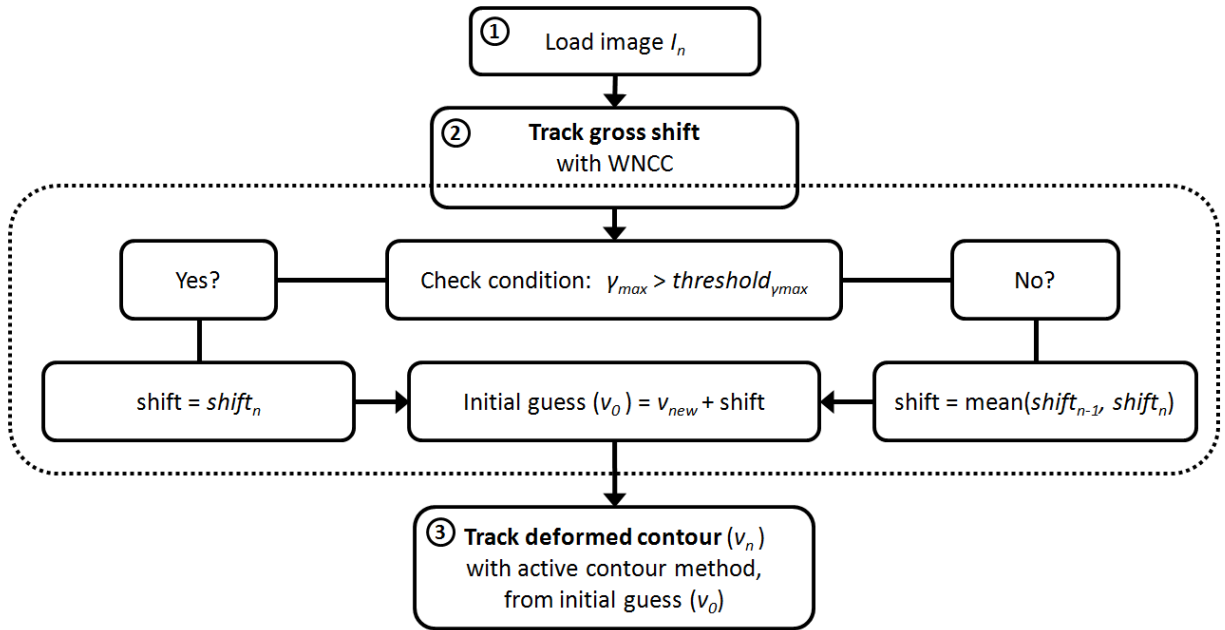


Figure 4.2 Workflow for determining the shift of the bowel contour from frame $n-1$ to frame n based on the γ_{max} constraint.

Tracking deformable motion. The deformable motion tracking component of the software is based on a modified version of the traditional active contour method, originally described by Kass *et al* [91]. Traditional active contour models, also known as “snakes”, are based on the premise of minimizing the energy of the contour (E_{snake}), which is comprised of energies contributed by internal (E_{int}) forces and image (E_{ext}) forces (Equation 4.3). A preliminary guess of the position of

the boundary of interest (v_0) is first given. The position of the contour is then iteratively optimized to a state of minimum local energy.

$$E_{snake}^* = \int_0^1 E_{int}(v(s)) + E_{ext}(v(s)) ds \quad (4.3)$$

where

$$v(s) = (x(s), y(s)) \quad \text{describes the position of the snake} \\ \text{parametric form.}$$

The internal energy E_{int} represents the energy contributed by contour itself modeled as a spline, and controls contour smoothness. The internal energy was implemented as described by Kass *et al* (see Appendix), in order to force smooth behavior of the contour. The external energy E_{ext} includes the energy contributed by image forces, including image intensity and image gradients. It is represented by the weighted sum of image force components, as:

$$E_{ext} = w_{line}E_{line} + w_{edge}E_{edge} + w_{term}E_{term} \quad (4.3)$$

where w_{line} , w_{edge} , and w_{term} control the weights of the line energy (E_{line}), edge energy (E_{edge}), and terminal energy (E_{term}), respectively (see Appendix).

In our implementation, two major modifications were made to the traditional definition of E_{ext} . The first modification was made to the E_{line} energy, which is traditionally represented as the image intensity (ie. the image I itself) in order to attract the contour towards high or low intensities characterizing light or dark lines, respectively. Low (dark) intensities translate to low energy, which attracts the contour. Weighting E_{line} with a value $w_{line} < 0$ negates this relationship, so that high intensities represent low energies, attracting the contour. On the cine MR imagesets analyzed here, areas of high and low intensities typically represent regions of the targeted bowel and the underlying background tissue, not structure borders. Furthermore, the internal region of the bowel can

represented by various intensities (from high to low) depending on the image set, particular bowel segment, and moment of time when the bowel is imaged (since the bowel is susceptible to mid-imaging contrast changes). In order to address this issue, the E_{line} term was replaced with a term E_{region} , defined as the following:

Let R_{int} represent the region on image I_n (scaled to [0,1]) encompassed by the initial guess contour v_0 on the n^{th} image frame. Let R_{ext} represent the complement of R_{int} (ie. the region outside of the R_{int} , including its boundary). Let pdf_{int} represent the discrete probability density function of pixel intensities [0,1] located within R_{int} . Then,

$$E_{region}(x, y) = \begin{cases} pdf_{int}(x, y), & \text{for } (x, y) \in R_{int} \\ 1 - pdf_{int}(x, y), & \text{for } (x, y) \in R_{ext} \end{cases} \quad (4.4)$$

Thus, E_{region} represents the image $I_n(x, y)$ as a matrix of probabilities, weighted by the pdf of pixels lying within the contour v_0 (i.e., on R_{int}). Pixels lying on R_{int} having intensities that occur frequently within R_{int} are labeled with a high energy value, while pixels having intensities that occur less frequently are labeled with a low value. Conversely, pixels lying on R_{ext} having intensities that occur frequently within R_{int} are labeled with a low energy value.

Given a reasonable initial guess contour v_0 , the contour will move to encompass regions that are characteristic of the inner contents of the bowel, based on pixel intensity. On R_{ext} , the contour is attracted towards regions that contain high frequency intensities of the inner contents of the bowel (which commonly represents bowel which has fallen outside the contour), while on R_{int} , the contour is attracted towards regions that do not contain high frequency intensities of the inner contents of the bowel (commonly representing background tissues which have fallen inside the contour). For example, consider a segment of deformable bowel whose inner contents appear dark (low intensity) on a set of cine MR images. An expansion of the deforming bowel from frame $n-1$ to frame n will leave part of the bowel un-encompassed by contour v_0 (Figure 4.3). Regions of outlying bowel, labeled with low E_{region} values, will attract the contour outward.

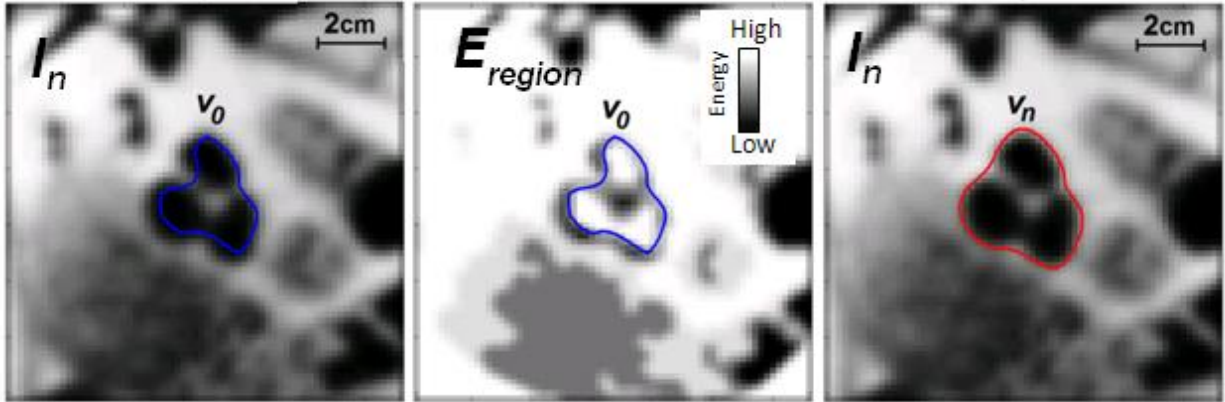


Figure 4.3 Example of E_{region} in aiding contour expansion. Initial contour v_0 overlaid on image I_n (Left). Initial contour v_0 overlaid on E_{region} (Middle). Deformed contour v_n overlaid on image I_n (Right).

Conversely, a contraction of the deforming bowel from frame $n-1$ to frame n will result the inclusion of outlying tissues by contour v_0 (Figure 4.4). Regions of encompassed tissue, labeled with low E_{region} values, will attract the contour inward.

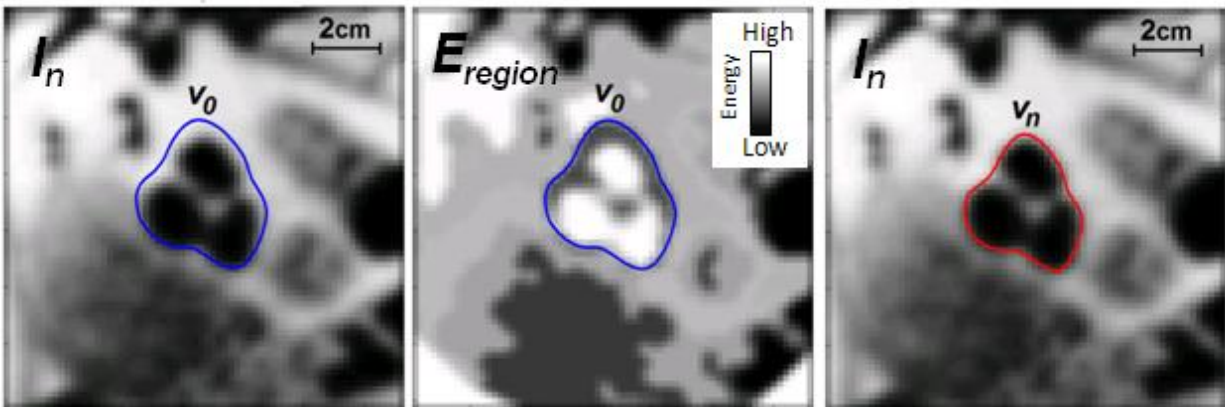


Figure 4.4 Example of E_{region} in aiding contour contraction. Initial contour v_0 overlaid on image I_n (Left). Initial contour v_0 overlaid on E_{region} (Middle). Deformed contour v_n overlaid on image I_n (Right).

Because E_{region} is computed based on the *pdf* of the inner contents of the bowel, it is robust to a spectrum of intensities, low to high. While E_{region} will operate ideally in a fairly homogenous region of bowel, non-homogenous regions can be challenging. For example, high intensity materials may momentarily fill regions of the bowel as they pass through, causing inner contents to take on the appearance of outlying tissue. Thus, E_{region} may act to push the contour away from the true

boundaries of the bowel in order to accommodate such non-homogenous regions. Figure 4.5 demonstrates this issue. To control for such situations, a feature is implemented within the tracking code to dynamically weight E_{region} based on the distribution of pdf_{int} . When the inner quartile range of pdf_{int} exceeds a certain threshold indicated a large range of pixel intensities within the contour, w_{region} is decreased, reducing the contribution of E_{region} to E_{ext} .

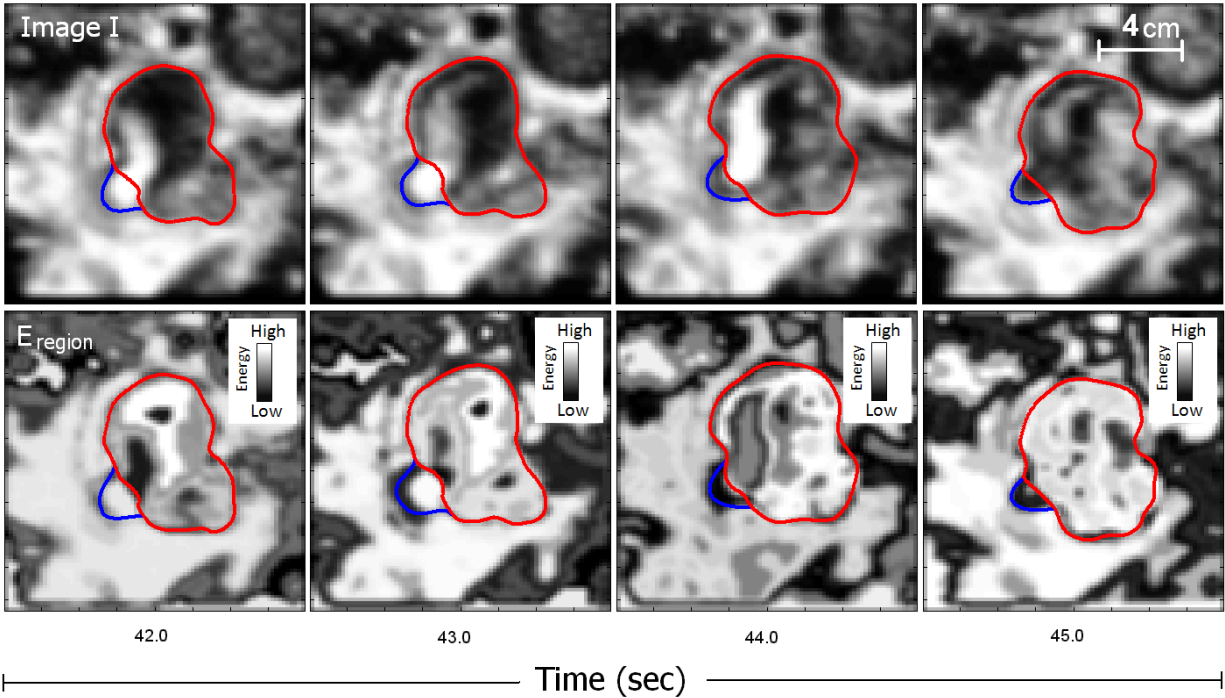


Figure 4.5 Example of changing bowel contrast and its effect on E_{region} . The red contour is the output contour, and the blue contour represents the true position of the tracked bowel.

A second modification was introduced to the active contour implementation in order to localize the contour to the most probable local energy minima. This was implemented using positional information from the prior v_{n-i} contours (where $i = 1, 2, 3 \dots i_{user-defined\ limit}$). In our implementation, the previous five contours were used. The Euclidean distance from the contour v_{n-i} is computed during iteration $n-i$, and the distance map is stored as a two-dimensional matrix. Pixels lying on the contour are assigned a value of zero energy, with energy values increasing for pixels located increasingly more distant from the contour. During the n^{th} iteration, the stored distance maps are translated to the new bowel position computed by the WNCC process, and summed over (x, y) .

This resultant matrix, representing energy as a function of distance from prior contours, is as added to E_{ext} as $w_{dist}E_{dist}$, where w_{dist} is a weighting factor. Thus, the final representation of the external energy is:

$$E_{ext} = w_{region}E_{region} + w_{edge}E_{edge} + w_{term}E_{term} + w_{dist}E_{dist} \quad (4.5)$$

While these modifications greatly improve tracking accuracy, they do not fully eliminate errors. In some instances, energy minimization is achieved at a set of points on the deformed contour boundary that does not accurately represent the deformed bowel. Most commonly, the V_n contour will either collapse in or expand out to an inaccurate position due to local minima or nearby gradients which represent false bowel edges. Since V_{new} is used in the subsequent $n+1$ iteration to establish V_0 , contours which inaccurately shrink or expand often lead to composite effects, rendering a contour which collapses down to a point or expands out to the image edge over subsequent image frames. Not surprisingly, this is most common in images where the bowel is inhomogenous or there are nearby structures with similar intensity or gradient features. In order to control for these types of tracking failures, a constraint was placed on the size of the contour itself, limiting it to physiologically realistic dimensions. A constraint placed on the perimeter of the tracked bowel was deemed most appropriate, since the bowel can easily change shape within a matter of seconds while the perimeter remains the same. Thus, a subroutine within the tracking code is implemented to flag instances in which the percentage change of the perimeter of V_n (compared to V_I) falls below a user-defined threshold, indicating an unsatisfactory result. For our implementation, a value of 15% (which was established during testing) is used. Under the condition that the contour perimeter changes more than 15%, V_{new} is defined as V_0 at the end of the n^{th} iteration. Otherwise, V_{new} is defined as V_n (Figure 4.6). The template is then updated as the region on image I_n encompassed by V_{new} .

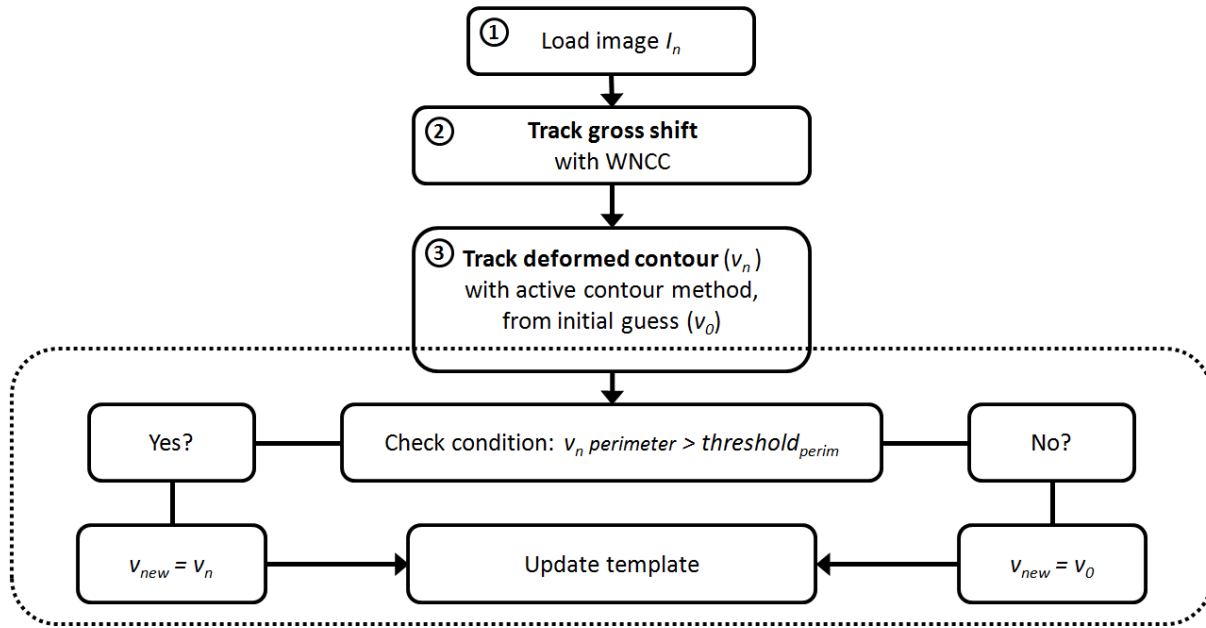


Figure 4.6 Workflow for determining the output contour, v_{new} for the subsequent tracking iteration, based on the v_n perimeter constraint.

Evaluation. Seventy cine MR imagesets (11,556 image frames in total) of small and large bowel located in the upper, mid-, and lower abdominal region of seven patients were analyzed. Cine image sets were acquired for an average duration of 47 seconds, with a minimum of 30 seconds and a maximum of 2.5 minutes. The tracking software was used to track bowel segments on each cine imageset, and the centroid of each tracked contour was stored. Due to the lack of an objective ‘gold standard’ baseline for tracked images, each frame was manually inspected and the agreement between the deformed bowel contour and the appearance of the bowel on the image was assessed. Any disagreements were flagged by the observer on a frame-by-frame basis. Disagreements were considered to be cases in which 1) portions of healthy tissues were encompassed by the deformed contour, and 2) portions of bowel which were designated for tracking were not encompassed by the tracked contour.

Additionally, the nature of tracking inaccuracies was categorized as the following for image each frame (in increasing severity):

Type 1) minor disagreement of the contour with true bowel edges, $< 5\text{mm}$

Type 2) major disagreement of the contour with true bowel edges, $> 5\text{mm}$

Type 3) complete tracking failure, with a majority of the contour containing outlying tissues, or a majority of bowel exceeding the contour.

Type 2 and Type 3 tracking inaccuracies were designated as tracking failures. The percentage of image frames demonstrating tracking failures (Type 2 and Type 3 inaccuracies) was computed for each of the 70 image sets. Examples of each type of inaccuracy can be seen in Figure 4.7.

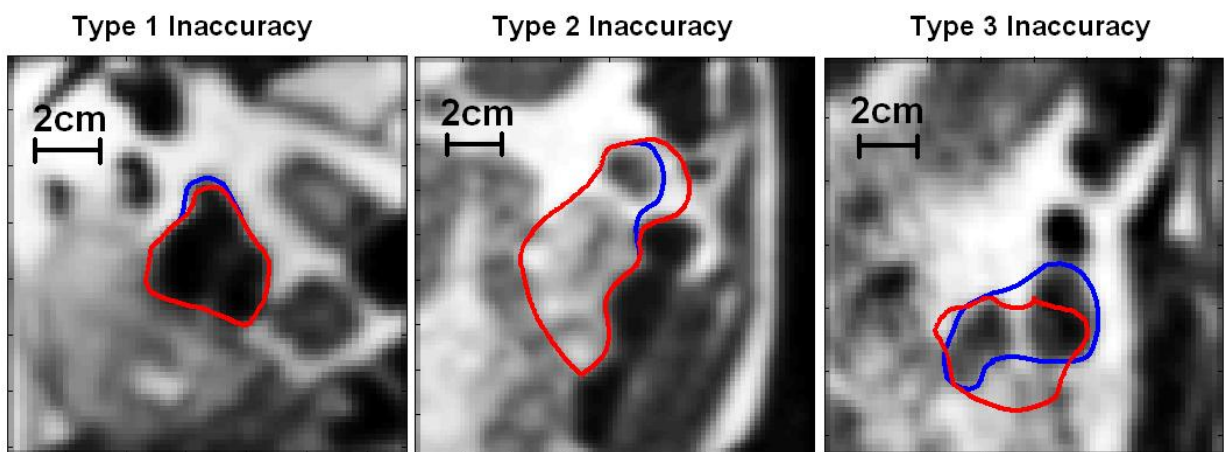


Figure 4.7 Examples of Type 1, 2 and 3 tracking inaccurate. The red contour is the output contour, and the blue contour represents the true position of the tracked bowel.

4.3 Results

Overall, the algorithm demonstrated moderate success in tracking the bowel over large amplitudes, and under conditions of deformation and contrast changes. Figure 4.8 displays three subsequent cine image frames and the tracked bowel abutting a liver tumor. There was a substantial variation in size, shape, and intensity of tracked bowel segments. Table 4.1 displays statistics characterizing the large variation in geometric and intensity-based features over all 70 cases. Figure 4.9 displays several examples of bowel segments tracked by the tracking algorithm.

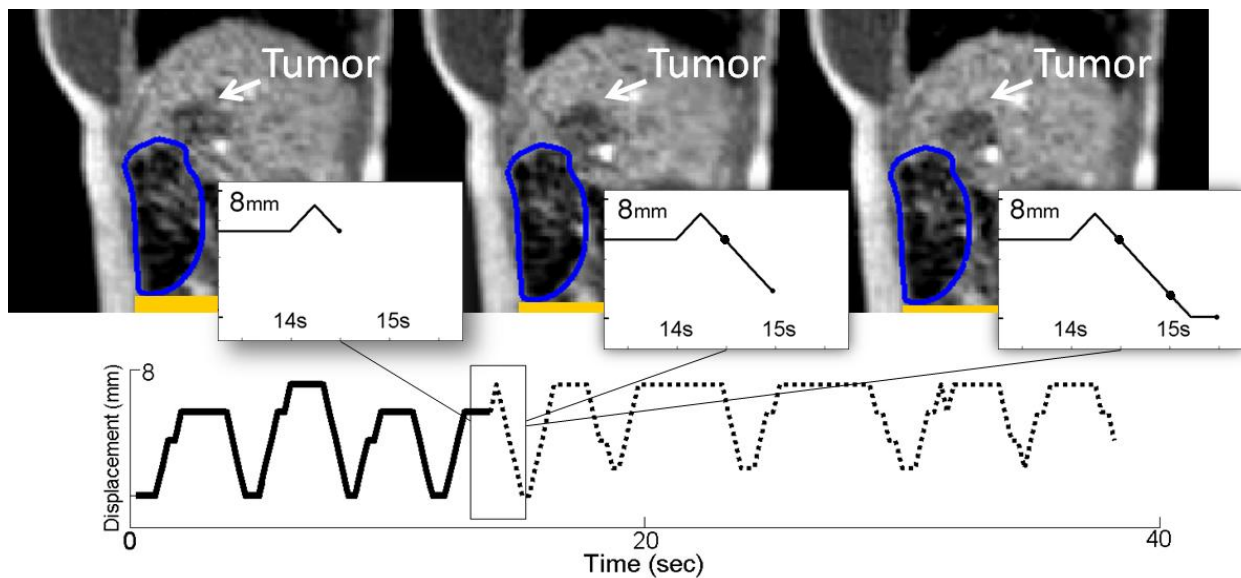


Figure 4.8 A sequence of frames showing tracked bowel (blue contour) abutting a liver tumor. The yellow bar indicates motion of the inferior edge of the bowel. The box overlaid on the SI motion trace defines the motion range displayed in the insets. Each inset displays the tracked motion at that instance.

Table 4.1 Features of tracked bowel segments as they appear on frame 1. Width and height are computed from a rectangular bounding box enclosing the contour.

Feature	Std Dev	Mean (Min – Max)
Area (cm ²)	16.6	20.3 (3.0 – 87.5)
Width (cm)	2.5	5.1 (1.5 – 13.5)
Height (cm)	3.1	6.1 (1.8 – 14.6)
Eccentricity (0 - 1)	0.2	0.8 (0.3 – 1.0)
Mean intensity of pixels within the contour* (0 – 1)	0.2	0.4 (0.1 – 0.8)
Variance of pixel intensities within the contour*	0.1	0.3 (0.0 – 0.4)
Mean absolute gradient across contour boundary* (0 – 1)	0.05	0.31 (0.4 – 0.10)

*Intensity-based features are normalized to pixel intensity values contained within a 4cm margin around the contour.

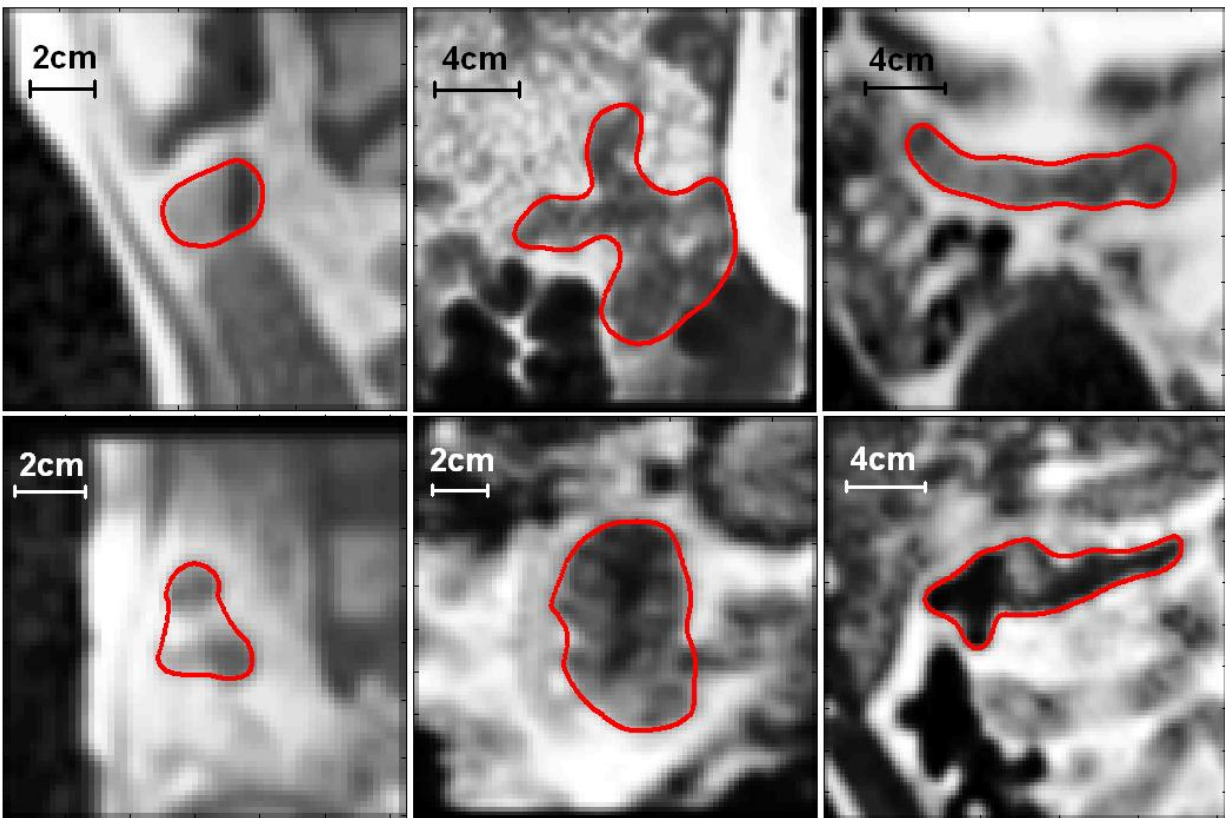


Figure 4.9 Examples of tracked bowel segments.

The tracked bowel motion yielded an average amplitude of 7 mm in the superior-inferior (SI) direction, and 3 mm in the anterior-posterior (AP) and lateral directions over the sample of patients (Table 4.2). Frames which were found to yield Type 2 and Type 3 tracking inaccuracies were not included in the calculation of these statistics.

Table 4.2 Mean, maximum, minimum, and average standard deviation of tracked motion amplitude for the SI, AP and lateral (Lat) directions for all patients.

Direction	Tracked Motion Amplitude (mm)			
	Mean	Maximum	Minimum	Average Std Dev
SI	7.0	22.9	1.7	3.1
AP	3.5	14.1	0.3	1.4
Lat	3.2	15.8	0.0	2.4

Eighty percent of cases ($n = 56/70$) were tracked with 80% accuracy or greater. A histogram of the tracking accuracy of the 70 cine MR imagesets is displayed in Figure 4.10. A majority of inaccuracies were categorized as Type 1 disagreements, in which the contour showed a minor disagreement ($<5\text{mm}$) with the true boundary of the bowel (Table 4.3). The mean duration of Type 1 errors was 7.8 seconds. Sixty-three percent of cases displayed Type 2 inaccuracies; however in a majority of these cases ($n = 24/44$ or 55%), Type 2 inaccuracies were observed for 5 seconds or less. Two cases demonstrated Type 3 inaccuracies, resulting in a complete tracking failure (Type 3). Examples of these failures can be seen in Figure 4.7.

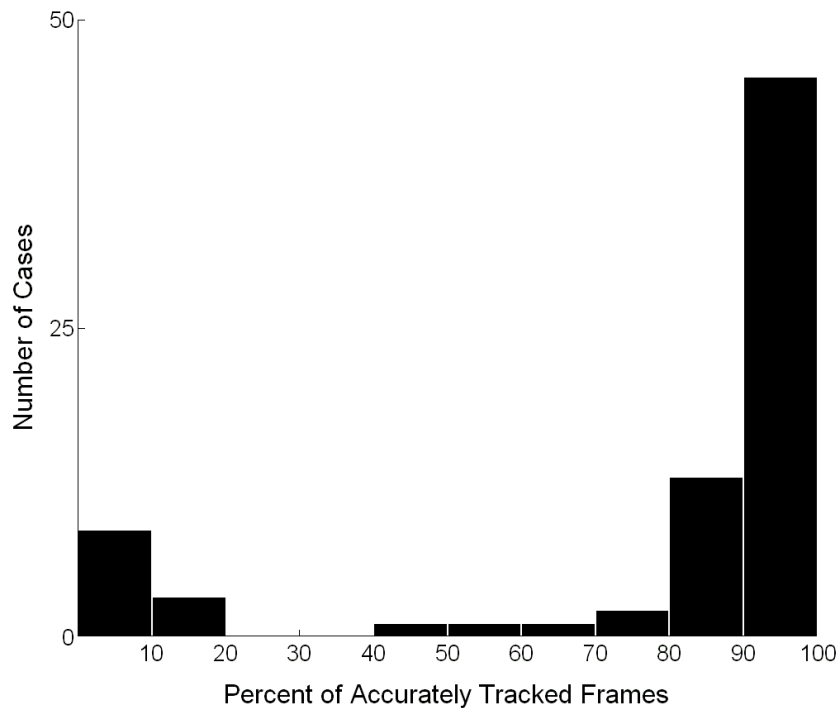


Figure 4.10 Histogram showing percentage of frames in which the bowel was accurately tracked.

Table 4.3 Number of cases resulting in tracking inaccuracies (by type)

Type of Tracking Inaccuracy	Number of Cases (Percent of Cases)
Type 1 (Minor)	51 (73%)
Type 2 (Major)	44 (63%)
Type 3 (Complete Failure)	2 (3%)

Not surprisingly, the tracking algorithm worked well for high-contrast, fairly homogenous regions of bowel. The algorithm also demonstrated some robustness to intermittent changes in contrast. Tracking failures seemed mostly attributed to deformation tracking (rather than gross motion tracking) as tracked contours appeared centered on the bowel for most cases, even when there were disagreements between the contour and the true boundaries of the bowel. This suggests that the WNCC approach is satisfactory, even for rapidly changing bowel segments. While the modified active contour method was moderately successful, it was still somewhat susceptible to inaccuracies

in differentiating bowel boundaries from other nearby boundaries. An example of this can be seen in Figure 4.7 (center), where the contour deviated away from the true boundary of the bowel due to the presence of another proximal boundary in the image. Sometimes tracked contours also experienced some lag when deforming to portions of bowel moving into the two-dimensional imaging plane. An example of this can be seen in Figure 4.11.

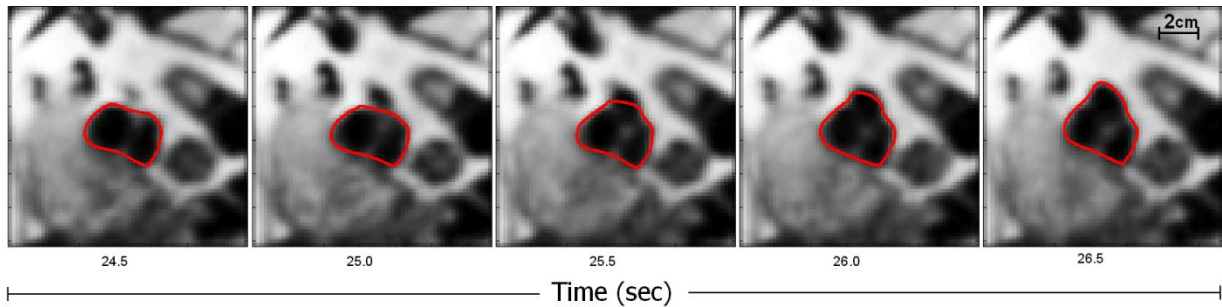


Figure 4.11 Example of contour deforming to bowel entering the two-dimensional imaging plane.

Extensive testing was performed to adjust weighting parameters before a set was found that provided satisfactory tracking for a majority of image sets. This is one of the disadvantages of such a technique, as tracking results may be sensitive to changes in input parameters. It is likely that tuning parameters individually to each image set would improve tracking results, however this is impractical for achieving real-time tracking. Automated, prospective parameter tuning would be ideal, and warrants investigation for future improvements to this work.

The algorithm in its current implementation does not perform with sufficient speed to enable real-time tracking at a sampling rate of 4Hz. The software performed with overall mean processing speed of 0.26 seconds per frame, as implemented on MATLAB and run on a 3GHz Intel Core processor. However, reduction of tracking speed can be achieved through by optimizing the implementation of the tracking algorithm.

4.4 Discussion

The demonstration of real-time bowel-tracking simulation for gated radiotherapy treatment offers promising clinical possibilities. Still, the implementation of real-time bowel tracking for radiotherapy or other MRI-guided interventions is not without its challenges. Both our work and others' have highlighted the inherent technical difficulties in tracking bowel over even relatively short durations [85, 94]. MR is sensitive to fluctuations in the inner contents of the bowel, leading to continuous changes in image contrast of the targeted region. Even when contrast fluctuations of the bowel are properly determined and handled, changes in the overall shape of the organ present additional complications.

Peristaltic motion makes the bowel more difficult to track than targets in the abdomen or thorax that primarily move with respiration, and out-of-plane motion poses additional complications. Cerviño et al reported on the use of several tracking methodologies on cine MR-images of lung lesions for radiotherapy [89]. Despite being relatively more rigid and systematic in motion as compared to bowel, authors still reported challenges in tracking lung targets. This was largely due to non-optimal search window constraints and complications arising from large out-of-plane motion. However, authors also demonstrated good success with a template-matching algorithm.

The use of the WNCC algorithm for tracking bowel motion demonstrated a high degree of robustness. The implementation of constraints on tracked bowel displacement proved to be useful in preventing gross tracking inaccuracies. Motion constraints used for detecting tracking results that are physiologically unrealistic, or used to focus a tracking algorithm's search window, are often used for tracking targets in the thorax [95]. Here we have used search window which is updated according to the new position of each tracked image. Due to arbitrary peristaltic movements, motion constraints for bowel-tracking applications should incorporate a higher tolerance for random motion and deformation than many other organs in the abdomen and thorax. The implementation of an additional motion constraint based on the WNCC coefficient (γ_{max}) proved to be very useful in prevention of unrecoverable tracking failures, however false positives (successes that are incorrectly flagged as failures) may contribute to smaller inaccuracies. More sophisticated testing conditions incorporating feature or texture matching approaches should be explored in future work.

The deformable tracking methodology presented here has demonstrated some robustness to intermittent changes in contrast and shape, however improvements are warranted. The level of confidence in tracking accuracy is certainly dependent on the severity of regional fluctuations. As discussed in the Methods, we use several parameters to automatically flag potentially poor tracking conditions and adapt the algorithm accordingly (such as the WNCC coefficient, contour perimeter changes, and internal distribution of pixel intensities within the contour region). Tracking results are likely sensitive to the adjustment of these parameter values, as well as the value of energy weighting parameters. Additionally, parameter thresholds defining the tradeoff between poor tracking conditions and simple fluctuations in local shape and contrast may vary across cases. Thus, a method to automatically and prospectively detect the most appropriate value of these parameters on a case-by-case basis is ideal, and warrants future work.

While the active contour model has demonstrated success in many medical imaging applications [92], it can be susceptible to inaccuracies (as demonstrated), and its implementation now exists in various forms due to investigators' efforts in optimizing its edge detection abilities. Several different variations were investigated during testing in efforts to improve tracking accuracy. Xu and Prince presented a technique to incorporate vector gradient flow in order to improve locating boundaries in

convex regions [96], however it proved unsuitably slow for real-time implementation. Cohen proposed the implementation of an additional ‘balloon’ force to guide the contour towards gradient regions [97], however this technique renders the contour susceptible to looping and entanglement. Geometric active contour models which use level set formulation were not explored in this work, but could prove more advantageous [92]. There are also many additional variations of the active contour model described throughout the literature, which could be explored [90, 92]. Future experimentation may identify one of these as a suitable technique for further enhancing deformable bowel tracking on cine MRI.

Another challenge in the development of a deformable bowel tracking method is in establishing a reliable evaluation method. Published literature on bowel tracking primarily explores its application for assessing bowel motility for diagnostic purposes. The standard evaluation method for these applications consists of a simple measurement of the diameter of the bowel [85, 98]. However, the application of bowel tracking for gated radiotherapy treatment is a different proposition entirely. The endpoint of interest is the accurate tracking of the borders of the bowel, so that the beam can be held when any part of the bowel enters high radiation regions. Thus, the disagreement between the tracked contour and border of the bowel must be evaluated. The frame-by-frame manual inspection method used here is incredibly cumbersome, making it inefficient for evaluating small changes made to the algorithm. Indeed, this proved challenging during the development phase, as detecting incremental improvements in tracking accuracy required lengthy sessions of manual inspection. Additionally, this type of evaluation is subjective. However we attempted to control for this by utilizing a single observer and categorizing errors using quantitative metrics (i.e. distance of the contour to bowel edge).

While this bowel tracking method is currently only implemented in an offline testing environment, the application of this work in a patient treatment setting carries significant implications in limiting bowel toxicity during the treatment of abdominal cancers. Such a clinical application could enable safer dose escalation to abdominal targets, which is marked by greater treatment efficacy [80, 81]. In addition to real-time intervention, this method could also be utilized as a retrospective dose evaluation tool to aid in treatment monitoring and adaptive therapy. By adapting initial bowel contours defined at the start of treatment to bowel segments tracked on images acquired during

treatment, the dose delivered to the bowel can be estimated using the treatment plan and delivery information. Monitoring dose to the bowel over subsequent treatment sessions may offer clinicians valuable assessment of potential bowel toxicity for individual patients. This could aid in clinical decisions or interventions designed to minimize or manage side effects.

Chapter 5

Process-Based Quality Management for Clinical Implementation of Adaptive Radiotherapy

The work presented in Chapters 2 – 4 introduces the use of novel technologies for enabling adaptive treatment schemes. Adaptive radiation therapy (ART) entails mid-treatment dose modification based on anatomical changes occurring throughout the treatment scheme, and has been the focus of much experimental study due to the potential treatment improvements it offers. However, ART introduces unique quality assurance (QA) challenges that make it difficult to implement in a clinical setting. In light of these unique QA challenges, no one has described a robust framework for its clinical implementation. We aim to address these obstacles by applying Failure Mode and Effects Analysis (FMEA), a process-based risk management technique, in order to identify high-priority errors and appropriate risk-mitigation strategies for clinical implementation of ART.

5.1 Background & Significance

Adaptive radiotherapy (ART) has garnered tremendous attention for years. Due to the advantages it may offer, there has been massive interest in ART as a potentially superlative treatment technique for patients who experience significant anatomical changes throughout treatment, including weight loss or gain, tumor shrinkage or growth, anatomical deformation and motion, and even metabolic or

functional changes of the tumor. Publications on tools, techniques, and potential benefits of ART are plenty. Investigational studies demonstrating significant improvement in treatment efficacy using adaptive techniques [5, 20] have motivated clinical implementation. The first reports of ART in a clinical setting are now emerging and reveal dosimetric advantages in the pelvis and head and neck [5, 20].

But despite the myriad of promising studies and sophisticated technology supporting clinical use of ART, its unique quality assurance challenges pose a major barrier. There are no clear answers as to how ART (especially intensity-modulated ART) will practicably fit within a quality assurance scheme that is both safe and efficient. Radiotherapy is comprised of many complicated processes which are reliant on different types of resources, such as software, hardware, and personnel. The major processes of radiotherapy treatment include simulation (patient imaging for planning), simulation image transfer and physician orders for planning, treatment planning, plan approval and preparation, and treatment. Intensity modulated radiation treatment (IMRT), which is now commonplace, is even more complicated than conventional treatment since a dynamic beam shaping device is used during treatment. Due to the complexity of these processes and the resources they utilize, QA measures are a fundamental component of the radiotherapy process in order to catch potential errors.

Recent position papers by ASTRO and AAPM have firmly endorsed pre-treatment patient-specific IMRT QA, which places online intensity-modulated ART at odds with the customary, time-tested practice of traditional phantom-based IMRT QA (see Appendix). Other standard forms of QA, such as detailed pretreatment plan reviews, are impractical when imaging, planning, and treatment delivery occur within minutes, not days or weeks. Furthermore, there is considerable uncertainty surrounding the potential risk and impact of ART-based errors. While analyses of radiotherapy error records from the last few decades have shed light on the origin and management of common treatment errors [99], no such data exists for ART. There is a common belief that ART is inherently riskier than standard radiotherapy, however there is no data demonstrating the magnitude or distribution of these risks throughout the ART process.

Given the scope of these challenges and degree of risk uncertainty, no robust quality management strategy has been established for ART. The lack of a framework for the safe implementation of ART continues to deter its practice, while the lack of ART practice limits the implementation of a data-driven quality management scheme. We aimed to address this void by employing a process-based approach, which has recently been endorsed by community experts as a means to optimize radiotherapy safety strategies [100-102], to evaluate the QA and safety needs for implementation of ART. Since ART-based error data currently does not exist, process-based analysis was performed using expert-based data from the forthcoming AAPM task group 100 (TG-100) as a baseline. Failure mode and effects analysis (FMEA, see Appendix) was used to identify and quantify risks for potential errors occurring during ART. For simplicity, a single scheme - online intensity-modulated ART with an integrated imaging, planning, and treatment system - was considered here. Through evaluation of the ART risk profile, vulnerabilities in the ART process were identified and risk-mitigation strategies are discussed to address high-priority QA and safety needs.

5.2 Materials & Methods

5.2.1 Failure Mode & Effects Analysis (FMEA)

FMEA involves the identification of process-based failure modes and their associated risks (see Appendix). Risk assessment is achieved by establishing 1) the probability of occurrence for each possible failure (*O*), 2) the severity of the failure effect if unmitigated (*S*), and 3) the probability that the failure will be undetected (*D*). Each is rated with a value from 1 (low probability/severity) to 10 (high probability/severity), and multiplied to achieve a single risk priority number (RPN):

$$RPN = O \times S \times D \quad (5.1)$$

5.2.2 FMEA for Adaptive Radiotherapy

An experienced team comprised of two clinical medical physicists, one clinical engineer, and one radiation oncologist was assembled. FMEA was executed for an online intensity-modulated ART scheme performed on an integrated (i.e. sharing a single database) planning, onboard imaging, and

treatment device equipped with some version of automated or semi-automated segmentation/planning software. A set of 216 radiotherapy failures composed by the forthcoming AAPM TG-100 was used as a basis for analysis [102] (Saiful Huq, personal communication, March 13, 2013).

The team first identified failure modes most relevant to the ART process. In the interest of isolating ART-specific failures, it was assumed that initial simulation and planning was first performed error-free. Onboard imaging and subsequent adaptive planning were regarded as the ART simulation and treatment planning processes (Figure 5.1). Failure modes related to simulation, data transfer, treatment planning (including directives, image fusion, anatomical segmentation, etc.), plan approval and preparation, and treatment were included. In total, 127 of 216 failures were identified as being most relevant and of high priority to an intensity-modulated ART scheme.

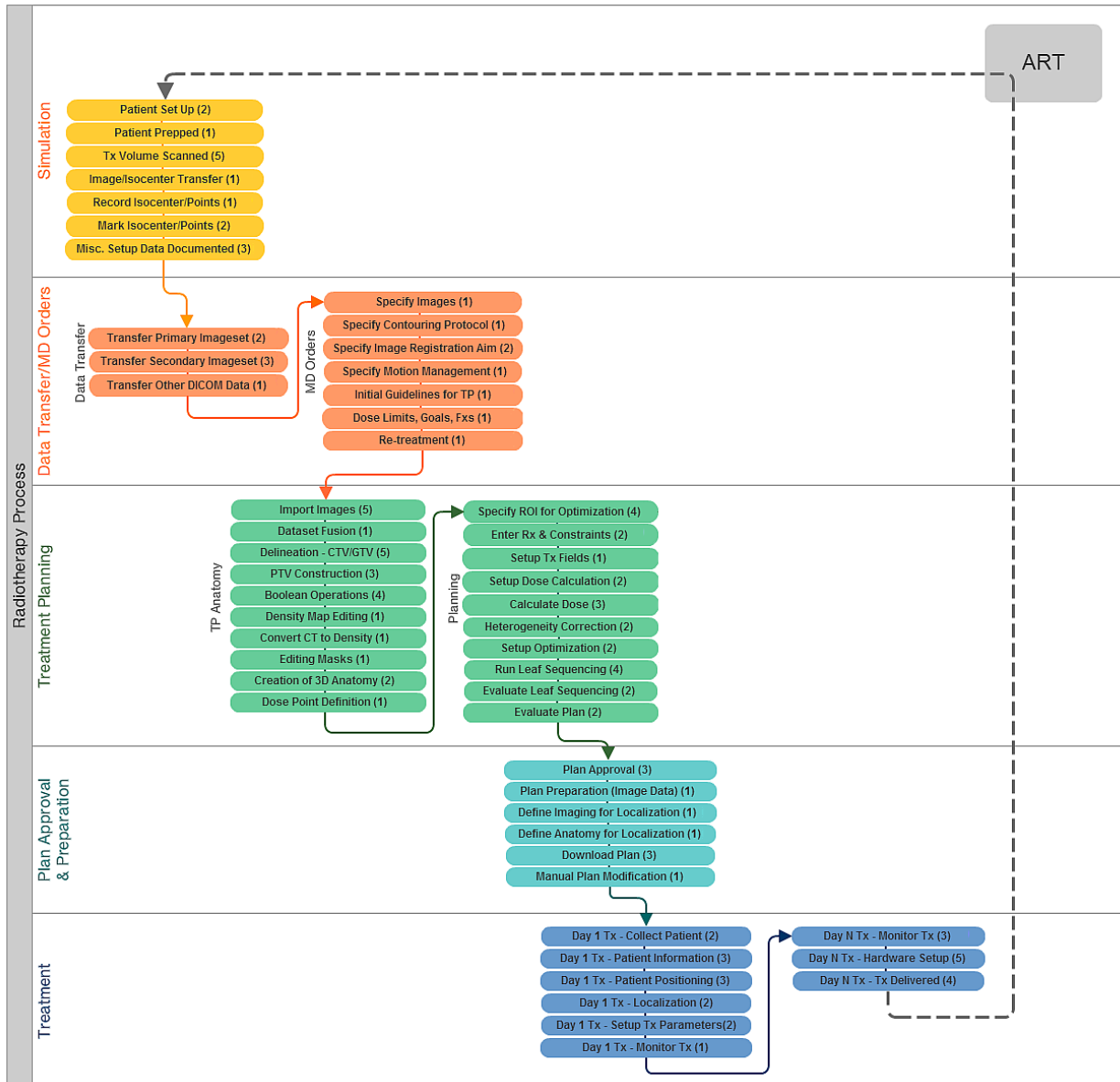


Figure 5.1 Flow diagram of major intensity-modulated ART processes and subprocesses. The number of failure modes per subprocess is included in parenthesis. Each subprocess is annotated to indicate an increase or decrease in average RPN of the associated failure modes. Critical failures are indicated by bold symbols. Process points necessitating QC strategies are also indicated. Corresponding QC strategies are listed in Table 2. QC = Quality Control

Each of the 127 failures was then evaluated for likeliness of occurrence (O), outcome severity (S) and likeliness of being undetected (D). The FMEA rating scale proposed by AAPM TG-100 was referenced for scoring (Table 5.1). Replicating the methodology employed for TG-100, it was assumed that no specialty QA tools (including patient-specific QA) or increased staffing was utilized

for ART. Factors relating to increased pressures (e.g. time constraints, real-time distractions, etc.) were considered, and their effects on O and D values were taken into account. The team also considered changes in overall severity of failures due to error accumulation over multiple fractions. Using the associated TG-100 values for standard IMRT as a baseline, the team established new O, S, and D values for each potential failure upon consensus agreement, and new RPN values were calculated.

Table 5.1 Occurrence (O), severity (S), and detectability (D) values proposed by AAPM TG-100 for the radiotherapy process. (Re-created from AAPM Monograph No. 36 [103])

Value	Occurrence (O)		Severity (S)		Detectability (D)
	Qualitative	Frequency	Qualitative	Categorization	Estimated probability failure goes undetected (%)
1	Failure unlikely	$(\frac{1}{10,000})$	No effect		0.01
2		$(\frac{2}{10,000})$	Inconvenience	Inconvenience	0.2
3	Relatively few failures	$(\frac{5}{10,000})$	Minor dosimetric error	Suboptimal plan or treatment	0.5
4		$(\frac{1}{1,000})$	Limited toxicity or underdose	Wrong dose, dose distribution, location or volume	1.0
5	<0.2%	Potentially serious toxicity or underdose	2.0		
6	Occasional failures	<0.5%	Possibly very serious toxicity	Very wrong dose, dose distribution, location or volume	5.0
7		<1%			10
8	Repeated failures	<2%	Catastrophic		15
9		<5%			20
10	Failures inevitable	>5%			>20

Failures characterized by $O \geq 6$ (at least moderate occurrence), $S \geq 7$ (serious injury or death) and $D \geq 5$ (at least a moderate chance of going undetected), yielding an RPN equal to 210, were categorized as high priority. For simplicity, the team designated failures with an $RPN \geq 200$ as potentially critical. Finally, quality control tools, resources and processes were identified for points of critical failure.

5.3 Results

5.3.1 Overall Trends

ART demonstrated a wider range and higher maximum of O, D, and RPN values compared to standard IMRT (Table 5.2). RPN values increased for 38% ($n = 48/127$) of potential failures, with 75% ($n = 36/48$) attributed to failures in the segmentation and treatment planning processes. Increased O values were observed for 26% ($n = 33/127$) of potential failures, with 36% ($n = 12/33$) attributed to failures in anatomical segmentation during treatment planning. S values increased for only 1% of potential failures. In many cases, the cumulative severity of failure modes prone to cause systematic errors was deemed less severe. It was reasoned that a systematic error occurring for standard IMRT would affect every treatment fraction leading to a larger cumulative error, while a systemic error occurring for ART would affect only the fractions for which the ART plan was used. D values increased (i.e. decreased probability of detection) for 44% ($n = 56/127$) of potential failures, with 86% ($n = 48/56$) attributed to failures in the segmentation and treatment planning processes. This was largely due to increased time constraints, user inattention, and inadequate training of onsite personnel.

Table 5.2 Mean, standard deviation (σ), minimum, maximum, and range values for occurrence (O), severity (S), detectability (D), and risk priority number (RPN) values for 127 standard IMRT and intensity-modulated ART steps.

	Standard IMRT				Intensity-modulated ART			
	O	S	D	RPN	O	S	D	RPN
Mean $\pm \sigma$	5 \pm 1	7 \pm 1	6 \pm 1	188 \pm 60	4 \pm 2	7 \pm 1	6 \pm 2	174 \pm 105
Minimum	2	3	2	46	1	3	1	11
Maximum	7	9	8	366	8	9	9	441
Range	5	6	6	320	7	6	8	430

5.3.2 Process-specific Trends

There was a reduction in O and D values for simulation processes and treatment planning directives due to the availability of prior knowledge of immobilization, imaging, and treatment directives given for the initial plan. For the majority of segmentation and planning failures, RPN values increased. This was largely due to tighter time constraints and user inattention. O and D values were reduced for some failures due to the availability of the initial treatment plan as a reference. These included failures in specifying optimization goals, planning constraints, prescription information, dose calculation parameters, and beam energy.

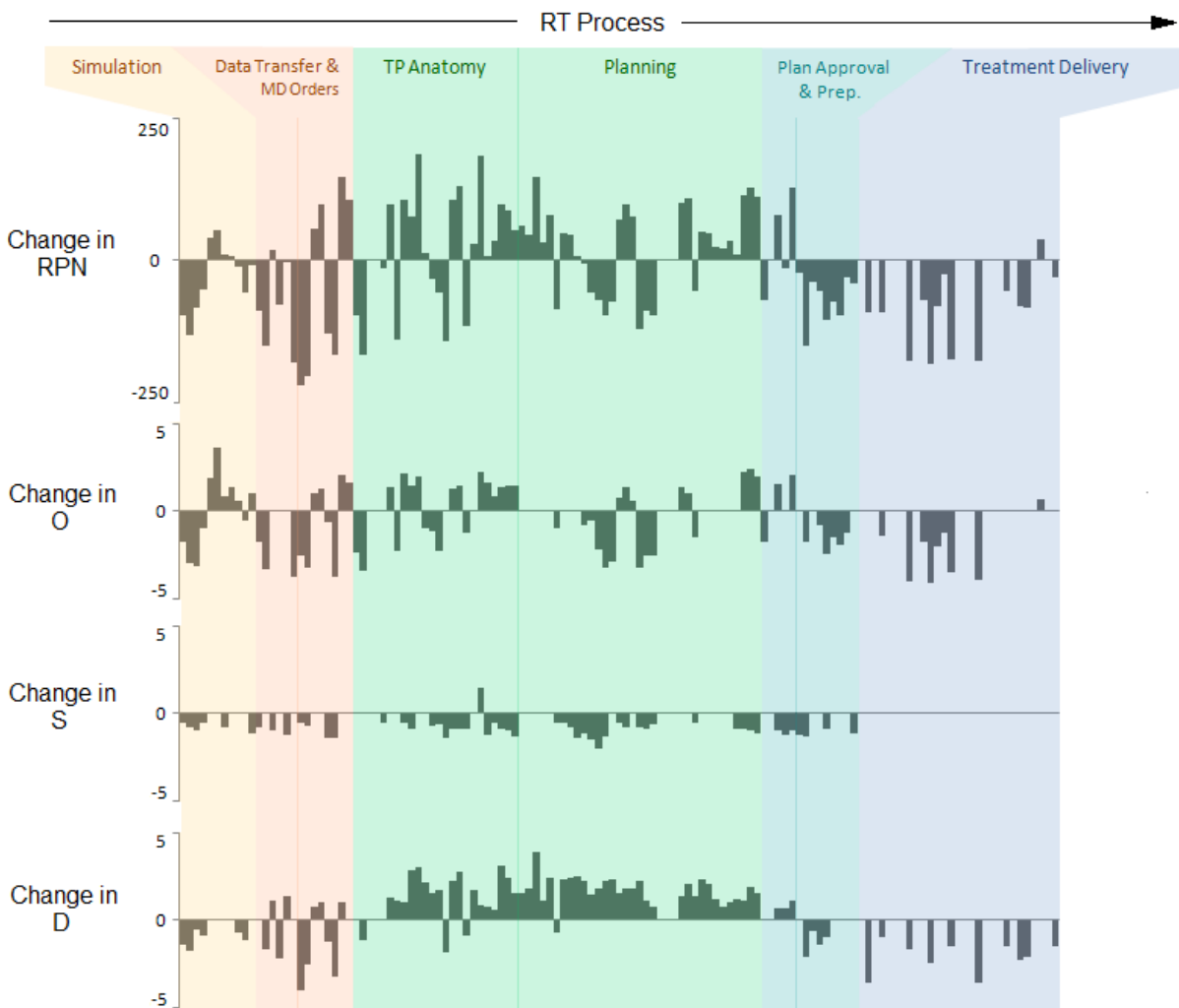


Figure 5.2 Change in RPN, O, S, and D values for intensity-modulated ART (relative to standard IMRT) for each potential failure. (TP = Treatment Planning)

Increased RPN values for plan approval failures were attributed to increased time constraints, user inattention, and inadequate training of onsite personnel. Plan preparation, however, experienced reduced RPN values. Failure occurrence decreased for many plan preparation failure modes (preparation of localization images, transferring the plan to the delivery system, etc.) due to the integrated nature of the ART system. The probability of detecting these errors was improved since the image and treatment data was handled by staff immediately before transfer to the machine, making any discrepancies more obvious than they otherwise would be.

Reduction of treatment delivery RPN values largely corresponded to reduction of daily setup, positioning and localization errors, which were improved by ART. The integrated nature of the ART system reduced the likeliness of inconsistencies between the planning and treatment systems. RPN values for severe, systematic delivery system failures experienced no substantial changes.

5.3.3 Critical Failures

Forty-three of 127 potential failures analyzed for intensity-modulated ART were identified as potentially critical ($RPN \geq 200$). Under the same criteria, 51 failures were identified as potentially critical for standard IMRT. While ART introduced 13 new critical failures, 30 critical failures were common between ART and standard IMRT (Figure 5.3). RPN values were higher in the majority ($n = 23/30$) of these common failures for ART than for standard IMRT. Delineation errors, optimization errors, and equipment failures during treatment delivery remained as some of the highest ranked for both standard IMRT and intensity-modulated ART, due to difficulties in detection. Most failures were elevated to a ‘critical’ rating due to increased time constraints, real-time distractions, and inadequate training of onsite personnel.

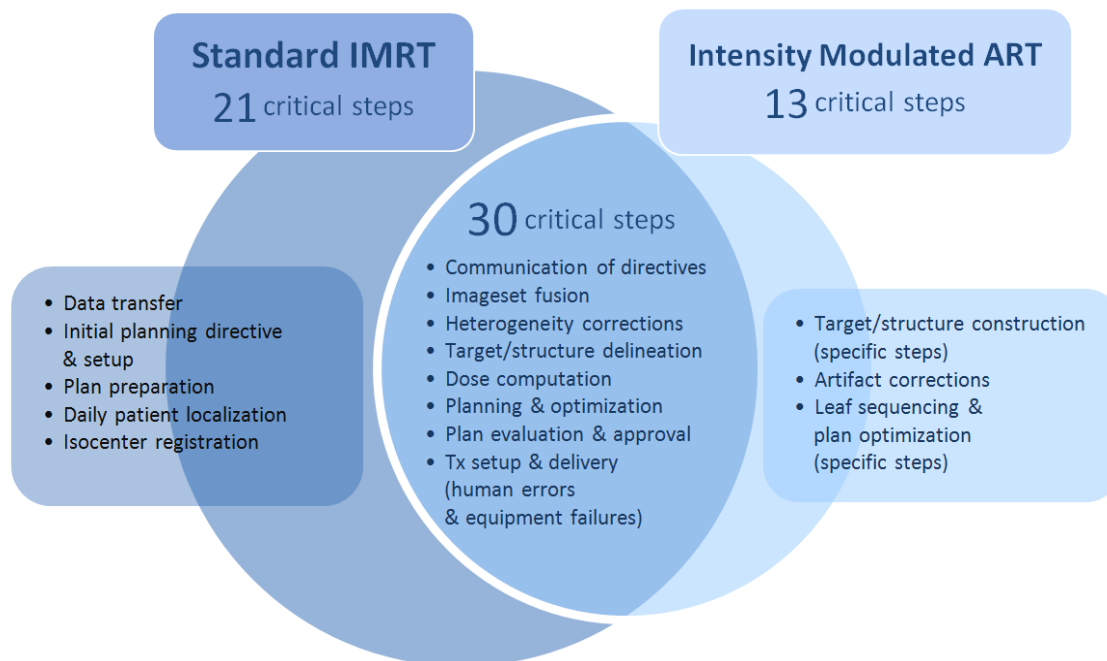


Figure 5.3 Processes with occurrence of common and unique critical failures for intensity-modulated ART and standard IMRT. (Tx = treatment).

5.3.4 Quality Control Strategies

Nine major points of quality control for critical failures were identified. Strategies for each point of critical failure are listed in Table 5.3 and referenced in the process map displayed in Figure 5.4. Key strategies are discussed below.

Failures associated with isocenter documentation and communication of planning and fusion directives for adaptive treatment (including the proper documentation and interpretation of ‘tracked treatment’ from fraction to fraction) necessitate a combination of well-documented protocols, stable clinical workflow, staff training, and a reliable record management system. Electronic physician ordering and whiteboard systems are also an effective means for mitigating communication failures [104, 105]. Quality control measures for dataset fusion include both automated fusion tools and trained manual inspection [106].

Although automated segmentation tools will be commonplace for online ART to increase efficiency and reduce human error, automated quality control software is necessary for error detection. A system for inspection and comparison of the position, size, shape and volume of newly contoured structures to previously contoured structure(s) would enable an evaluation of contour accuracy using quantifiable metrics. Commercial software tools such as ImSimQA^{contour} (Modus Medical Devices, Inc.) and StructSure (Standard Imaging, Inc.) already offer similar capabilities designed to test inter-user and inter-system agreement, and could be extended for detection of re-contouring errors. For application to ART, appropriate metrics and tolerances for mobile and deformable structures must be established. One option is to use a clinical database of acceptable ranges. Tolerances could also be constructed based on physiologic models. Alternatively, a redundancy check using a separate, independent auto-segmentation system could also be employed.

Table 5.3 Mitigation and QC strategies for ART processes with critical failures.

Failure	Quality Control (QC) Strategy	Prototypes and Commercial Tools
1) Isocenter documentation	Automated isocenter capture, checklists, monitoring trends in daily patient shifts	
2) Mis-communication of planning directives and failure to properly account for dose accumulation	Well-defined protocols, stable clinical workflow, staff training, integrated record management, electronic physician order and whiteboard systems	Santanam [105], Brewster [104]
3) Poor imageset fusion	Automated fusion tools, specialty training for onsite staff	
4) Incorrect target/structure delineation and construction	Automated contour integrity verification software	ImSimQA ^{contour} , StructSure (not specifically designed for ART)
5) Poor plan optimization and or incorrect dose computation	Automated software verifying: <ul style="list-style-type: none"> • dose computation 	RadCalc (LifeLine Software), IMSure (Standard Imaging), muCheck (Oncology Data Systems Imaging), Sun 2012 [107]
	<ul style="list-style-type: none"> • leaf sequencing 	Xing 2000 [108]
	<ul style="list-style-type: none"> • plan integrity 	Yang 2012 [109]
6) Poor plan review	Automated decision support software	Zhu 2011 [110], Moore 2011 [111]
7) Corruption of plan data during transfer to treatment machine	Independent verification software comparing data stored on the planning and delivery system	QAPV (IHE-RO) [112]
8) Failures in treatment parameter setup on treatment machine	Simulated delivery, pre-treatment (running gantry rotations and MLC patterns without dose output)	
	Retrospective MLC QA, post-treatment	Sun 2012 [107]
9) Failures occurring during treatment delivery	Transmission detectors	In-vivo EPID dosimetry, DAVID harp chamber, MatriXX ^{Evolution} , Investigational transmission detectors (Islam 2009 [69], Goulet 2011 [113], Wong 2012 [114])
	Real-time MLC monitoring	Jiang 2010 [115]

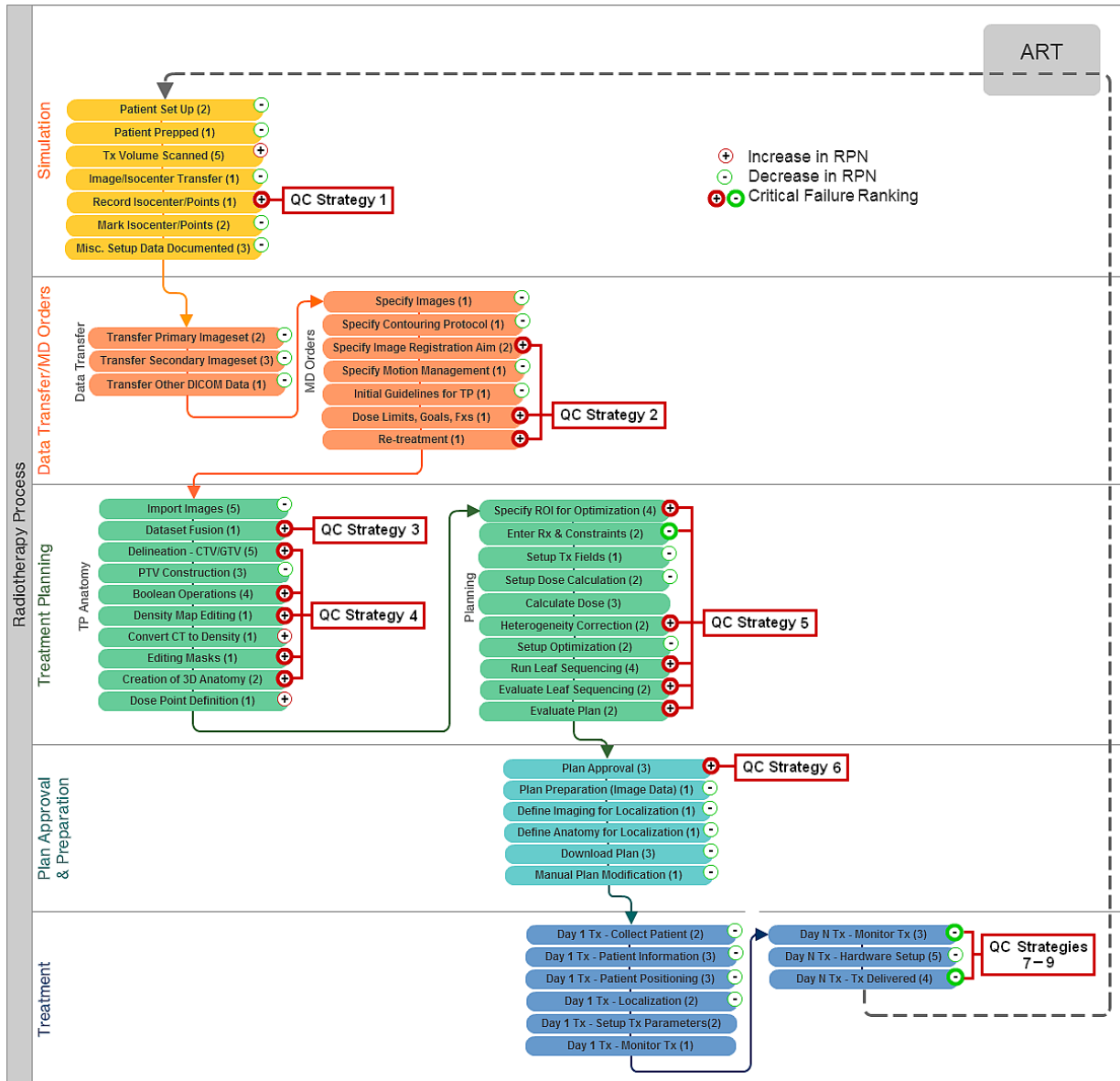


Figure 5.4 Flow diagram of major intensity-modulated ART processes and subprocesses. The number of failure modes per subprocess is included in parenthesis. Each subprocess is annotated to indicate an increase or decrease in average RPN of the associated failure modes. Critical failures are indicated by bold symbols. Process points necessitating QC strategies are also indicated. Corresponding QC strategies are listed in Table 5.3. QC = Quality Control

Automated quality control software will also be instrumental in detecting planning errors and facilitating more effective plan review. Commercial tools like RadCalc (LifeLine Software, Inc.) and IMSure (Standard Imaging, Inc., Middleton WI) are readily available and can be implemented into an

online ART scheme as a verification measure, as described by Peng *et al* [116]. Several groups have proposed more comprehensive tools for plan verification. Yang and Moore have described a software tool for automated verification of plan integrity, which includes specific error detection for contours (empty, incomplete, etc.), beams (inconsistencies in isocenter, type, etc.), dose calculation parameters, IMRT optimization, and other plan components [109]. Authors found that implementation of their tool led to a decrease in plan-related failures in the clinic, and it is now standard use in their clinical practice. This type of comprehensive automated analysis is ideal for rapid error detection of adaptive plans.

Plan review failures (i.e. approval of poor plans) can be partially mitigated by the quality control software just described, however those tools are designed to specifically address technical planning errors. Decision support software will be necessary for this purpose. Software enabling easily-interpreted automated comparisons between planning goals and achieved goals should be commonplace on ART planning software. A more sophisticated solution is to incorporate an automated check against a database of quality-rated plans. This approach for plan evaluation has been explored using various methodologies, including machine learning [110] and pareto-front type modeling [111]. Moore *et al* demonstrated that the clinical implementation of such a feedback system during planning of head and neck and prostate cases could improve tissue sparing and planning efficiency [111]. This approach could expedite and stabilize the plan review process by establishing a robust baseline for achievable dosimetric goals specific to the site, planning, technique, patient geometry, and other parameters.

Alternatives to the traditional patient-specific phantom-based IMRT QA process (which was assumed to be absent for the analysis) for detection of treatment parameter transfer/setup failures should be considered. Data transfer errors occurring between the planning and/or R&V systems to the treatment machine could be detected with independent software that performs automated comparisons between the parameters housed on each system. The ongoing development of the QAPV (Quality Assurance with Plan Veto) profiler by the IHE-RO group (Integrating the Healthcare Enterprise - Radiation Oncology) would ideally support such a solution [112]. To verify that treatment parameters are correctly uploaded by the treatment machine, additional measures

would need to be taken. One approach is to perform a ‘simulated’ treatment before delivery, which would entail running the treatment machine through planned gantry angles and multi-leaf collimator (MLC) patterns without activating the radiation beam. Comparison of machine delivery log files to planned patterns could reveal failures – a practice that has been shown to be both feasible and effective for post-delivery verification [107]. This approach is also much less resource intensive than physical measurement-based QA. Retrospective post-treatment QA (simulated or physical phantom-based) could be adequate for delivery systems that demonstrate time-tested stability. It is important to note, however, that these methods (patient-specific IMRT QA included) do not detect clinical planning errors such as suboptimal or poor dosimetry, which collectively yielded higher RPN values than treatment parameter setup errors for both standard IMRT and ART.

Pretreatment verification is also not necessarily sensitive to failures occurring *during* delivery, one of the highest rated critical failures for both standard IMRT and ART. In-vivo EPID dosimetry is very effective. In an analysis performed by Ford *et al*, EPID dosimetry was found to be one of the most effective QA methods of all those commonly available, with the ability to detect errors that even pre-treatment phantom-based IMRT missed [117]. Investigational studies demonstrate that real-time EPID dosimetry could even be used to detect errors as they occur [118], enabling immediate intervention. Transmission detectors that can be mounted onto the gantry head for online treatment monitoring have also been under development by many groups [69, 113, 114], and could play a key QA role for ART. Several of these devices are commercially available including the MatriXX^{Evolution} transmission detector (IBA Dosimetry, Germany), which is marketed as an arc treatment QA device, and the DAVID harp chamber device (PTW, Germany), which is specifically designed for real-time dosimetric monitoring. Although not based on direct dosimetric measurements, post-treatment or real-time monitoring of MLC log files is a simpler solution and has been demonstrated by several groups [107, 115]. It has been suggested that supplementing MLC log file analysis with independent dose calculations may be a better QA method than traditional measurement-based approaches due to increased sensitivity to dose calculation errors, heterogeneity errors, and beam modeling errors [107]. Regardless of the approach, intra-fraction monitoring of treatment delivery can improve quality control and error detection for both standard IMRT and ART, and is likely to become an integral part of clinical QA as tools become more practical and widely available.

Many of these tools are not yet commercially available, however their need is widely recognized. Most (if not all) of these tools can be of value for standard IMRT as well. As these tools continue to be developed, data demonstrating their efficacy will offer valuable insight into their usefulness for ART.

5.3 Discussion

Evaluation of the ART risk profile suggests that ART does not substantially increase risk as compared to standard IMRT. While ART was particularly more vulnerable to failures in planning and delivery, most of the critical failures were deemed high-risk for both ART and standard IMRT. It is evident that many processes in the RT planning and delivery phase are just inherently risky. Critical risks unique to intensity-modulated ART were deemed manageable with proper mitigation. Furthermore, while ART experienced some elevated risks, a reduction in risk was observed for many failure modes. In particular, risks associated with patient positioning and localization failures were substantially reduced, illustrating a primary advantage of adaptive techniques.

Examining the risks of intensity-modulated ART with respect to risks of standard IMRT is intended to offer clinical context, and not to draw direct comparisons between the overall levels of risk of these two treatment techniques. Overall risk will be dependent on cumulative error and the frequency and nature of plan adaptation, which may be difficult to quantify. The use of FMEA, however, enables identification and comparison of process-specific risks. Using the recommended FMEA values of TG-100 provides a well-developed and standardized baseline for analysis, and allows for the comparison of QA needs for standard and adaptive treatment. The use of a standardized baseline is an important feature of this work, since the assessment of risk values can be subjective across groups performing the FMEA. However, the major limitation of this analysis is that it relies on expert opinion. As ART is brought to practice, data-driven analysis will provide a more quantitative assessment of risk. For example, Ford *et al* [117] have demonstrated how the use of a clinical error database can be used to identify common failures and assess the effectiveness of quality control strategies for standard radiotherapy.

While process-based quality management is a relatively new practice for the radiotherapy field, it offers a pragmatic approach to a complex problem. When viewed within the traditional quality management framework, developing an implementation strategy for ART is daunting. Conventional QA practices generally embody a micromanagement strategy which emphasizes detection of technical errors and device-based testing. This is problematic in an environment of increasingly more complex systems, and some conventional QA methods are becoming impractical. For example, there is now evidence that phantom-based IMRT QA is one of the least effective routine QA measures [117], and some have suggested that software tools could potentially replace measurement-based pretreatment QA as RT equipment becomes increasingly stable [107, 119]. This position is controversial, and will undoubtedly continue to be a point of contention.

At the very least, the development of alternative strategies, such as onboard QA devices and quality control software, indicates that investigators and vendors alike are taking measures to overcome such challenges. Furthermore, the recent advocacy of process-based approaches for RT quality management [100-102] indicates an appreciation for the shifting QA paradigm by community leaders. This study demonstrates the value of such a process-based technique in facilitating the safe clinical implementation of adaptive treatment.

Appendix

Extended Definitions & Descriptions

A.1 Calypso Electromagnetic Tracking System

Real-time electromagnetic tracking has recently been introduced into clinics for enabling point-based target localization, both before and during treatment. This technology utilizes continuous tracking to monitor the target isocenter position. The Calypso® 4D Localization System (Varian Medical Systems, Inc., Seattle WA) uses an electromagnetic array to track passive Beacon® electromagnetic transponders (8.5x1.85-mm glass-encapsulated copper coils) implanted in the patient's tumor.



Figure A.1 Calypso electromagnetic tracking array. Inset displays the implantable electromagnetic transponders (Image courtesy of Calypso Medical).

The first clinical application of the Calypso System was in prostate cancer patients. Implantation by general clinical protocol for prostate cancer patients involves insertion of three transponders placed at the left base, right base, and apex of the prostate. The stability of these implanted transponders has been previously reported [120]. The three-dimensional coordinates of each transponder, with

respect to treatment isocenter, are determined from the CT scan taken during simulation. These coordinates are entered into the Calypso System to serve as the planned treatment position.

During localization on the treatment machine, the electromagnetic array, a rectangular panel encasing electromagnetic coils, is positioned over the patient's target area. The coils emit a radiofrequency signal to excite the implanted transponders. Each transponder contains a RLC circuit, which is tuned to a unique resonant frequency between 300–500 kHz. The transponders are excited sequentially, and each returns a signal at a specific frequency allowing for their positions to be detected relative to the array at a nominal sampling rate of 10Hz. The array (equipped with reflective surface markers), is in-turn tracked by three infra-red cameras mounted to the ceiling, providing absolute positional information of the transponders. The target isocenter position as calculated from the transponder locations is tracked and reported throughout treatment. The system also monitors ambient radiation in the treatment room for synchronization with tracking data, enabling identification of target motion collected during active radiation delivery.

Previous studies done by Balter *et al* and Parikh *et al* have documented the submillimeter accuracy of the system within a volume of 14x14 cm in width, and 27cm in depth when tracking transponders moving up to 3cm/s [42, 43]. The tracking latency of the system is reported to be 303ms [121].

The Calypso System is designed for both set-up localization and continuous monitoring of isocenter position. At the time of initial localization, the Calypso System reports translational shifts and rotational offsets, as compared to the planned transponder positions. The user is allowed to set patient-specific rotational limits for patient set-up. If the system detects target rotation greater than this value, the user is warned during initial localization. Additionally, the user is allowed to set patient-specific motion limits of translational isocenter movement. The system is designed to warn the user if the isocenter exceeds these limits during treatment. Limits for each axis (lateral, anterior-posterior, and superior-inferior) are set independently, allowing for asymmetrical motion boundaries.

Tracking data from each treatment fraction is stored by the Calypso System on the tracking station. The clinical system at our institution is equipped with supplementary functionality allowing for

exportation of individual transponder positions to an external computer. Individual tracking files are exported into an Excel (Microsoft Corporation) spreadsheet via a non-clinical software application. Data exported for each fraction consists of individual transponder and isocenter positions as a function of time. Also included is synchronized radiation detection data.

A.2 Gamma Dosimetric Analysis

The Gamma dosimetric analysis method is a QA metric that compares an evaluated dose distribution to a reference dose distribution [122]. It takes into account the dosimetric difference and dosimetric distance to agreement (DTA) between the two distributions, simultaneously. The rationale behind this composite analysis is that the dose difference and DTA metrics are actually complementary. The dose difference metric describes the difference in dose between the evaluated and reference distribution at a single point, and is therefore sensitive to regions with steep dose gradients. Conversely, the DTA metric is sensitive to regions of shallow dose gradients for interpolated dose distributions, since it measures the distance between the nearest points of equal dose on the evaluated and reference dose distributions [123]. By combining these two into a single metric (the gamma metric), false positives due to hyper-sensitivity are reduced. The gamma metric identifies failures only when both the dose distance and DTA metrics simultaneously exceed user-defined values (commonly 3%/3mm for clinical use).

A.3 ViewRay Onboard MRI System

The hybrid MRI-treatment unit is comprised of an open, split-solenoid low-field MRI co-registered to a three-head ^{60}Co gamma-ray radiation delivery device. The MRI has a nominal field strength of 0.35T and is a variant of the Siemens MAGNETOM product used for intraoperative imaging. The split coil design allows for an unobstructed path from the treatment source to the patient, which eliminates a possible source of beam attenuation. The design also allows for the radiofrequency (RF) shield, 12-channel receiver coil, and patient couch to remain within the beam path, as these components contribute minimal attenuation. The imaging and treatment isocenter are co-registered, allowing for simultaneous target treatment and localization (Figure A.2).

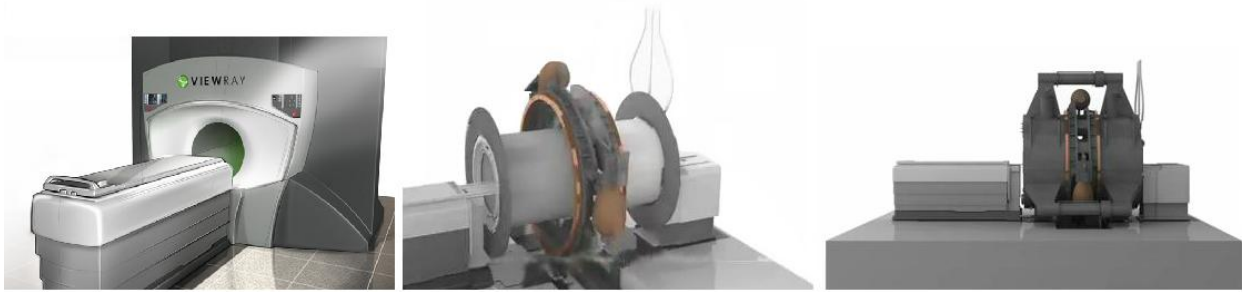


Figure A.2 The ViewRay System, a hybrid MRI-⁶⁰Co radiotherapy device (images courtesy of ViewRay, Inc.).

The system is designed to enable pre-treatment volumetric MRI for positioning and adaptive planning. The system software is equipped with deformable image registration algorithms, a re-planning interface, and a fast dose calculation engine. During an adaptive workflow, the patient is positioned on the treatment couch, a volumetric MRI is acquired, and a decision to re-plan or proceed with the current plan is made. The system is also designed to enable intra-fraction cine MRI for motion planning and mid-treatment intervention. During the tracking and intervention, the target is selected and contoured, the target is automatically tracked during treatment, and the beam is held when the target leaves the path of the treatment beam due to motion.

The superconducting magnet, RF coils, and gradient coil are specifically designed to allow for simultaneous operation with the radiotherapy unit. The superconducting magnet is cooled with liquid helium. The gradient system is comprised of three gradient coils oriented in the x-, y-, and z-axes and has a maximum strength of 18 mT/m and a maximum slew rate 200 T/m/s. The imaging field of view of radius of 70 cm, centered at treatment isocenter. The low-field design of the MRI scanner bypasses many obstacles that would be encountered with a standard-field design.

A fundamental complication of merging an MRI unit with a radiotherapy treatment unit is managing the effect of the magnetic field on the treatment beam and delivered dose distribution. The standard linear accelerator (LINAC) design relies on the use of a linear beam of electrons to produce radiation. However, in the presence of a magnetic field, the trajectory of the beam is governed by the Lorentz force,

$$\vec{F} = q(\vec{v} \times \vec{B}) \quad (\text{A.1})$$

which describes the force acting on a charged particle (q) moving within a vacuum at velocity \vec{v} , within a magnetic field \vec{B} . Without complete shielding from the magnetic field, accelerated electrons cannot be directed along a straight path. This force also effects the delivered dose distribution. However, by employing a low-field MRI design, the effect of the Lorentz force is reduced. Furthermore, the use of naturally emitting Cobalt radiation eliminates considerations for LINAC-based radiation and its specialized shielding requirements. This feature also eliminates the concern of RF interference between the LINAC and the RF transceiver system of the MRI. Finally, the low-field design of the MRI results in less magnetic susceptibility artifacts and image distortions, which are proportional to the field strength [124]. This is particularly important for targeting accuracy during radiotherapy, since patient alignment and dosimetric planning accuracy is reliant on the accurate spatial representation of the patient's anatomy.

Only the imaging component was utilized in this work. The spatial integrity of the onboard imaging unit has been characterized by Hu *et al* [125]. Investigators reported a geometric distortion of approximately 0.2mm within a radial distance 100mm from isocenter, and 0.6mm within a radial distance of 175mm from isocenter for static planning images. Geometric distortion for cine images was approximately 0.1mm within a radial distance of 175mm from isocenter. Geometric distortion always remained <1mm within a radial distance 100mm from isocenter, and <2mm within a radial distance of 175mm from isocenter for both static planning and cine images. The maximum signal-to-noise ratio (SNR) deviated from the mean SNR by values of 1.62%, 6.98%, and 7.22% the body coil, combined torso coil and combined head/neck coil, respectively. Investigators reported a RF phase stability of <2%, through measurement of the FID (free induction decay) time for both for both real and imaginary channels.

The ViewRay system is designed to for fast image acquisition, in order to minimize pre-treatment imaging time and the maximize intra-fraction imaging rate. Two imaging sequences were used for patient imaging. The TrueFISP imaging sequence was used to acquire a majority of patient volumetric imagesets (Chapter 3) sets and all real-time cine imaging of the bowel (Chapter 4). The Siemens TrueFISP sequence is designed for use in cardiac imaging due to its fast acquisition time. It is characterized by a high flip angle and short TR/TE. The transverse magnetization is preserved during acquisition, which results in fast acquisition of a T2/T1-weighted signal with high SNR. A TurboFLASH sequence was used to acquire two of 14 volumetric patients imagesets (Chapter 3). Like the True FISP imaging sequence, it is characterized by a low TR. However it is a T1-weighted sequence due to the saturation-recovery magnetization preparation performed before the FLASH acquisition.

A.4 Active Contour Model

The traditional active contour model was introduced by Kass *et al* in 1988 [91]. This traditional active contour model, also known as “snakes”, is based on the premise of minimizing the energy of the contour (E_{snake}), which is comprised of energies contributed by internal (E_{int}) forces and image (E_{ext}) forces.

$$E * = \int_0^1 E_{snake}(v(s)) ds \quad (A.2)$$

$$= \int_0^1 E_{int}(v(s)) + E_{ext}(v(s)) ds \quad (A.3)$$

where

$v(s) = (x(s), y(s))$ describes the position of the snake parametric form.

The internal energy represents the energy contributed by the contour itself modeled as a spline, and is composed of the weighted sum of: 1) a first-order term which represents the membrane energy, and 2) and a second-order term which represents the thin plate energy.

$$E_{int} = (\alpha(s)|v_s|^2 + \beta(s)|v_{ss}|^2)/2 \quad (\text{A.4})$$

where $\alpha(s)$ and $\beta(s)$ control the relative weights of the first- and second-order terms, respectively. As these weights approach zero, the contour becomes more discontinuous.

The external energy E_{ext} includes the energy contributed by images forces (E_{image}) and interactive force constraints imposed by the user (E_{con}). This constraint energy is traditionally described as applied by interactive user intervention. For the purposes of our implementation, E_{ext} is equal to E_{image} . Thus:

$$E_{ext} = E_{image} \quad (\text{A.5})$$

$$= w_{line}E_{line} + w_{edge}E_{edge} + w_{term}E_{term} \quad (\text{A.6})$$

where w_{line} , w_{edge} , and w_{term} control the weights of the line energy (E_{line}), edge energy (E_{edge}), and terminal energy (E_{term}), respectively. In its traditional form, the line energy is represented as the image intensity (ie. the image I itself),

$$E_{line} = I(x, y) \quad (\text{A.7})$$

the edge energy is represented as the image gradients convolved with Gaussian G with a standard deviation σ ,

$$E_{grad} = -(G_\sigma * \nabla^2 I)^2 \quad (\text{A.8})$$

and the terminal energy is represented as

$$E_{term} = \frac{\partial \theta}{\partial n_{\perp}} \quad (\text{A.9})$$

$$= \frac{\partial^2 C / \partial^2 n_{\perp}}{\partial C / \partial n} \quad (\text{A.10})$$

$$= \frac{C_{yy}C_x^2 - 2C_{xy}C_xC_y + C_{xx}C_y^2}{(C_x^2 + C_y^2)^{3/2}} \quad (\text{A.11})$$

given that

$$C(x, y) = G_{\sigma} * I(x, y) \quad (\text{a smoothed version of the image } I), \quad (\text{A.12})$$

$$\theta = \tan^{-1} \frac{C_y}{C_x} \quad (\text{the gradient angle}), \quad (\text{A.13})$$

$$n = (\cos \theta, \sin \theta) \quad (\text{the unit vector along the gradient direction}), \quad (\text{A.14})$$

$$n_{\perp} = (-\sin \theta, \cos \theta) \quad (\text{the unit vector perpendicular to the gradient direction}). \quad (\text{A.15})$$

The E_{line} term attracts the contour towards high or low intensities (characterizing black or white lines in a grayscale image). Low (dark) intensities translate to low energy, which attracts the contour. Weighting E_{line} with a value < 0 negates this relationship, so that high intensities represent low energies, attracting the contour. The E_{edge} term attracts the contour towards edges, which are represented as image gradients, and the combination of E_{edge} and E_{term} is used to attract the contour towards line segment terminations and corners.

A.5 IMRT QA

Intensity modulated radiotherapy (IMRT) is a highly conformal form of treatment, and is more complex than conventional techniques. During IMRT, the beam is shaped to the target dynamically (either between treatment beams or during beam delivery). Due to the mechanical complexities and the high dose output of this delivery method, it can be considered as a riskier treatment method than conventional dose delivery. As such, comprehensive dosimetric testing executed on a per patient basis is regularly performed for IMRT. Furthermore, reimbursement policies set forth by the Centers for Medicare and Medicaid Services (CMS) stipulate that planned dose must be verified for IMRT treatments. Patient-specific dose verification for IMRT treatments is traditionally performed by delivering the planned dose to a solid water phantom implanted with planar film or ion chambers. The value of this technique is that phantom-based QA accounts for multiple parameters that simulated calculations do not, such as correct multi-leaf collimator positions and gantry angles. Other methods include delivering planned dose to diode/ion chamber arrays, or using MV portal imaging dosimetry. The delivered dose can then be compared to the planned dose to ensure that the plan or delivery was not corrupted.

A.6 Failure Mode and Effects Analysis (FMEA)

Failure mode and effects analysis (FMEA) is a technique that is well-suited for process-based risk management and has recently been suggested as the future framework for radiotherapy QA by the AAPM [120]. The FMEA method, which is used routinely in industrial engineering fields, facilitates safety improvement through identification of process failure modes and their associated risks.

In order to identify all possible modes of failures, the entire process is generally first mapped out as a process tree so that distinct subroutines can be distinguished. Within each subroutine there are possible modes of failure, which can be mapped out as a fault tree detailing the possible failure and causes. For example, a patient immobilization subroutine could involve a setup failure (failure mode) resulting in a random patient positioning error and caused by operator error or device failure (failure causes). Risk assessment is then achieved by identifying 1) the probability of occurrence for each

possible failure (O), 2) the Risk assessment is achieved by establishing 1) the probability of occurrence for each possible failure (O), 2) the severity of the failure effect if unmitigated (S), and 3) the probability that the failure will be undetected (D). Each is rated with a value from 1 (low probability/severity) to 10 (high probability/severity) [126]. Table 5.1 (Chapter 5) displays the O, S, D values proposed by AAPM TG-100 [103]. These values are incorporated into a single risk priority number defined as the product of the three values:

$$RPN = O \times S \times D \quad (A.16)$$

Failure modes can then be ranked according to their RPN value, which high RPN values indicating the riskiest failures. By providing a quantitative measure of risk, FMEA enables identification of failure modes warranting a high degree of focus. Strategies and resources can then be put into place in order to mitigate these failure modes. FMEA ideally promotes efficiency, since resources are distributed according to safety-based needs in a systematic manner, rather than ad-hoc.

References

1. Lawrence TS, Ten Haken R, Giaccia A. Cancer: Principles and Practice of Oncology. 8th ed. 2008, Philadelphia, PA: Lippincott Williams and Wilkins.
2. 2004 IMV Medical Information Division.
3. Timmerman RD, *et al.* Stereotactic body radiation therapy in multiple organ sites. *J Clin Oncol*, 2007. 25(8): p. 947-952.
4. Murphy MJ, *et al.* The management of imaging dose during image-guided radiotherapy: Report of the AAPM Task Group 75. *Med Phys*, 2007. 34(10): p. 4041-4063.
5. Jaffray DA. Image-guided radiotherapy: From current concept to future perspectives. *Nature Reviews Clinical Oncology*, 2012. 9(12): p. 688-699.
6. McParland NA. kV-Cone Beam CT as an IGRT Tool in the Treatment of Early Stage Prostate Cancer: A Literature Review. *J Med Imag Radiat Sci*, 2009. 40(1): p. 9-14.
7. Khoo VS, *et al.* Magnetic resonance imaging (MRI): Considerations and applications in radiotherapy treatment planning. *Radiother Oncol*, 1997. 42(1): p. 1-15.
8. Létourneau D, *et al.* Assessment of residual error for online cone-beam CT-guided treatment of prostate cancer patients. *Int J Rad Onc Biol Phys*, 2005. 62(4): p. 1239-1246.
9. Aoyama H, *et al.* Magnetic resonance imaging system for three-dimensional conformal radiotherapy and its impact on gross tumor volume delineation of central nervous system tumors. *Int J Rad Onc Biol Phys*, 2001. 50(3): p. 821-827.
10. O'Neill BDP, *et al.* MR vs CT imaging: Low rectal cancer tumour delineation for three-dimensional conformal radiotherapy. *Brit J Radiol*, 2009. 82(978): p. 509-513.
11. Villeirs GM, *et al.* Interobserver delineation variation using CT versus combined CT + MRI in intensity-modulated radiotherapy for prostate cancer. *Strahlentherapie und Onkologie*, 2005. 181(7): p. 424-430.
12. Tang X, *et al.* Comparing gross tumor volume of delineation between CT and MRI for nasopharyngeal carcinoma. *Chinese-German J Clin Oncol*, 2005. 4(3): p. 141-145.
13. Dempsey JF, *et al.* A device for realtime 3D image-guided IMRT. *Int J Rad Onc Biol Phys*, 2005. 63: p. S202.
14. Fallone BG, *et al.* First MR images obtained during megavoltage photon irradiation from a prototype integrated linac-MR system. *Med Phys*, 2009. 36(6): p. 2084-2088.
15. Lagendijk JJW, *et al.* MRI/linac integration. *Radiother Oncol*, 2008. 86(1): p. 25-29.
16. Noel CE, *et al.* An automated method for adaptive radiation therapy for prostate cancer patients using continuous fiducial-based tracking. *Phys Med Biol*, 2010. 55(1): p. 65-82.
17. Olsen JR, *et al.* Practical method of adaptive radiotherapy for prostate cancer using real-time electromagnetic tracking. *Int J Rad Onc Biol Phys*, 2012. 82(5): p. 1903-1911.
18. Langen KM and Jones DTL. Organ motion and its management. *Int J Rad Onc Biol Phys*, 2001. 50(1): p. 265-278.
19. Minn AY, Koong AC and Chang DT. Stereotactic body radiation therapy for gastrointestinal malignancies. *Front Radiat Ther Oncol*, 2011. p. 412-427.
20. Wu QJ, *et al.* Adaptive radiation therapy: Technical components and clinical applications. *Cancer Journal*, 2011. 17(3): p. 182-189.
21. British Institute of Radiology, Geometric Uncertainties in Radiotherapy: Defining the Planning Target Volume. 2003, London, UK: BIR Publications.

22. Van Herk M, *et al.* The probability of correct target dosage: Dose-population histograms for deriving treatment margins in radiotherapy. *Int J Rad Onc Biol Phys*, 2000. 47(4): p. 1121-1135.
23. Peeters STH, *et al.* Dose-response in radiotherapy for localized prostate cancer: Results of the Dutch multicenter randomized phase III trial comparing 68 Gy of radiotherapy with 78 Gy. *J Clin Oncol*, 2006. 24(13): p. 1990-1996.
24. Pollack A, *et al.* Prostate cancer radiation dose response: Results of the M. D. Anderson phase III randomized trial. *Int J Rad Onc Biol Phys*, 2002. 53(5): p. 1097-1105.
25. Zelefsky MJ, *et al.* Dose escalation with three-dimensional conformal radiation therapy affects the outcome in prostate cancer. *Int J Rad Onc Biol Phys*, 1998. 41(3): p. 491-500.
26. Gordon JJ and Siebers JV. Coverage-based treatment planning: Optimizing the IMRT PTV to meet a CTV coverage criterion. *Med Phys*, 2009. 36(3): p. 961-973.
27. Huang SH, *et al.* The Effect of Changing Technique, Dose, and PTV Margin on Therapeutic Ratio During Prostate Radiotherapy. *Int J Rad Onc Biol Phys*, 2008. 71(4): p. 1057-1064.
28. Yan D, *et al.* The influence of interpatient and inpatient rectum variation on external beam treatment of prostate cancer. *Int J Rad Onc Biol Phys*, 2001. 51(4): p. 1111-1119.
29. De Boer HCJ and Heijmen BJM. A protocol for the reduction of systematic patient setup errors with minimal portal imaging workload. *Int J Rad Onc Biol Phys*, 2001. 50(5): p. 1350-1365.
30. Yan D, *et al.* Adaptive modification of treatment planning to minimize the deleterious effects of treatment setup errors. *Int J Rad Onc Biol Phys*, 1997. 38(1): p. 197-206.
31. Yan D, *et al.* A new model for 'accept or reject' strategies in off-line and on-line megavoltage treatment evaluation. *Int J Rad Onc Biol Phys*, 1995. 31(4): p. 943-952.
32. Lee L, Le QT and Xing L. Retrospective IMRT Dose Reconstruction Based on Cone-Beam CT and MLC Log-File. *Int J Rad Onc Biol Phys*, 2008. 70(2): p. 634-644.
33. Woodford C, *et al.* Adaptive Radiotherapy Planning on Decreasing Gross Tumor Volumes as Seen on Megavoltage Computed Tomography Images. *Int J Rad Onc Biol Phys*, 2007. 69(4): p. 1316-1322.
34. Wu QJ, *et al.* On-line re-optimization of prostate IMRT plans for adaptive radiation therapy. *Phys Med Biol*, 2008. 53(3): p. 673-691.
35. Oelfke U, *et al.* Linac-integrated kV-cone beam CT: Technical features and first applications. *Med Dosim*, 2006. 31(1): p. 62-70.
36. Baumann M, Hölscher T and Zips D. The future of IGRT - Cost benefit analysis. *Acta Oncologica*, 2008. 47(7): p. 1188-1192.
37. Verellen D, *et al.* An overview of volumetric imaging technologies and their quality assurance for IGRT. *Acta Oncologica*, 2008. 47(7): p. 1271-1278.
38. Chen GTY, Sharp GC and Mori S. A review of image-guided radiotherapy. *Radiol Phys Tech*, 2009. 2(1): p. 1-12.
39. Tran WT. Practical Considerations in Cone Beam and Ultrasound IGRT Systems in Prostate Localization: A Review of the Literature. *J Med Imag Radiat Sci*, 2009. 40(1): p. 3-8.
40. Moseley DJ, *et al.* Comparison of localization performance with implanted fiducial markers and cone-beam computed tomography for on-line image-guided radiotherapy of the prostate. *Int J Rad Onc Biol Phys*, 2007. 67(3): p. 942-953.
41. Swerdloff SJ. Data Handling in Radiation Therapy in the Age of Image-Guided Radiation Therapy. *Seminars in Rad Onc*, 2007. 17(4): p. 287-292.

42. Balter JM, *et al.* Accuracy of a wireless localization system for radiotherapy. *Int J Rad Onc Biol Phys*, 2005. 61(3): p. 933-937.
43. Parikh PJ, *et al.* 4D verification of real-time accuracy of the Calypso system with lung cancer patient trajectory data. *Int J Rad Onc Biol Phys*, 2005. 63: p. 26-7.
44. Deasy JO, Blanco AI and Clark VH. CERR: A computational environment for radiotherapy research. *Med Phys*, 2003. 30(5): p. 979-985.
45. Kupelian P, *et al.* Multi-institutional clinical experience with the Calypso System in localization and continuous, real-time monitoring of the prostate gland during external radiotherapy. *Int J Rad Onc Biol Phys*, 2007. 67(4): p. 1088-1098.
46. van der Wielen GJ, *et al.* Deformation of Prostate and Seminal Vesicles Relative to Intraprostatic Fiducial Markers. *Int J Rad Onc Biol Phys*, 2008. 72(5): p. 1604-1611.e3.
47. Deurloo KEI, *et al.* Quantification of shape variation of prostate and seminal vesicles during external beam radiotherapy. *Int J Rad Onc Biol Phys*, 2005. 61(1): p. 228-238.
48. Bharat S, *et al.* Motion-compensated estimation of delivered dose during external beam radiation therapy: Implementation in Philips' Pinnacle 3 treatment planning system. *Med Phys*, 2012. 39(1): p. 437-443.
49. Gutt R, Liauw SL and Weichselbaum RR. The role of radiotherapy in locally advanced pancreatic carcinoma. *Nat Rev Gastroenterology and Hepatology*, 2010. 7(8): p. 437-447.
50. Hallissey MT, *et al.* The second british stomach cancer group trial of adjuvant radiotherapy or chemotherapy in resectable gastric cancer: Five-year follow-up. *Lancet*, 1994. 343(8909): p. 1309-1312.
51. Swaminath A and Dawson LA. Emerging role of radiotherapy in the management of liver metastases. *Cancer Journal*, 2010. 16(2): p. 150-155.
52. Dawson LA, *et al.* MRI for tumor volume definition during radiation planning of unresectable intrahepatic malignancies. in *Amer Soc Clin Oncol*. 2003.
53. Méndez Romero A, *et al.* Comparison of macroscopic pathology measurements with magnetic resonance imaging and assessment of microscopic pathology extension for colorectal liver metastases. *Int J Rad Onc Biol Phys*, 2012. 82(1): p. 159-166.
54. Voroney JJ, *et al.* A Prospective Comparison Study of Liver Tumour Target Definition Based on Triphasic CT and Gadolinium MR. *Int J Radiat Oncol Biol Phys*. 2005. 63(S1): p. S282.
55. Hamm B, *et al.* *MR Imaging of the Abdomen and Pelvis*. 2009, Stuttgart, Germany: Thieme.
56. Warfield SK, Zou KH and Wells WM. Simultaneous truth and performance level estimation (STAPLE): An algorithm for the validation of image segmentation. *IEEE Transactions on Med Imag*, 2004. 23(7): p. 903-921.
57. Hwee J, *et al.* Technology assessment of automated atlas based segmentation in prostate bed contouring. *Rad Onc*, 2011. 6(1).
58. Ost P, *et al.* Delineation of the postprostatectomy prostate bed using computed tomography: Interobserver variability following the EORTC delineation guidelines. *Int J Rad Onc Biol Phys*, 2011. 81(3): p. e143-e149.
59. Stapleford LJ, *et al.*, Evaluation of Automatic Atlas-Based Lymph Node Segmentation for Head-and-Neck Cancer. *Int J Rad Onc Biol Phys*, 2010. 77(3): p. 959-966.
60. Pekar V, *et al.* Head and Neck Auto-segmentation Challenge: Segmentation of the Parotid Glands. in *Int Conf Med Image Comput Computer Assist Intervention*. 2010.
61. Zou KH, *et al.* Statistical Validation of Image Segmentation Quality Based on a Spatial Overlap Index. *Academic Radiology*, 2004. 11(2): p. 178-189.

62. Zijdenbos AP, *et al.* Morphometric analysis of white matter lesions in MR images: method and validation. *IEEE Transactions on Med Imag*, 1994. 13(4): p. 716-724.
63. Shrout PE and Fleiss JL. Intraclass correlations: Uses in assessing rater reliability *Psychological Bulletin*, 1979. 86(2): p. 420-428.
64. Lee YK, *et al.* Radiotherapy treatment planning of prostate cancer using magnetic resonance imaging alone. *Radiother Oncol*, 2003. 66(2): p. 203-216.
65. Feng M, *et al.* Characterization of Pancreatic Tumor Motion Using Cine MRI: Surrogates for Tumor Position Should Be Used With Caution. *Int J Rad Onc Biol Phys*, 2009. 74(3): p. 884-891.
66. Devic S. MRI simulation for radiotherapy treatment planning. *Med Phys*, 2012. 39(11): p. 6701-6711.
67. Raaymakers BW, *et al.* Integrating a 1.5 T MRI scanner with a 6 MV accelerator: Proof of concept. *Phys Med Biol*, 2009. 54(12): p. N229-N237.
68. Kron T, *et al.* Adaptive radiotherapy for bladder cancer reduces integral dose despite daily volumetric imaging. *Radiother Oncol*, 2010. 97(3): p. 485-487.
69. Santanam L, *et al.* Standardizing naming conventions in radiation oncology. *Int J Rad Onc Biol Phys*, 2012. 83(4): p. 1344-1349.
70. Islam MK, *et al.* An integral quality monitoring system for real-time verification of intensity modulated radiation therapy. *Med Phys*, 2009. 36(12): p. 5420-5428.
71. Landis JR and Koch GG. The measurement of observer agreement for categorical data. *Biometrics*, 1977. 33(1): p. 159-174.
72. Dawson LA and Sharpe MB. Image-guided radiotherapy: rationale, benefits, and limitations. *Lancet Oncol*, 2006. 7(10): p. 848-858.
73. Verellen D, *et al.* Innovations in image-guided radiotherapy. *Nat Rev Cancer*, 2007. 7(12): p. 949-960.
74. Boda-Heggemann J, *et al.* kV cone-beam CT-based IGRT. *Strahlentherapie und Onkologie*, 2011. 187(5): p. 284-291.
75. Jonsson JH, *et al.* Treatment planning using MRI data: An analysis of the dose calculation accuracy for different treatment regions. *Radiat Oncol*, 2010. 5(1).
76. Chen L, *et al.* MRI-based treatment planning for radiotherapy: Dosimetric verification for prostate IMRT. *Int J Rad Onc Biol Phys*, 2004. 60(2): p. 636-647.
77. Lambert J, *et al.* MRI-guided prostate radiation therapy planning: Investigation of dosimetric accuracy of MRI-based dose planning. *Radiother Oncol*, 2011. 98(3): p. 330-334.
78. Kapanen M, *et al.* Commissioning of MRI-only based treatment planning procedure for external beam radiotherapy of prostate. *Magn Res Med*, 2013. 70(1): p. 127-135.
79. Xiong LL, *et al.* Early clinical experience using high intensity focused ultrasound for palliation of inoperable pancreatic cancer. *J Pancreas*, 2009. 10(2): p. 123-129.
80. Goyal K, *et al.* Stereotactic body radiation therapy for nonresectable tumors of the pancreas. *J Surgical Research*, 2012. 174(2): p. 319-325.
81. Greco C, *et al.* Radiotherapy of liver malignancies. From whole liver irradiation to stereotactic hypofractionated radiotherapy. *Tumori*, 2004. 90(1): p. 73-79.
82. Coia LR. Late effects of radiation therapy on the gastrointestinal tract. *Int J Rad Onc Biol Phys*, 1995. 31(5): p. 1213-1236.
83. Low DA, 4D imaging and 4D radiation therapy: A new era of therapy design and delivery. *Front Radiat Ther Oncol*, 2011. 43:p. 99-117.

84. Froehlich JM, *et al.* MR motility imaging in Crohn's disease improves lesion detection compared with standard MR imaging. *Euro Radiol*, 2010. 20(8): p. 1945-1951.
85. Wu X, *et al.* Orientation adaptive fast marching method for contour tracking of small intestine. *Electronics Letters*, 2009. 45(23): p. 1154-1155.
86. Buzurovic I, *et al.* A robotic approach to 4D real-time tumor tracking for radiotherapy. *Phys Med Biol*, 2011. 56(5): p. 1299-1318.
87. Ren Q, *et al.* Adaptive prediction of respiratory motion for motion compensation radiotherapy. *Phys Med Biol*, 2007. 52(22): p. 6651-6661.
88. Yigitsoy M, *et al.* Out-of-plane motion compensation in cine-MRI. *Abdominal Imaging. Computational and Clinical Applications, LNCS* 2012. p. 107-115.
89. Cerviño LI, Du J and Jiang SB. MRI-guided tumor tracking in lung cancer radiotherapy. *Phys Med Biol*, 2011. 56(13): p. 3773-3785.
90. Leymarie F. Tracking and Describing Deformable Objects Using Active Contour Models, Technical Report TR-CIM-90-9. 2003: Montreal, CA.
91. Kass M, Witkin A and D. Terzopoulos. Snakes: Active contour models. *Int J Comp Vis*, 1988. 1(4): p. 321-331.
92. Derraz, F., M. Beladgham, and M. Khelif. Application of active contour models in medical image segmentation. *Int Conf Information Tech: Coding Computing*, 2004.
93. Udayashankara V. Modern Digital Signal Processing: Includes Signals and Systems Matlab Programs, Dsp Architecture with Assembly and C Programs. 2012, New Delhi, India: PHI Private Learning Limited.
94. Glocker B, *et al.* Towards a computer aided diagnosis system for colon motility dysfunctions. *Proc. SPIE 6514, Med Imag 2007: Computer-Aided Diagnosis, 65140B*, 2007.
95. Tang X, Sharp GC and Jiang SB. Fluoroscopic tracking of multiple implanted fiducial markers using multiple object tracking. *Phys Med Biol*, 2007. 52(14): p. 4081-4098.
96. Xu C and Prince JL. Gradient vector flow: A new external force for snakes. *IEEE Proc. Conf on Comp Vis Patt Recog*, 1997.
97. Cohen LD and Coehn I. Finite Element Methods for Active Contour Models and Balloons for 2D and 3D Images *IEEE Transactions on Pattern Analysis and Machine Intelligence*, 1991.
98. Yoshida H, Hawkes D, Vannier MW. *Abdominal Imaging LNCS*, 2012(7601): p. 107-115.
99. Yeung TK, *et al.* Quality assurance in radiotherapy: evaluation of errors and incidents recorded over a 10 year period. *Radiother Oncol*, 2005. 74: p. 283-291.
100. Williamson JF, *et al.* Quality assurance needs for modern image-based radiotherapy: recommendations from 2007 interorganizational symposium on Quality Assurance of Radiation Therapy: Challenges of Advanced Technology. *Int J Radiat Oncol Biol Phys*, 2008. 71(1 Suppl): p. S2-12.
101. Terezakis SA, *et al.* Safety strategies in an academic radiation oncology department and recommendations for action. *Jt Comm J Qual Patient Saf*, 2011. 37(7): p. 291-9.
102. Huq MS, *et al.* A method for evaluating quality assurance needs in radiation therapy. *Int J Radiat Oncol Biol Phys*, 2008. 71(1 Suppl): p. S170-3.
103. Thomadsen BR, *et al.* Risk assessment using TG-100 methodology Table 4-3 in *Quality and Safety in Radiotherapy: Learning the New Approaches in Task Group 100 and Beyond*. *AAPM Monograph* 2013. 36: p. 95-112.

104. Brewster LM, *et al.* An Electronic Whiteboard and Associated Databases for Physics Workflow Coordination in a Paperless, Multi-Site Radiation Oncology Department. *Med Phys*, 2011. 38: p. 3755.
105. Santanam L, *et al.*, Eliminating inconsistencies in simulation and treatment planning orders in radiation therapy. *Int J Rad Onc Biol Phys*, 2013. 85(2): p. 484-491.
106. Sharpe M, Brock KK. Quality Assurance of Serial 3D Image Registration, Fusion, and Segmentation. *Int J Rad Onc Biol Phys*, 2008. 71(1 Suppl): p. S33-S37.
107. Sun B, *et al.* Evaluation of the efficiency and effectiveness of independent dose calculation followed by machine log file analysis against conventional measurement based IMRT QA. *J Appl Clin Med Phys*, 2012. 13(5): p. 140-154.
108. Xing L and Li JG. Computer verification of fluence map for intensity modulated radiation therapy. *Med Phys*, 2000. 27(9): p. 2084-2092.
109. Yang D and Moore KL. Automated radiotherapy treatment plan integrity verification. *Med Phys*, 2012. 39(3): p. 1542-1551.
110. Zhu X, *et al.* A planning quality evaluation tool for prostate adaptive IMRT based on machine learning. *Med Phys*, 2011. 38(2): p. 719-726.
111. Moore KL, *et al.* Experience-based quality control of clinical intensity-modulated radiotherapy planning. *Int J Rad Onc Biol Phys*, 2011. 81(2): p. 545-551.
112. QAPV Simulator Hosting Site. QAPV-Simulator: Simulator for the actors found in IHE-RO profile QAPV.; Available from: <http://code.google.com/p/qapv-simulator>.
113. Goulet M, Gingras L, and Beaulieu L. Real-time verification of multileaf collimator-driven radiotherapy using a novel optical attenuation-based fluence monitor. *Med Phys*, 2011. 38(3): p. 1459-1467.
114. Wong JHD, *et al.* Characterization of a novel two dimensional diode array the magic plate as a radiation detector for radiation therapy treatment. *Med Phys*, 2012. 39(5): p. 2544-2558.
115. Jiang Y, *et al.* Real-Time Dose Reconstruction for Treatment Monitoring, in AAPM Annual Meeting. 2010. p. 3400.
116. Peng C, *et al.* Validation of an online replanning technique for prostate adaptive radiotherapy. *Phys Med Biol*, 2011. 56(12): p. 3659-3668.
117. Ford EC, *et al.* Quality control quantification (QCQ): A tool to measure the value of quality control checks in radiation oncology. *Int J Rad Onc Biol Phys*, 2012. 84(3): p. e263-e269.
118. Fuangrod T, *et al.* Development of EPID-based real time dose verification for dynamic IMRT. *World Academy of Science, Engineering and Tech*, 2011. 80: p. 609-612.
119. Pawlicki T, *et al.* Moving from IMRT QA measurements toward independent computer calculations using control charts. *Radiother Oncol*, 2008. 89: p. 330-337.
120. Litzenberg DW, *et al.* Positional Stability of Electromagnetic Transponders Used for Prostate Localization and Continuous, Real-Time Tracking. *Int J Rad Onc Biol Phys*, 2007. 68(4): p. 1199-1206.
121. Santanam L, *et al.* Quality assurance for clinical implementation of an electromagnetic tracking system. *Med Phys*, 2009. 36(8): p. 3477-3486.
122. Low DA, *et al.* A technique for the quantitative evaluation of dose distributions. *Med Phys*, 1998. 25(5): p. 656-661.
123. Low DA and Dempsey JF, Evaluation of the gamma dose distribution comparison method. *Med Phys*, 2003. 30(9): p. 2455-2464.

124. Raaijmakers AJE, Raaymakers BW, and Lagendijk JJW. Magnetic-field-induced dose effects in MR-guided radiotherapy systems: Dependence on the magnetic field strength. *Phys Med Biol*, 2008. 53(4): p. 909-923.
125. Hu Y, *et al.* Image Performance Characterization of an MRI-Guided Radiotherapy System, in *ASTRO 55th Annual Meeting*. 2013.
126. McDermott RE, Mikulak MR, Beauregard MR. *The Basics of FMEA*. 1996, New York, NY: Productivity Press.

Curriculum Vitae

Camille E. Noel

- Degrees Ph.D. Biomedical Engineering, August 2013
Washington University, Saint Louis MO
- M.S. Clinical Investigation, August 2013
Washington University School of Medicine, Saint Louis MO
- B.S. Physics, December 2006
University of Illinois, Urbana-Champaign IL
- Academic Positions Graduate Student, Department of Biomedical Engineering,
& Employment Washington University, Saint Louis MO, 2009 – Present
- Clinical Physics Assistant, Department of Radiation Oncology, Physics
Division, Washington University School of Medicine, Saint Louis MO,
2007 – 2009
- Research Assistant, Department of Radiation Oncology, Washington
University School of Medicine, Saint Louis MO, 2006 – 2007
- Professional American Association of Physicists in Medicine
Societies & Awards American Society for Therapeutic Radiation Oncology
 Institute of Clinical and Translational Sciences
 Society of Women Engineers
 Reviewer – International Journal of Radiation Oncology and Biology
 Reviewer – Medical Physics
 Reviewer – Radiotherapy and Oncology
 Reviewer – The International Journal of Medical Robotics and
Computer Assisted Surgery
 Clinical and Translational Science Award, 2-year (NIH grant UL1 TR000448)
- Publications **Noel CE**, Santanam L, *et al.* “Process-Based Quality Management for
Clinical Implementation of Adaptive Radiotherapy” Int J Radiat Oncol Biol
Phys. 2013 (submitted)
- Noel CE**, Parikh PJ, *et al.* “Comparison Of Onboard Low-field MRI Versus
CBCT/MVCT For Anatomy Visualization In Radiotherapy” Int J Radiat
Oncol Biol Phys. 2013 (submitted)
- Noel CE**, Zhu F, *et al.* “Segmentation precision of abdominal anatomy for
MRI-based radiotherapy” J Appl Clin Med Phys. 2013 (submitted)

Smith RL, Wen J, **Noel CE**, *et al.* “A respiratory correlated image guided surgery method: Quantitative accuracy results in swine and human cadaver environments” *Int J Med Robotics Comp Assist Surg.* 2013

Ge J, Santanam L, **Noel CE**, *et al.* “Planning 4-dimensional computed tomography (4DCT) cannot adequately represent daily intrafractional motion of abdominal tumors” *Int J Rad Onc Biol Phys.* 2013; 85(4):999-1005.

Li H, **Noel CE**, *et al.* “Clinical evaluation of a commercial orthopedic metal artifact reduction tool for CT simulations in radiation therapy” *Med Phys.* 2012; 39(12):7507-17.

Li H, **Noel CE**, *et al.* “Clinical evaluations of an amplitude-based binning algorithm for 4DCT reconstruction in radiation therapy” *Med Phys.* 2012; 39(2):922-32.

Olsen JR, **Noel CE**, *et al.* “Practical method of adaptive radiotherapy for prostate cancer using real-time electromagnetic tracking” *Int J Rad Onc Biol Phys.* 2012; 82(5):1903-11.

Olsen JR, Parikh PJ, Watts M, **Noel CE**, *et al.* “Comparison of dose decrement from intrafraction motion for prone and supine prostate radiotherapy” *Radiother Oncol.* 2012; 104(2):199-204.

Bharat S, Parikh P, **Noel CE**, *et al.* “Motion-compensated estimation of delivered dose during external beam radiation therapy: Implementation in Philips' Pinnacle 3 treatment planning system” *Med Phys.* 2012; 39(1):437-43.

Noel CE, Parikh PJ. “Effect of mid-scan breathing changes on quality of 4DCT using a commercial phase-based sorting algorithm” *Med Phys.* 2011; 38(5):2430-8.

Noel CE, Santanam L, *et al.* “An automated method for adaptive radiation therapy for prostate cancer patients using continuous fiducial-based tracking” *Phys Med Biol.* 2010; 55(1):65-82.

Low DA, Zhao T, White B, Yang D, Mutic S, **Noel CE**, *et al.* “Application of the continuity equation to a breathing motion model” *Med Phys.* 2010; 37(3):1360-4.

Zhao T, Lu W, Yang D, Mutic S, **Noel CE**, *et al.* “Characterization of free breathing patterns with 5D lung motion model” *Med Phys.* 2009; 36(11):5183-9.

Santanam L, **Noel CE**, *et al.* “Quality assurance for clinical implementation of an electromagnetic tracking system” *Med Phys.* 2009; 36(8):3477-86.

Noel CE, Parikh PJ, *et al.* “Prediction of intrafraction prostate motion: Accuracy of pre- and post-treatment imaging and intermittent imaging” *Int J Rad Onc Biol Phys.* 2009; 73(3):692-8.

Yalavarthy PK, Low D, **Noel CE**, *et al.* “Current role of PET in oncology: Potentials and challenges in the management of non-small cell lung cancer” *Asilomar Conference on Signals, Systems and Computers.* 2008; 1067-71.

Malinowski KT, **Noel CE**, *et al.* “Efficient use of continuous, real-time prostate localization” *Phys Med Biol.* 2008; 53(18):4959-70.

Malinowski K, **Noel CE**, *et al.* “Development of the 4D Phantom for patient-specific, end-to-end radiation therapy QA” *Prog Biomed Optics Imag.* 2007. 6510.

Book Chapters

“4D treatments & motion management” in *Quality Assurance and Safety in Radiotherapy*: Pawlicki T, Dunscombe PB, Mundt AJ, Scalliet P. CRC Press. 2011.

Oral Presentations
& Invited Lectures

Noel CE, Parikh PJ, *et al.* “Comparison of Onboard Low-field MRI Versus CBCT/MVCT For Anatomy Visualization in Radiotherapy” *ASTRO 2012.*

Noel CE, Santanam L, *et al.* “Risk analysis for clinical implementation of adaptive radiation adaptive radiation therapy” *ASTRO 2012.*

Noel CE. “Dosimetric Evaluation Using Fiducial-Tracking Data” *ESTRO Pinnacle Research Forum 2012.*

Noel CE, Olsen JR, *et al.* “Feasibility of Bowel Tracking Using Onboard Cine MRI for Gated Radiotherapy” *AAPM 2012.*

Noel CE, Santanam L, *et al.* “Establishing Motion Tolerances for Reduced-Margin Planning of Prostate Cancer Patients” *International Conference for Translational Research in Radiation Oncology (ICTR) 2009.*

Noel CE. “Real-time Electromagnetic Tracking in Radiation Therapy” *Missouri River Valley AAPM Chapter Meeting 2009.*

Noel CE, Santanam L, *et al.* “Analysis Of The Effect Of Prostate Rotation On Target Coverage Using Real-Time Tracking Technology” *Electronic Portal Imaging & Positioning Devices (EPI) 2008.*

Noel CE, Roy M, *et al.* “Are Pre and Post Imaging Sufficient to Assess Intrafraction Prostate Motion?” *ASTRO 2007.*

Noel CE, Parikh PJ. “The effect of mid-scan changes of breathing frequency and amplitude on 4D CT quality” *AAPM 2007.*

Noel CE. “4D CT: Evaluation of Imaging Quality Using Respiratory Gating.” Philips Healthcare - Radiation Oncology, Cleveland OH, 2006.

Selected Proceedings **Noel CE, Santanam L, et al.** “Risk Analysis for Clinical Implementation of Adaptive Radiotherapy” ASTRO 2012.

Noel CE, Olsen JR, et al. “Feasibility of Bowel Tracking Using Onboard Cine MRI for Gated Radiotherapy” AAPM 2012.

Olsen JR, **Noel CE, et al.** “Feasibility of Single and Multiplane Cine MR for Monitoring Tumor Volumes and Organs-at-Risk (OARs) Position During Radiation Therapy” ASTRO 2012.

Parikh PJ, **Noel CE, et al.** “Comparison of Onboard Low-field MRI Versus CBCT/MVCT for Anatomy Identification in Radiation Therapy” ASTRO 2012.

Noel CE, Higham-Kessler J, et al. “Feasibility of fiducial-based Electromagnetic tracking for postoperative radiotherapy to the prostate bed.” ASTRO 2010.

Noel CE, Olsen JR, et al. “Establishing Motion Tolerances for Reduced-Margin Planning of Prostate Cancer Patients” International Conference for Translational Research in Radiation Oncology (ICTR), 2009.

Olsen JR, **Noel CE, et al.** “A Practical Method of Adaptive Radiotherapy for Prostate Cancer using Real-time Electromagnetic Tracking” ASTRO 2009.

Palaniswaamy G, **Noel CE, et al.** “Dose Perturbation Due To High Z Artifacts in IMRT Planning” AAPM 2009.

Olsen JR., **Noel CE, et al.** “Individual Margin Determination for Prostate Cancer Patients Undergoing Real-Time Tracking” ASTRO 2008.

Yalavarthy P, Low D, **Noel CE, et al.** “Current role of PET in oncology: Potentials and challenges in the management of non-small cell lung cancer” IEEE 2008.

Esthappan J, Santanam L, **Noel CE, et al.** “Dosimetric Evaluation of 4D CT-based Treatment Planning for SBRT of Mobile Lung Tumors” ASTRO 2008.

Noel CE, E Klein, et al. “A Surface-Based Respiratory Surrogate for 4D Imaging” AAPM 2008.

Goddu S, **Noel CE**, *et al.* “4D Treatment Planning and Dosimetric Validation of Helical Tomotherapy Treatments of Moving Tumors” AAPM 2008.

Zhao T, Bradley J, **Noel CE**, *et al.* “Application of 5D Breathing Motion Model for Monitoring Radiation Damage” AAPM 2008.

Noel CE, Santanam L, *et al.* “Analysis Of The Effect Of Prostate Rotation On Target Coverage Using Real-Time Tracking Technology” EPI 2008.

Noel CE, Roy M, *et al.* “Are Pre and Post Imaging Sufficient to Assess Intrafraction Prostate Motion?” ASTRO 2007.

Noel CE, Parikh P, *et al.* “The effect of mid-scan changes of breathing frequency and amplitude on 4D CT quality” AAPM 2007.

Improving Radiotherapy Targeting, Noel, Ph.D. 2013